BRNO UNIVERSITY OF TECHNOLOGY

VYSOKÉ UČENÍ TECHNICKÉ V BRNĚ

FACULTY OF MECHANICAL ENGINEERING

FAKULTA STROJNÍHO INŽENÝRSTVÍ

INSTITUTE OF AEROSPACE ENGINEERING

LETECKÝ ÚSTAV

METHODOLOGY OF ANALYSIS OF WING STRUCTURE WITH RESPECT TO WIDESPREAD FATIGUE DAMAGE (WFD)

METODIKA VÝPOČTU ČÁSTI KONSTRUKCE KŘÍDLA S OHLEDEM NA MOŽNOST ROZVOJE MNOHOOHNISKOVÉHO ÚNAVOVÉHO POŠKOZENÍ (WFD)

MASTER'S THESIS

DIPLOMOVÁ PRÁCE

AUTHOR   Bc. Martin Bulko
AUTOR PRÁCE

SUPERVISOR   Ing. Dalibor Vlček
VEDOUCÍ PRÁCE

BRNO 2016

VYSOKÉ UČENÍ FAKULTA
TECHNICKÉ STROJNÍHO
V BRNĚ INŽENÝRSTVÍ

Zadání diplomové práce

Ústav: Letecký ústav
Student: **Bc. Martin Bulko**
Studijní program: Strojní inženýrství
Studijní obor: Stavba letadel
Vedoucí práce: **Ing. Dalibor Vlček**
Akademický rok: 2015/16

Ředitel ústavu Vám v souladu se zákonem č.111/1998 o vysokých školách a se Studijním a zkušebním řádem VUT v Brně určuje následující téma diplomové práce:

Metodika výpočtu části konstrukce křídla s ohledem na možnost rozvoje mnohoohniskového únavového poškození (WFD)

Stručná charakteristika problematiky úkolu:

Problematika WFD nabývá v posledních letech značného významu, což je reflektováno i nově zaváděnými požadavky předpisů letové způsobilosti. V posledních 25 letech byl fenomén WFD příčinou několika závažných provozních poruch zejména u velkých dopravních letadel. Plné zvládnutí této problematiky je v dnešní době podmínkou pro certifikaci letounu v kategorii commuter dle FAR 23.

Cíle diplomové práce:

V první části diplomant provede rozbor platných předpisů letové způsobilosti vztahujících se k danému tématu. V další části bude provedena rešerše publikovaných prací v této oblasti. Stěžejní částí práce bude vlastní tvorba algoritmu výpočtu. Tento algoritmus bude zahrnovat stochastický model rozvoje únavového poškození založený na simulační metodě Monte Carlo. Dále bude navržen analytický způsob výpočtu faktoru intenzity napětí pomocí superpozice základních konfigurací trhliny, pro které je řešení známo v uzavřeném tvaru. Získané hodnoty faktoru intenzity napětí budou vstupem do simulace šíření trhliny při zatěžování provozní sekvencí zatížení. Součástí algoritmu bude i výpočet zbytkové pevnosti porušující se konstrukce. Závěrečným výstupem celé simulace bude distribuční funkce vztahující se k pravděpodobnosti rozvoje WFD po určité době provozu letounu.
Diplomová práce by měla být ve společnosti Aircraft Industries, a.s. přímo využitelná při vývoji nových výpočetních metod v rámci průkazu únavové životnosti a odolnosti proti poškození letounu L 410 NG.

Seznam literatury:

Swift, T. (1993): Widespread fatigue Damage Monitoring – Issues and Concerns. Report N95-1948.

Schijve J. (2009): Fatigue of Structures and Materials. Springer, Dordrecht, The Netherlands.

Schmidt, H.-J., Schmidt-Brandecker, B. (2012): Fatigue and Damage Tolerance Course for Metal Structure.

Bent, L.J. (2010): Practical Airframe Fatigue and Damage Tolerance. Sigma K Ltd, Coylton, Scotland.

Isida, M. (1996): Stress intensity factors for the tension of an eccentrically cracked strip. Transactions of the ASME Applied Mechanics Section, v. 88, p.94.

Rooke, D. P., Cartwright, D. J. (1974): Compendium of Stress Intensity Factors. Her Majesty's Stationery Office, London, UK.

Eastin, R. G., Sippel, W. (2011): The „WFD rule" – have we come full circle? Paper presented at USAF Aircraft Structural Integrity Conference, San Antonio, TX, USA.

Termín odevzdání diplomové práce je stanoven časovým plánem akademického roku 2015/16

V Brně, dne

L. S.

<table>
<tr><td>doc. Ing. Jaroslav Juračka, Ph.D.</td><td>doc. Ing. Jaroslav Katolický, Ph.D.</td></tr>
<tr><td>ředitel ústavu</td><td>děkan fakulty</td></tr>
</table>

Abstract

The thesis presents the methodology for analyses of the widespread fatigue damage (WFD) susceptible structures. Firstly, the airworthiness regulations related to WFD for airplanes certified in compliance with FAR 23 in the category commuter are introduced. Methods of fatigue calculation and crack growth prediction follow. Solutions to stress intensity factor for basic crack configurations are presented in a closed form or in a tabular form. Central part of the work is a development of the algorithm AIMA, which provides complex analysis of the structure with respect to multiple site damage. Validation is performed on the bottom wing panel splice joint fatigue test specimen, followed by the analysis of the real L 410 NG bottom wing panel splice joint.

Keywords

WFD, widespread fatigue damage, MSD, multiple site damage, fatigue, fracture mechanics, stress intensity factor, crack growth

Abstrakt

Diplomová práce popisuje metodiku výpočtů částí náchylných k rozvoji mnoho-ohniskového únavového poškození (WFD). Nejdříve se práce zabývá rozborem předpisů letové způsobilosti souvisejících s WFD pro letadla certifikovaných podle FAR 23 v kategorii commuter. Následuje popis metodiky únavového výpočtu a predikce šíření trhliny. Dále jsou popsány řešení pro výpočet faktoru intenzity napětí pro základné konfigurace trhliny, tam kde to bylo možné v uzavřeném tvaru, jinak ve formě tabulky. Hlavní částí práce je návrh algoritmu AIMA schopného provést kompletní analýzu části náchylné k rozvoji únavového poškození na více místech (MSD). Model se validoval únavovou zkouškou vzorku přeplátovaného spoje dolního panelu křídla. Následně byla analyzována reálná konstrukce spoje dolních panelů křídla letounu L 410 NG.

Klíčové slova

WFD, mnohoohniskové únavové poškození, MSD, únava, lomová mechanika, faktor intenzity napětí, růst trhlin

Bibliografická citace

BULKO, M. *Metodika výpočtu části konstrukce křídla s ohledem na možnost rozvoje mnohoohniskového únavového poškození (WFD).* Brno: Vysoké učení technické v Brně, Fakulta strojního inženýrství, 2016. 96 s. Vedoucí diplomové práce Ing. Dalibor Vlček.

Čestné prohlášení

Prohlašuji, že jsem byl obeznámen s předpisy pro vypracování diplomové práce a že jsem celou práci vypracoval samostatně, s použitím uvedené literatury, pod vedením Ing. Dalibora Vlčka.

V Brně dne 24.5.2016

....

Martin Bulko

Poděkování

Contents

1   Introduction

As the currently operating aircraft fleets are aging, the importance of widespread fatigue damage (WFD) is growing. Because the WFD has been a cause of several structural failures in large transport aircraft in recent years, new airworthiness regulations were introduced in order to prevent further WFD occurrence. Nowadays, airplanes certified in compliance with FAR 23 in the category commuter must prove as well that WFD is unlikely to occur during the whole operational life.

In the first part the thesis describes the widespread fatigue damage together with analysis methods recommended by Advisory Circular 120-104. Later on a brief analysis of the regulations associated with WFD takes place.

The goal of the thesis is to develop an algorithm for analyses of wing structure with respect to WFD. Because of the probabilistic nature of fatigue, a Monte Carlo simulation method is employed. Stochastic part of the simulation is represented by the fatigue crack initiation calculation, while the deterministic part covers the crack growth stage. For the crack growth prediction the closed-form solutions to stress intensity factor for basic crack configurations are utilised. Complex configurations are solved with applying a compounding and superposition principle.

Finally, the algorithm of the analysis is designed. It is created in Matlab with full compatibility with an open source substitution Octave. The correctness of the algorithm is about to be validated by results of the fatigue test of the bottom panel splice joint specimen. Afterwards, an analysis of one structural joint of the wing takes place.

1.1 L 410 NG parameters

Figure 1.1 L 410 NG [44]

L 410 NG is a twin turbo-prop engine commuter airplane with capacity of 19 passengers. It is a new version of L 410 with several major changes, e.g. new wing construction, new engines or a use of glass cockpit. Basic specifications are summarized in Table 1.1. Design parameters for purposes of fatigue and damage tolerance assessment are presented in Table 1.2.

Table 1.1 L 410 NG specifications

Maximum take-off weight	7 000 kg
Maximum landing weight	6 800 kg
Maximum zero fuel weight	6 600 kg
Engines	GE H85-200
Propellers	AV-725

Table 1.2 Damage tolerance design parameters

Design Service Goal	30 000 flight hours	30 000 flight cycles
Inspection Threshold	15 000 flight hours	15 000 flight cycles
Inspection Interval	5 000 flight hours	5 000 flight cycles

2   Widespread fatigue damage

2.1   Introduction

Damage tolerance approach used for aircraft designing requires proving that the structure is able to withstand limit loads with a cracked part. After a crack is detected, a repair is performed and the aircraft can be further operated. However, for aging aircrafts degradation at multiple places may take place, which on 28 April 1988 resulted in an accident.

Boeing 737-297 of Aloha Airlines operating the scheduled flight 243 between Hilo and Honolulu experienced an explosive decompression leading to extensive damage. Approximately 6 m of the fuselage skin above the passenger floorline separated from the airplane during the flight, see Figure 2.1. One fatality and 8 serious injuries were recorded. At the time of accident, the B737 had flown 35 496 flight hours (89 680 flight cycles), i.e. was operating beyond its design service goal.
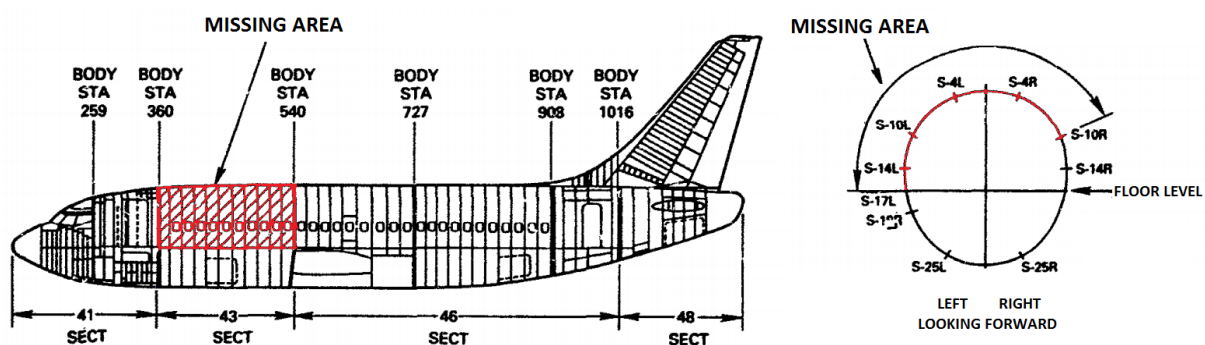
Figure 2.1 Description of the separated area of B737 [43]

The consequent accident investigation [43] concluded that weather was not the cause of the accident. However, it was stated that quality of inspections and maintenance programme was deficient, showing inability to detect the presence of significant fatigue damage. The failure initiated in the fuselage lap joint as a result of disbonding with subsequent corrosion and fatigue cracking at multiple sites.

After the accident Airworthiness Assurance Working Group (AAWG) was formed. Major contributions to improving the airworthiness of the aging fleet of transport aircrafts were made, including model specific reassessments of supplemental structural inspection programs or development of mandatory corrosion control programs. Moreover, Federal Aviation Administration (FAA) issued a special regulation proposing that older aircraft need at least one lifetime of the fatigue testing beyond the fleet leader. The purpose of this rule was to reduce a risk of problems with multiple site damage. Based on the regulation AAWG suggested performing a structural audit of each of the aging fleets. The work of the organisations resulted in creation of regulations dealing with widespread fatigue damage and a supporting advisory circular.

2.2 Description

Widespread fatigue damage is characterized by the simultaneous presence of cracks at multiple structural details of sufficient size and density, leading to not meeting the damage tolerance requirements. This global fatigue degradation might occur in a large structural element, i.e. row of fasteners connecting two skins of panels. Then we are talking about multiple site damage (MSD). Multiple element damage (MED) is characterized by degradation on multiple elements, such as adjacent stringers and frames. A description of MSD and MED is depicted in Figure 2.2.
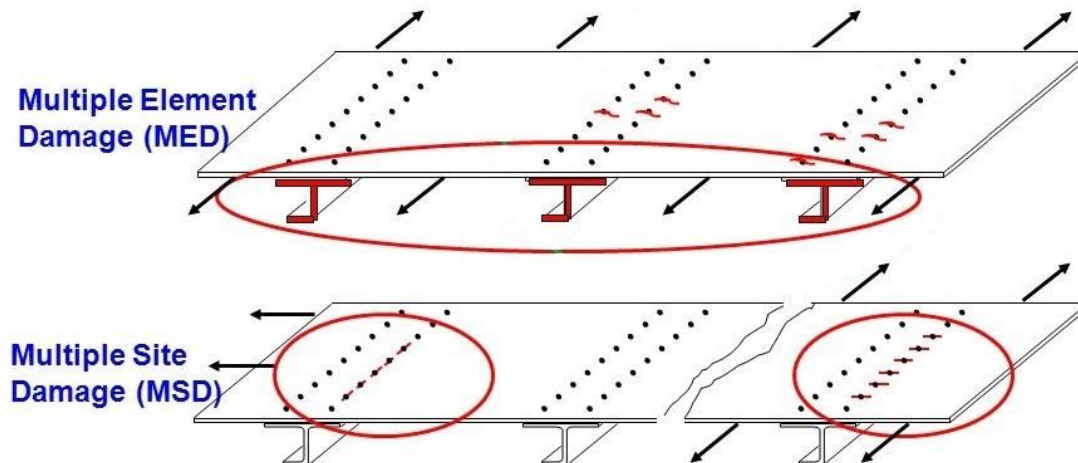
Figure 2.2 Description of MSD and MED [19]

MSD and MED cracks are typically too small to be reliably detected by standard inspection methods. Moreover, as it is depicted in Figure 2.3, the structure behaves as it was unflawed for a long time, but when multiple cracks link up (MSD case), a fast degradation of residual strength follows.

To avoid this undesired state, methods of evaluation of WFD are presented in Appendix 6 of AC 120-104. The task has two objectives: to predict when the WFD is likely to occur, and to establish additional maintenance actions to ensure safe operation of the airplane.
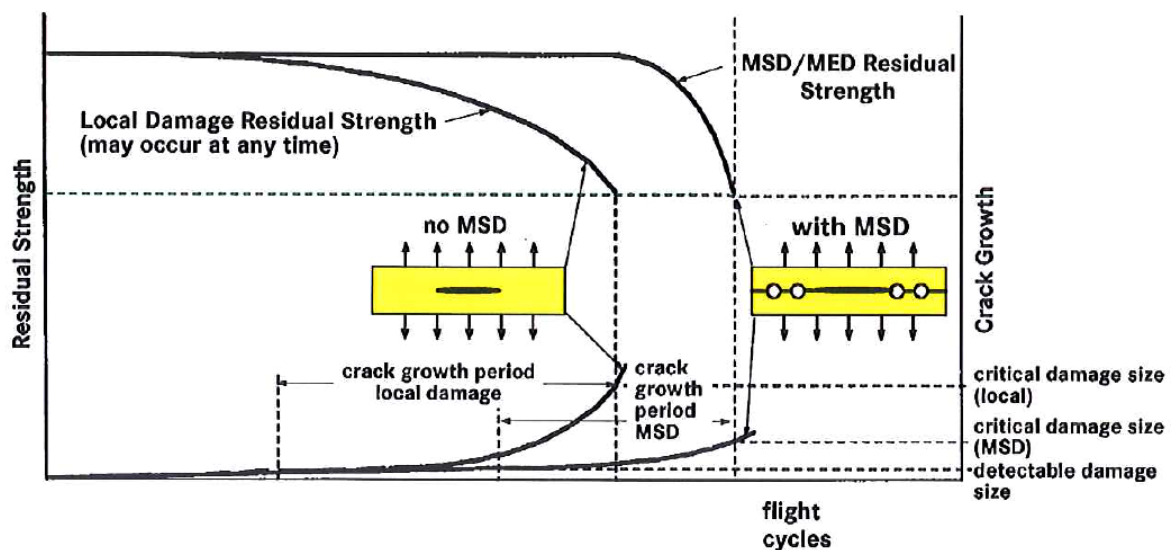
Figure 2.3 Residual strength of structure with local damage and MSD [10]

2.3 Susceptible areas

Some structures are more predisposed to occurrence of MSD or MED. Generally, areas with high amount of fasteners or stiffness transitions are of this kind. AC 120-104 suggests several structures of the wing to be susceptible to widespread fatigue damage presence. The list alongside with possible locations and main influencing factors is provided in Table 2.1. Geometries of such structures are displayed in Figure 2.4 to Figure 2.9.

Table 2.1 List of WFD susceptible areas for a wing structure

| Type of area	Possible locations	Influencing factors
Lap joints with milled, chem-milled or bonded radius (MSD)	Milled and chem-milled radius	High bending stresses due to excentricity
	Bonded doubler run-out	
	Abrupt cross-section change	
Abrupt changes in web or skin thickness (MSD/MED)	Milled and chem-milled radius	High stresses at edge supports due to structural deflections (non-pressure structure)
	Bonded doubler	
	Fastener row at edge support members	
	Edge support members in radius areas	
Skin at run-out of large doubler (MSD)	Cracks initiated at multiple critical fastener holes in skin at run-out of doubler	High load stransfer (high local stress)
Chord-wise splices (MSD/MED)	Chordwise critical fastener rows (MSD)	−High laod transfer −Local bending
	Fatigue critical fastener holes at stringer and/or fitting (MED)	
Rib-to-skin attachments (MSD/MED)	Critical fasteners in skin along rib attachments (MSD)	−Manufacturing deffect prestress due to assembly sequence −Sonic fatigue (empennage)
	Critical rib feet in multiple stringer bays (particularly for empennage in sonic fatigue - MED)	
Typical wing and empennage built-up construction (MSD/MED)	Rib attachment holes (MSD)	
	Drain and vent holes (MED)	
	Stiffener run-outs at root rib or tank end rib (MED)	
Typical wing and empennage integral construction (MSD/MED)	Rib attachment holes (MSD)	
	Drain and vent holes (MSD)	
	Stringer run-outs at root rib or tank end rib (MSD)	
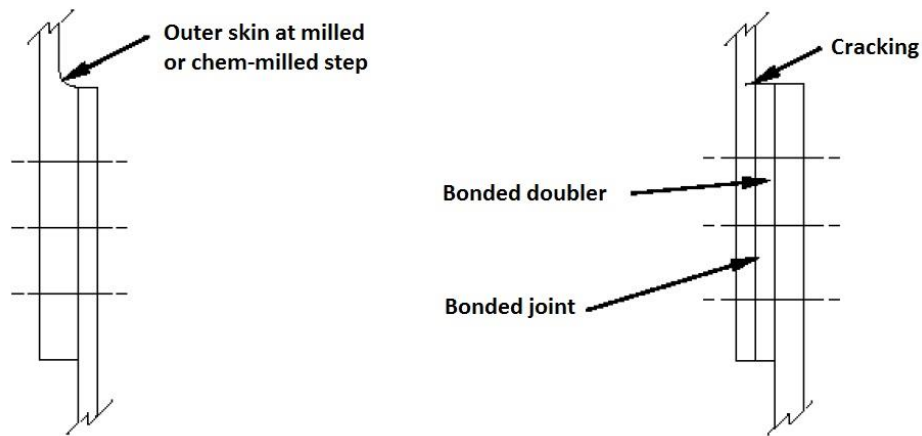
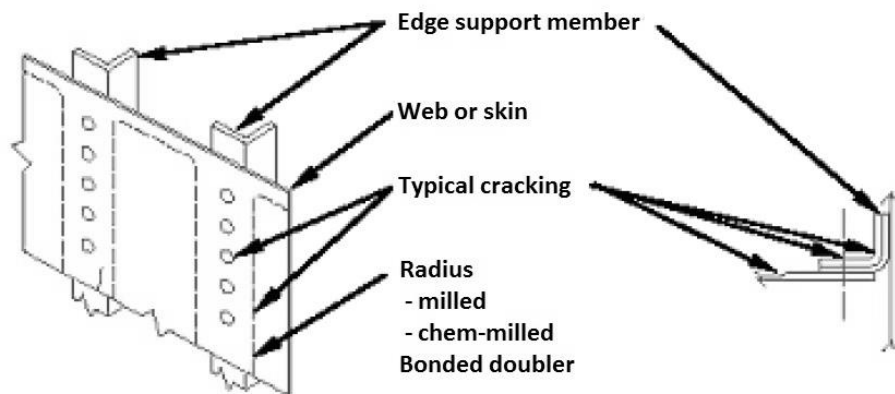**Figure 2.4 Lap joints with milled, chemically milled or bonded radius [12]**

Figure 2.5 Abrupt changes in web or skin thickness [12]
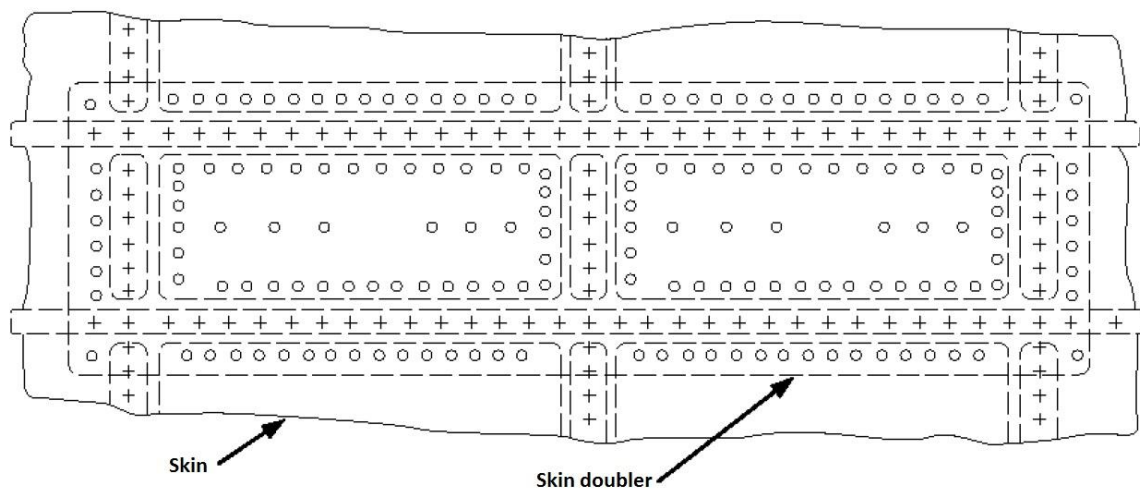

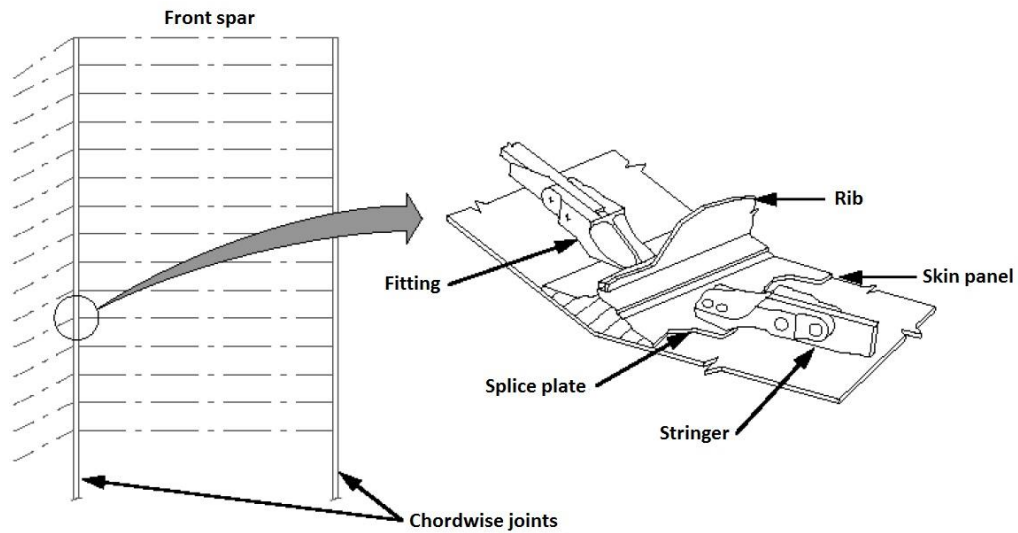**Figure 2.6 Skin at run-out of large doubler [12]**

9

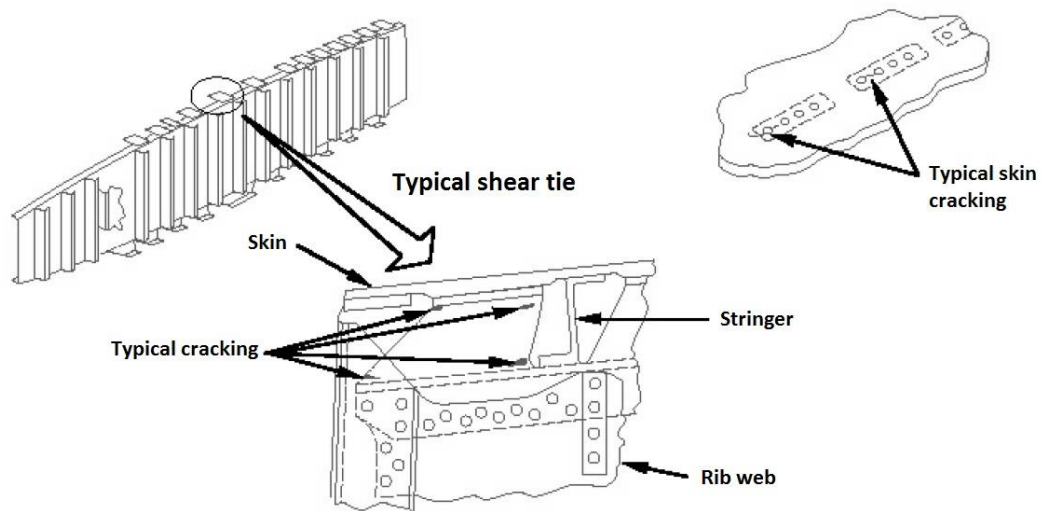**Figure 2.7 Chord-wise splices [12]**

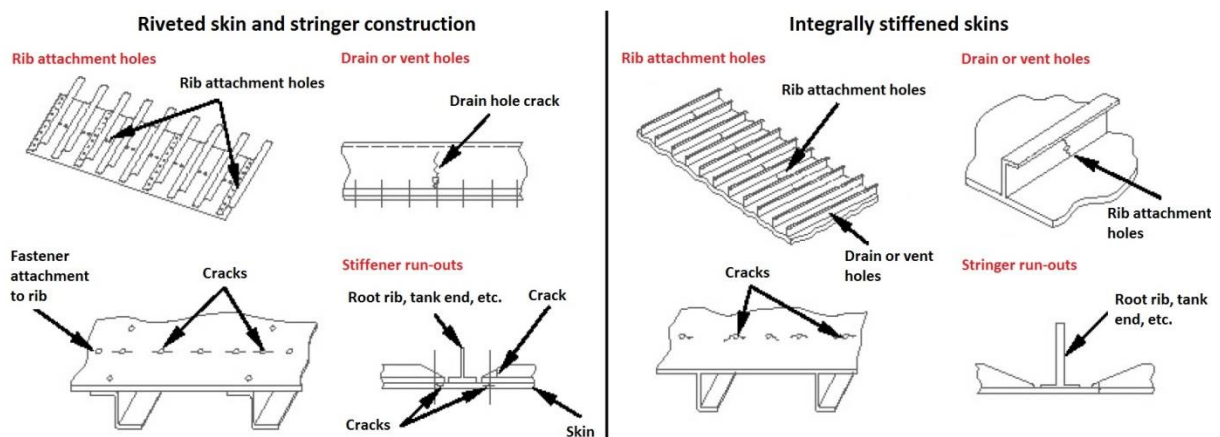**Figure 2.8 Rib-to-skin attachments [12]**

Figure 2.9 Typical wing and empennage construction (built-up and integral) [12]

2.4   Prediction of WFD occurrence

For any MSD or MED susceptible area it is important to define when WFD occurs. As shown in Figure 2.13, the moment can be described by a value of WFD average behaviour $WFD_{average}$ when, without intervention, 50 % of the fleet would have already experienced WFD in the considered area, i.e. the requirements on strength capability are no longer met by the structure.

For each WFD susceptible area (see chapter 2.3) WFD average behaviour should be estimated. A full-scale fatigue test and an analysis serve as a basis for such an estimate. Preferably, in-service history should be considered as well. In addition, test-to-structure factors are included in the assessment, which take into consideration possible differences in loading spectrum, boundary conditions, specimen configuration, material and geometric differences and environmental effects.

A crucial part of the analysis is to predict when and where cracks will initiate and how long will it take to stop meeting residual strength requirements.

2.4.1   Initial cracking scenario

It is the size and extent of multiple location cracking expected at the initiation of MSD or MED [12]. To predict the time to initiation, empirical data or an assumption based fatigue evaluation are necessary. There are two approaches to estimate crack size and position.

Equivalent initial flaw size (EIFS) is derived from the fatigue testing or tear-down inspections. A back extrapolation using the Paris law to zero cycles is made, giving thus a distribution of crack lengths in the very beginning.

Firstly, a distribution of time to crack initiation (TTCI), i.e. to some reference crack length, must be obtained. Then a compatible EIFS distribution can be constructed, as depicted in Figure 2.10. The compatibility was demonstrated for Weibull (normal being a special case of Weibull) and log-normal distributions [28]. The need of having a large number of test data to provide a reliable EIFS distribution is a disadvantage of the method.
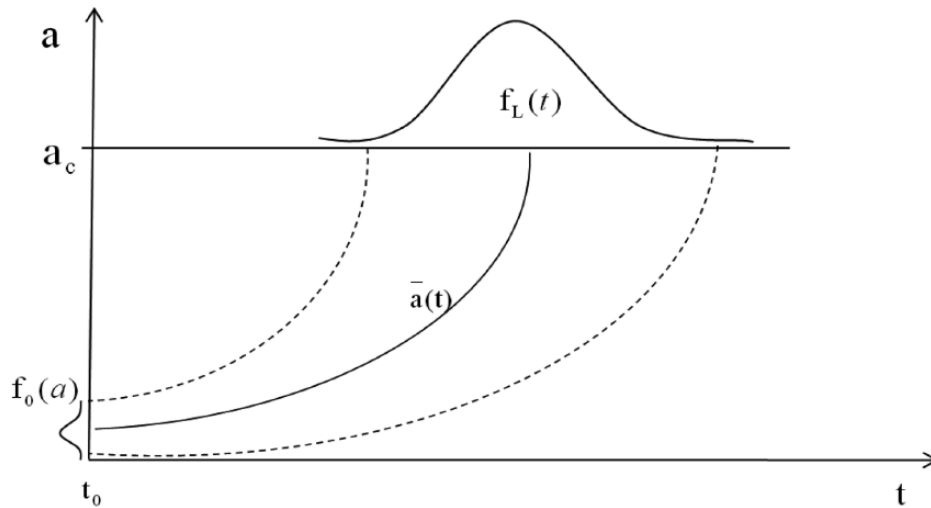
Figure 2.10 Process of compatibility between EIFS and TTCI distribution [28]

On the other hand, Schmidt [10] suggests sticking to the fixed initial crack length with a variable crack initiation time. Then we are searching for a point in the life of structure when the crack reaches this value. This is a result of the fatigue analysis of the structure. Randomized material data (S-N curve) are used to take into account the probabilistic nature of crack initiation time.

Despite Schmidt proposes using a single hole coupon data for S-N curve construction, an S-N curve shifting is suggested to account for a discrepancy between the time to fracture (as usual S-N

11

curve is constructed) and the time to detectable crack length, which Schmidt suggests to be 1 mm [10]. Modification of a time-to-fracture SN curve into time-to-crack-length based S-N curve is described in chapter 6.2.2.

After obtaining the time until crack initiation for each fastener, we can calculate initial damage in the structure with use of equation (2.1), where j is a number of a crack.

$$D_{init_j} = \frac{\min_{j} N_j}{N_j} \qquad\qquad (2.1)$$

Based on initial damage values we can determine where the first crack will initiate. If D_{init} = 1, then a crack is assumed. For any lower value more fatigue damage has to be accumulated before a crack initiates at given position, see an example shown in Figure 2.11. A mechanism of damage accumulation is described in chapter 6.4.
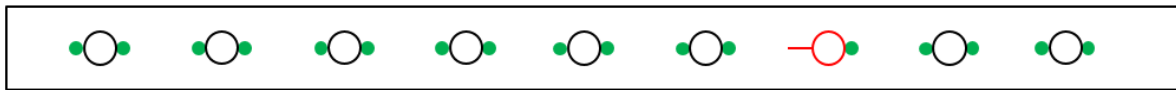
Figure 2.11 Initiation scenario based on initial damage [10];
red – initiated crack, green – damage accumulation in process

2.4.2   Crack growth

AC 120-104 suggests predicting crack growth in two ways:

 − empirically: from test evidence or fractographic data
 − analytically: typically based on linear elastic fracture mechanics;
                    see chapter 7 for more details

2.4.3   Crack interaction

For WFD analysis, including crack interaction is crucial. There are several differences in behaviour of structure with developed MSD or MED. Figure 2.12 shows the time to fracture of segments between the holes for structure with MSD and MED. Apparently, a presence of multiple site damage in the structure is more dangerous than for case of MED, yielding much faster crack growth compared to a single crack.

Analysis with assumption of MSD has to take into consideration several factors which have a high impact on its outcome [12]:

 − the flaw sizes assumed at initiation of the crack growth phase
 − material properties (static, fatigue, fracture mechanics)
 − ligament failure criteria
 − crack growth equations used
 − statistics used to evaluate fatigue behaviour of the structure (e.g. time to crack initiation)
 − methods of determining the structural modification point (SMP)
 − detectable flaw size assumed
 − initial distribution of flaws
 − factors used to determine lower-bound behaviour as opposed to mean behaviour

When assuming MED, it is necessary to consider crack interaction between two parts. The initiation of a crack in the element right next to the element with previously initiated crack is highly improbable. However, if this happens, a failure of two adjacent elements may negate any ability of the structure to withstand additional damage. To prevent this from happening, assuming such a scenario is recommended.
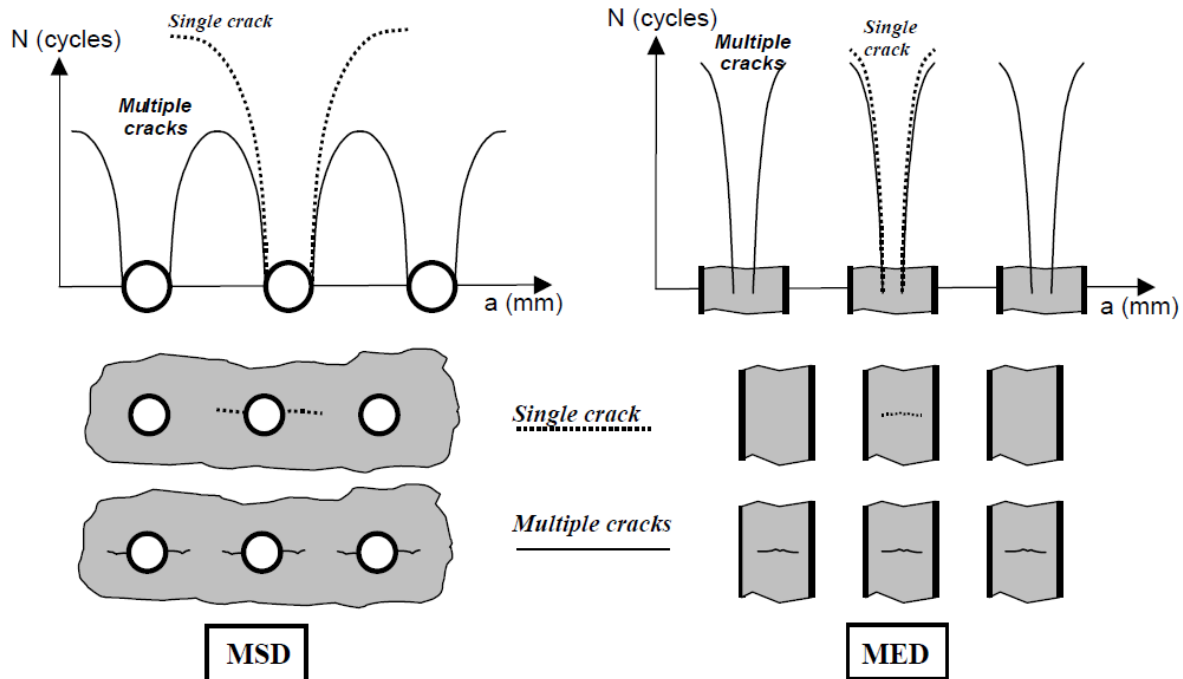
Figure 2.12 Comparison between MSD and MED interaction effects [12]

Because some structures are typically susceptible to both MSD and MED, the analysis for both the cases happening simultaneously should be performed, even though it is uncommon according to [12]. A comparison of ISP and MSP for separate analyses may indicate possibility of such an event. If so, interaction between MSD and MED should be included in the analysis.

2.4.4   Final cracking scenario

This is an estimate of extent of multiple location cracking, leading to diminution of residual strength below acceptable levels. AC 120-104 suggests employing the elastic-plastic analysis, however, due to its complexity, alternatives are proposed.

Defining the state before really critical condition is one of the approaches. An example of MSD is the occurrence of the first crack link-up in a row of fastener holes. Complexity of the analysis is reduced by using the sub-critical scenario. After all, because the most time to WFD is associated with crack initiation, the estimate is not reduced significantly.

2.5   Maintenance actions

Fatigue damage as a function of use can be statistically quantified. Hence, the end of the fatigue life, when the structure is no longer able to carry the residual strength loads, i.e. WFD, might be statistically quantified as well. That means there is always a chance that WFD might occur. Modifying or replacing the structure in advance helps with minimizing probability of such an event. The point of the maintenance action is derived from the analytically predicted time of WFD occurrence, and is called structural modification point (SMP).

Structural modification point is usually defined as a fraction of a moment when 50 % of a fleet would experience WFD for a given structure, i.e. WFD$_{average}$, giving a protection equivalent to two-lifetime fatigue test. The level of reliability of setting the SMP is acceptable provided MSD or MED inspections are effective in detecting cracks. These inspections should be implemented before the SMP; the first inspection is defined by the inspection start point (ISP). In case of ineffectiveness of inspections, SMP must be set at the time of the ISP.

ISP is defined based on statistical analysis of crack initiation based on fatigue test, tear-down inspections or in-service experience of similar structure. Alternatively, it might be defined as a fraction of the WFD average behaviour. Factors suggested by AC 120-104 for defining ISP as well as for SMP, are provided in Table 2.2.

Table 2.2 Factors for determining ISP and SMF based on the WFD$_{average}$

	Inspection effective	Inspection ineffective
Inspection start point	3	3
Structural modification point	2	3

After defining ISP, interval of inspections has to be established. This is dependent on the detectable crack size and the method of inspection.

If an inspection proves that structure is free from WFD, or on the contrary the cracks are found, further adjustment of SMP might take place. Both cases require an analysis of existing service data.
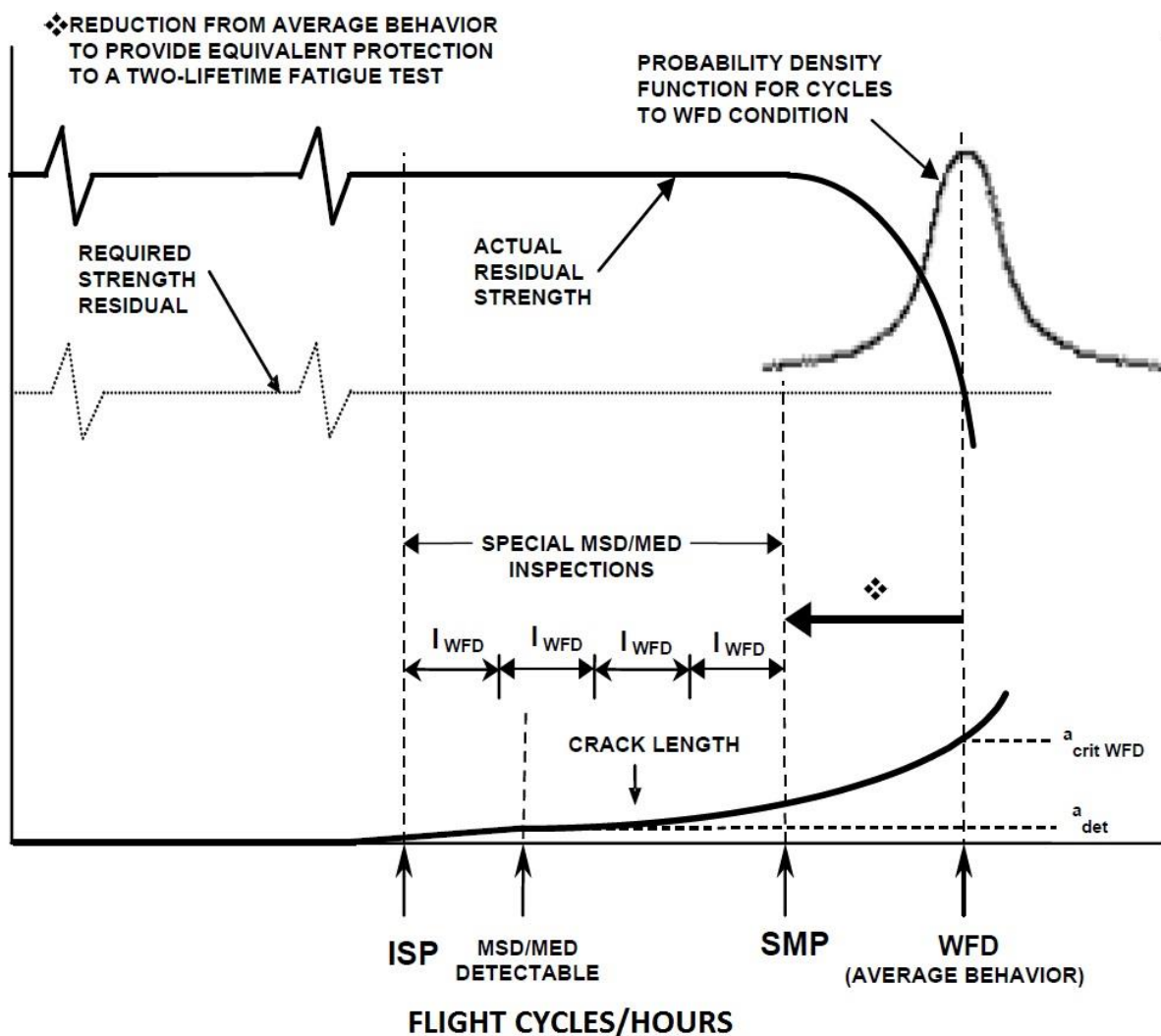
Figure 2.13 Residual strength curve, including WFD inspections [12]

2.6 Limit of validity

For airplanes certified in compliance with FAR 25, Amendment 125 or later, defining so called limit of validity (LOV) is required, beyond which the aircraft is not allowed to operate without repair, structural modification or replacement. It represents a period of time, up to which it has been demonstrated by fatigue tests, analysis and if available by teardown inspection results and service experience, that WFD is unlikely to occur in an airplane's model.

For L 410 NG airplane a fatigue test is planned to be run three times the design service goal (DSG) followed by a residual strength (RS) test. If all WFD susceptible areas successfully withstand the limit loads during the RS test, the LOV is claimed to be equal to the DSG and no further ISP or MSP would be required before reaching LOV.

3   Regulatory background

The L 410 NG airplane is certified in compliance with FAR 23 airworthiness regulations. However, regulations CS 23 issued by EASA are practically identical in the field of the damage tolerance and fatigue.

Airplanes certified in compliance with FAR 23 in category commuter are required by FAR 23.573 to fulfil the criteria on multiple site damage. Since no further regulations or advisory circulars related to WFD are introduced for this category, FAR 25 regulations must be taken into consideration as well.

3.1   FAR 23.573 Damage tolerance and fatigue evaluation of structure

(a) *Composite airframe structure*.

Does not apply for L 410 NG.

(b) *Metallic airframe structure*. If the applicant elects to use §23.571(c) or §23.572(a)(3), then the damage tolerance evaluation must include a determination of the probable locations and modes of damage due to fatigue, corrosion, or accidental damage**. Damage at multiple sites due to fatigue must be included where the design is such that this type of damage can be expected to occur**. The evaluation must incorporate repeated load and static analyses supported by test evidence. The extent of damage for residual strength evaluation at any time within the operational life of the airplane must be consistent with the initial detectability and subsequent growth under repeated loads. The residual strength evaluation must show that the remaining structure is able to withstand critical limit flight loads, considered as ultimate, with the extent of detectable damage consistent with the results of the damage tolerance evaluations. For pressurized cabins, the following load must be withstood:

(1) The normal operating differential pressure combined with the expected external aerodynamic pressures applied simultaneously with the flight loading conditions specified in this part, and

(2) The expected external aerodynamic pressures in 1g flight combined with a cabin differential pressure equal to 1.1 times the normal operating differential pressure without any other load.

3.2   FAR 23.574 Metallic damage tolerance and fatigue evaluation of commuter category airplanes.

For commuter category airplanes

(a) *Metallic damage tolerance*. An evaluation of the strength, detail design, and fabrication must show that catastrophic failure due to fatigue, corrosion, defects, or damage will be avoided throughout the operational life of the airplane. This evaluation must be conducted in accordance with the provisions of § 23.573, except as specified in paragraph (b) of this section, for each part of the structure that could contribute to a catastrophic failure.

(b) *Fatigue (safe-life) evaluation*.

Does not apply for WFD susceptible areas.

3.3 14 CFR 26.21 Limit of validity

(a) *Applicability*.

Definition of aircrafts which must comply with this regulation.

(b) *Limit of validity*. Each person identified in paragraph (c) of this section must comply with the following requirements:

(1) Establish a limit of validity of the engineering data that supports the structural maintenance program (hereafter referred to as LOV) that corresponds to the **period of time**, stated as a number of total accumulated flight cycles or flight hours or both, **during which it is demonstrated that widespread fatigue damage will not occur in the airplane**. This demonstration must include an evaluation of airplane structural configurations and be supported by test evidence and analysis at a minimum and, if available, service experience, or service experience and teardown inspection results, of high-time airplanes of similar structural design, accounting for differences in operating conditions and procedures. The airplane structural configurations to be evaluated include—

(i) All model variations and derivatives approved under the type certificate; and

(ii) All structural modifications to and replacements for the airplane structural configurations specified in paragraph (b)(1)(i) of this section, mandated by airworthiness directives as of January 14, 2011.

(c) *Persons who must comply and compliance dates*.

(d) *Compliance plan*.

(e) *Compliance dates for compliance plans*.

(f) *Compliance plan implementation*.

(g) *Exceptions.*

4 Monte Carlo method

4.1 Description

Complex problems such as failure prediction require a powerful tool to solve them. One such a tool is hidden under Monte Carlo (MC) methods. These algorithms are based on repeating the calculation with randomized inputs and ensuing statistical analysis. By the law of large numbers, after repeating the experiment a sufficient number of times, an average value of the results should be close to an expected value. In terms of MSD analysis, the expected value is the average time to WFD ($WFD_{average}$).

In Figure 4.1 there is a description of the MC method algorithm displayed. Input data comprise of geometry of the specimen, applied loads and material properties. In effect, all of mentioned inputs are of probabilistic nature. No two products are manufactured identical and no forces loading the structure are the same. Aside from scatter of loads (which is treated separately and is not subject of the thesis), the most significant random behaviour originates in a manufacture of semi-products, parts and assemblies. While the variances in the semi-products manufacture cause material to have different static, fatigue and crack growth properties, defects originating in parts and assemblies manufacture influence significantly fatigue properties of the structure.

These macroscopic defects, along with microscopic material defects, when loaded cyclically, lead to a future fatigue crack creation. The crack initiation is the main object of Monte Carlo sampling, since describing the process would be a noticeably complex task.

After sample data are generated, a deterministic part of the simulation takes place. The crack growth prediction gives a value of cycles to fracture of the structure. If the mean of the values from all MC simulation runs is within desired convergence bounds, the simulation stops and proceeds to post-processing data: determining WFD average behaviour, defining inspection intervals etc. Otherwise new sample data are generated based on input data and simulation runs until a convergence criterion is met.
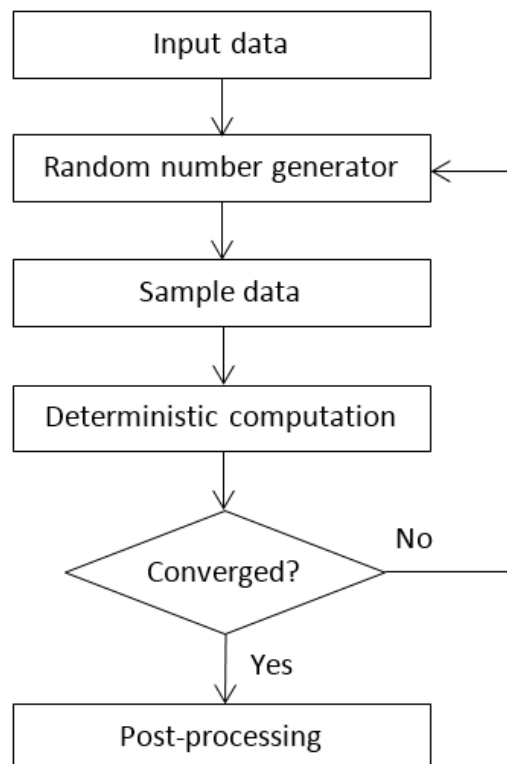

Figure 4.1 Monte Carlo method flow chart

4.2 Random number generator

The pivot of the sample generation is using a random number generator (RNG). There are two basic types of RNG: true-random and pseudo-random generators.

True-RNG measures some physical phenomenon that is expected to be random and then compensates errors of measurements. Toss of a coin or a dice, measurements of acoustic or thermal noise are examples of such phenomena.

Pseudo-RNG uses an algorithm to generate numbers that are apparently random. For the MSD analysis a Matlab built-in function *normrnd* was utilised to generate normally distributed data based on mean and standard deviation provided by material tests. This function uses the Mersenne Twister algorithm [27]; for more details about the algorithm see reference [30].

4.3 Convergence

As it was stated in chapter 4.1, a large amount of runs of the MC simulation is required to obtain desired value. A crucial task is to determine when the results of the simulation are satisfying enough and the simulation can stop. According to Ata [8], estimating a sample size requires knowledge of the usually unknown process variance.

There are two main types of MC procedures. Fixed-sample-size procedures rely on generating an adequate number of samples, usually multiples of 100, so desired confidence interval (CI) is always satisfied.

However, this leads to redundant runs of the simulation, costing a computational time. Because of this, Ata [8] in his 'acceptable shifting convergence band rule' (ASCBR) suggests employing a sequential CI procedure. The length of the simulation is then sequentially increased until an acceptable CI is reached. This interval should not be too strict, because it leads to a large number of simulation runs to satisfy the criterion. On the other hand, too loose CI might stop the calculation before the convergence was achieved.

Ata suggests using a confidence band (CB) instead of confidence interval in the usual statistical sense. Certainly, an acceptable confidence interval (ACI) estimated according to (4.1) is much larger than the range of fluctuating midpoints of actual CI, i.e. the MC sample mean.

$$ACI = z_{\alpha/2}\sqrt{s_n^2/n} \tag{4.1}$$

where n is number of MC runs, s_n^2 a sample variance and $z_{\alpha/2}$ is $\alpha/2$-quantile of normal distribution.

Let ε be the half-width of the acceptable range for the sample means. Then sequential interval covering the sample means is written as the equation (4.2) shows, where U and L are upper or lower bounds respectively. If a user does not define it, AIMA uses a thousandth of the mean of the first ξ runs as default (defined later in this chapter). As it turned out, it is a good compromise between the computational time demands and the accuracy.

$$U(\bar{x}_j) = \begin{cases} U(\bar{x}_{j-1}) \\ \bar{x}_j + \varepsilon \end{cases} \qquad L(\bar{x}_j) = \begin{cases} L(\bar{x}_{j-1}) \\ \bar{x}_j - \varepsilon \end{cases} \qquad \begin{aligned} &\text{if} \quad \delta_j = 1 \\ &\text{if} \quad \delta_j = 0 \end{aligned} \tag{4.2}$$

where

$$\delta_j = \begin{cases} 1 & \text{if} \quad \bar{x}_j \in \left(L(\bar{x}_{j-1});\ U(\bar{x}_{j-1}) \right) \\ 0 & \text{if} \quad \bar{x}_j \notin \left(L(\bar{x}_{j-1});\ U(\bar{x}_{j-1}) \right) \end{cases} \tag{4.3}$$

The number of adjacent MC means that comply with the CB defined by upper and lower limits (U, L) is defined in eq. (4.4). Afterwards, the value is compared to the desired confidence band length ξ. The recommended confidence band length is 50 or more. When the parameter z achieves the size of confidence band length, a desired sample mean value defined by U and L for the n-th run is confirmed to be valid also for next $\xi - 1$ runs. Naturally, this is the moment when the simulation stops. The core of the stop criterion is depicted in Figure 4.2. An estimate of sample mean from the point C is proved to be valid.

$$z_j = \begin{cases} z_{j-1} + 1 & \text{if } \delta_j = 1 \\ 0 & \text{if } \delta_j = 0 \end{cases} \qquad (4.4)$$
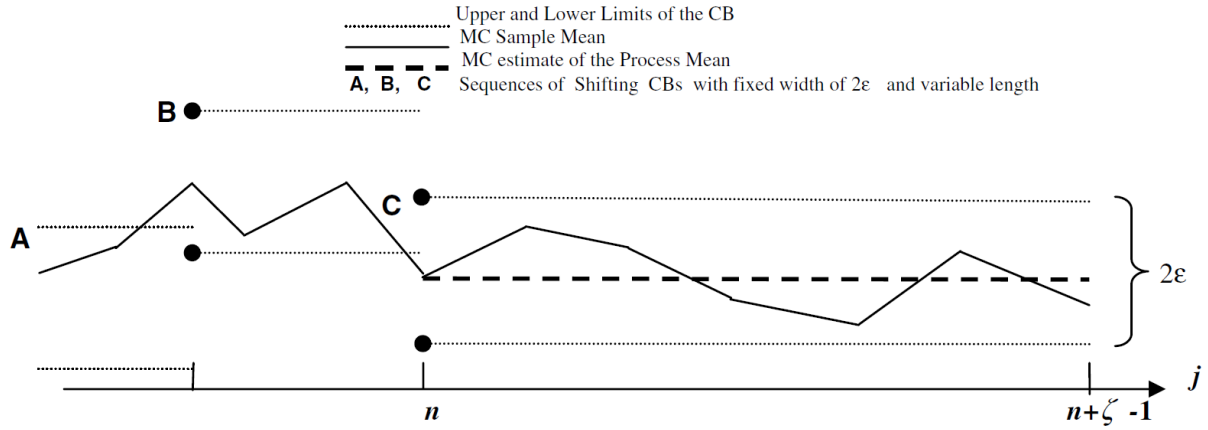
Figure 4.2 Description of acceptable shifting convergence band rule (ASCBR) [8]

4.4 Post-processing

After the simulation comes to an end, obtained results have to be processed. By the central limit theorem [8], for a sufficient large number of independent random variables, the mean of the population is approximately normally distributed regardless of the source distribution.

That means that the probability of failure of the structure due to WFD is approximately normally distributed. The normal distribution is characterized by two parameters: mean μ and variance s^2. To find a probability for a certain value, e.g. probability of WFD occurrence in our case, a cumulative probability distribution function (CDF) is constructed, for definition see eq. (4.5). An example is provided in Figure 4.3; a point estimate of mean displayed.

Because values of the mean and the variance are not at disposal, point estimates of the values are quantified, see equations (4.6).

$$F(n) = \frac{1}{s\sqrt{2\pi}} \int_{-\infty}^{n} e^{-\frac{(t-\mu)^2}{2s^2}} dt \qquad (4.5)$$

$$\mu \approx \frac{1}{n}\sum_{i=1}^{n} x_i \qquad\qquad s^2 \approx \frac{1}{n-1}\sum_{i=1}^{n}(x_i - \mu) \qquad (4.6)$$

Figure 4.3 Cumulative probability distribution for WFD occurrence
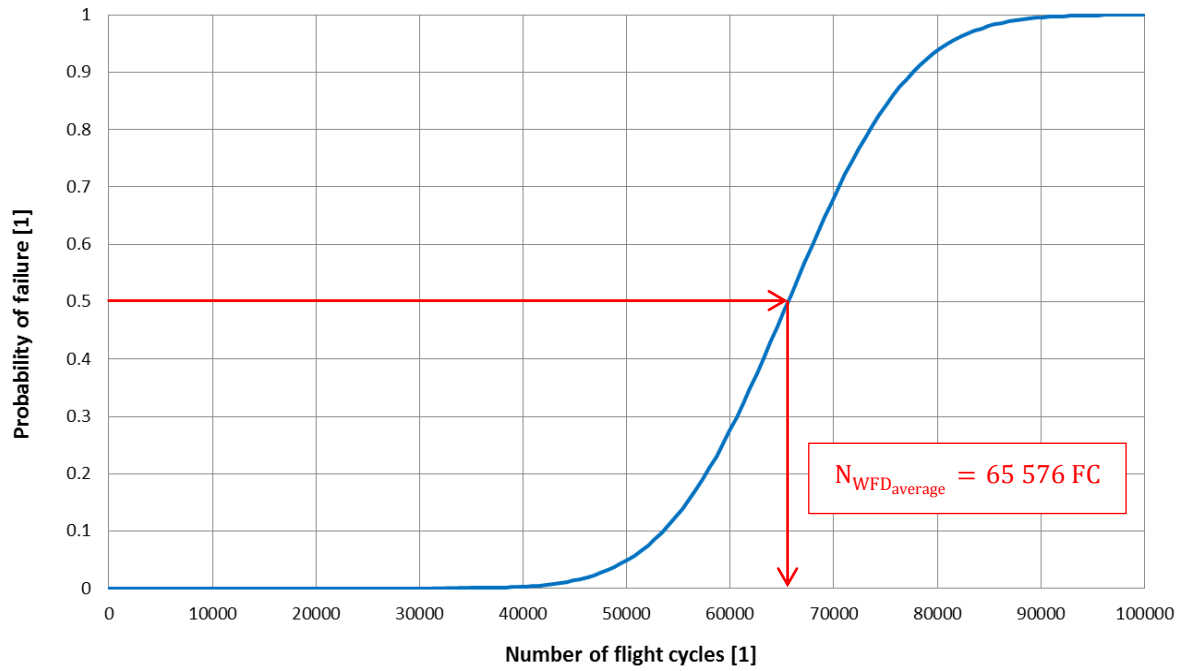
4.5   Computational time

When performing the Monte Carlo simulation, required computational time plays a big role due to large required number of runs. A computational time analysis was performed to evaluate influence of the geometry and applied loading. Ten runs were performed for each stress level for geometry with 4 fasteners and for varying geometry with constant load 80 MPa. Fasteners of identical diameter were being added with the same spacing. Geometry of the test specimen (4 fasteners) is displayed in Figure 10.6. Calculation was performed using Matlab on CPU Intel Core i3 M350 @ 2.27 GHz 2.27 GHz.

As shown in Figure 4.4, computational time is strongly dependent on the applied load. Unfortunately, for low stress levels typical for fatigue critical structures the most time is required. Particularly when it depends on the stress with a power of 2.5014, as a data fit in Figure 4.4 indicates. It is interesting to point out the exponent value, which is very close to the exponent of Forman equation (see chapter 7.1 for more details) for given material (n_f = 2.83). The relation between speed of the crack growth and required number of cycles for the fracture to occur is apparent. On the other hand, a dependence on the number of fasteners is not so significant, see Figure 4.5.

To shorten computational time, using a CPU with higher performance is suitable. For further improvement, the code could be modified so it allows parallel computing. Another way, probably with the highest impact, would be rewriting into a compiled code like C, C++ or FORTRAN. Matlab supports a code written in these languages in a form of mex-files.
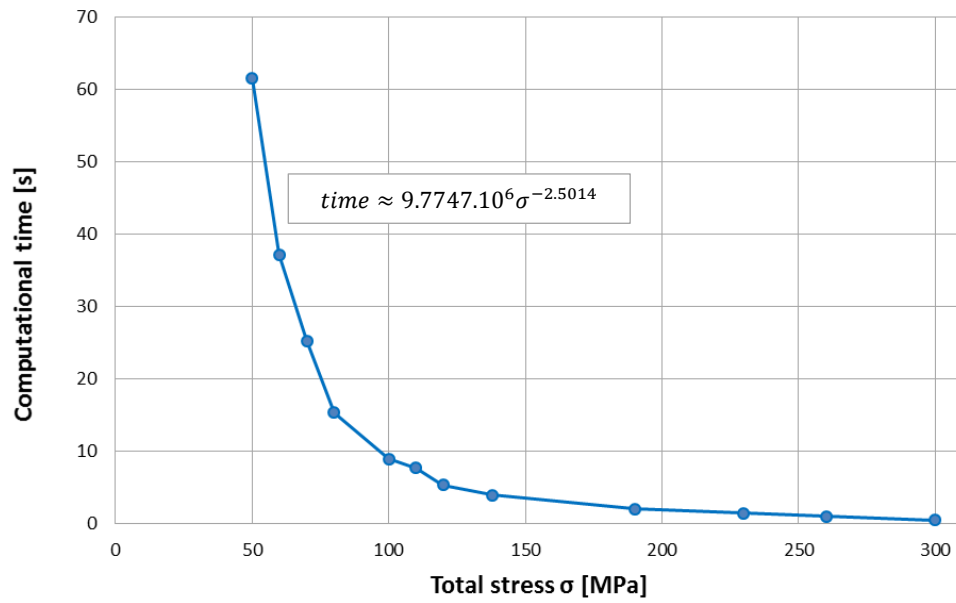
21

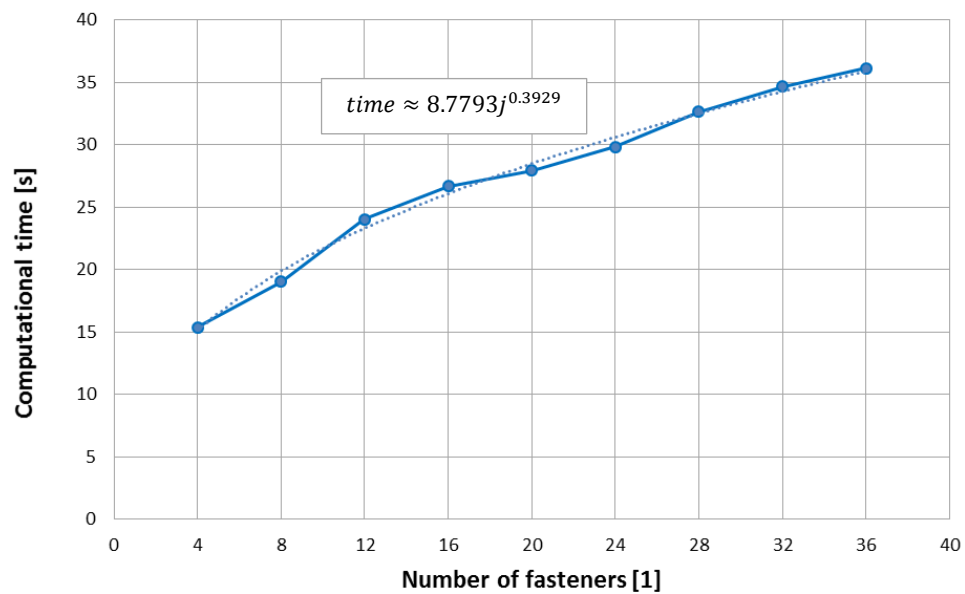**Figure 4.4 Dependence of computational time on applied remote stress at the specimen with four fasteners**

Figure 4.5 Dependence of computational time on number of fasteners for remote stress 80 MPa;
***j* is number of fasteners**

5 Stress calculation

For fatigue and MSD analysis, knowing the stress distribution in the structure is essential. Inputs might be obtained by analytical calculation, as a result of the experiment or by finite element method (FEM). For gaining total stress level at a fastener, approach suggested by TsAGI [24] is used in Aircraft Industries. The stress at the fastener is calculated as a superposition of by-pass stress (axial), secondary bending stress and pin load stress.

$$\sigma_{tot} = \sigma_{by-pass} + \sigma_b + \sigma_p \tag{5.1}$$

5.1 Pin load stress

Stress due to pin load effects is gained by a relation proposed by [24]. It comprises of pin load in direction of the by-pass stress P_L and the pin load in direction transverse to the by-pass stress P_T.

$$\sigma_p = 0.45\,\frac{P_L}{d\,t} + 0.1\,\frac{P_T}{d\,t} \tag{5.2}$$
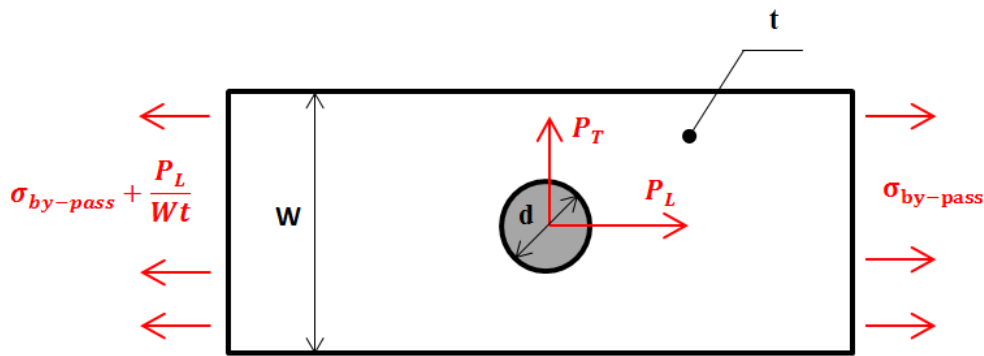
Figure 5.1 Geometry of the specimen for pin load stress determination

5.2 Secondary bending

If the structure is loaded eccentrically, it is loaded additionally by bending stress in attempt to get acting forces in one plane. The secondary bending is calculated according to Euler-Bernoulli beam theory, taking advantage of knowledge of pin forces. Bending moment is defined by moment – curvature relation [17], as well as a relation between transferred force and out-of-neutral-line displacement.

$$M_b = E\,J\,\frac{d^2 w}{dx^2} \tag{5.3}$$

$$M_b = F\,w \tag{5.4}$$

where E – Young's modulus, J – second moment of inertia, w – displacement from the neutral line, x – distance along the beam, F – total transferred force.

Combining (5.3) and (5.4) following differential equation is obtained:

$$\frac{d^2 w}{dx^2} - \alpha^2\,w = 0 \tag{5.5}$$

where $\alpha^2 = F/(E\,J)$.

Solution to (5.5) and its first derivative are known in this form:

$$w = A \sinh(\alpha x) \; + \; B \cosh(\alpha x) \qquad\qquad (5.6)$$

$$\frac{dw}{dx} = B\alpha \sinh(\alpha x) \; + \; A\alpha \cosh(\alpha x) \qquad\qquad (5.7)$$

The amount of necessary boundary conditions is $2(n+1)$, where n is number of section force and stiffness transitions. An example based on geometry shown in Figure 5.2 and Figure 5.3 is presented in Table 5.1. e represents neutral line jump. For symmetrical joint there is one stiffness transition (change of thickness of the bottom part) and one section force change due to a fastener, for asymmetrical just two fasteners, thus n = 2 and number of boundary conditions is 6 for both joints.

Table 5.1 Boundary conditions for joints shown in Figure 5.2 and Figure 5.3

Symmetrical joint	Asymmetrical joint	Description
$x_1 = 0$: $w_1 = 0$		Clamped end
$\left(\dfrac{dw}{dx}\right)_{1,x_1=L_1} = \left(\dfrac{dw}{dx}\right)_{2,x_2=0}$		Rotations on both sides are the same
$w_2(x_2 = 0) = w_1(x_1 = L_1) + e_1$		Neutral line jump due to thickness change
	$w_2(x_2 = 0) = w_1(x_1 = L_1) + e_1$	Neutral line jump due to fastener presence
$\left(\dfrac{dw}{dx}\right)_{1,x_1=L_1} = \left(\dfrac{dw}{dx}\right)_{2,x_2=0}$		Rotations on both sides are the same
$w_3(x_3 = 0) = w_2(x_2 = L_2) + e_2$		Neutral line jump due to fastener presence
$\left(\dfrac{dw}{dx}\right)_{1,x_3=L_3} = 0$		Symmetry axis: zero rotation
	$x_3 = L_3$: $w_3 = \delta$	Displacement δ related to the origin ($x_1 = 0$)
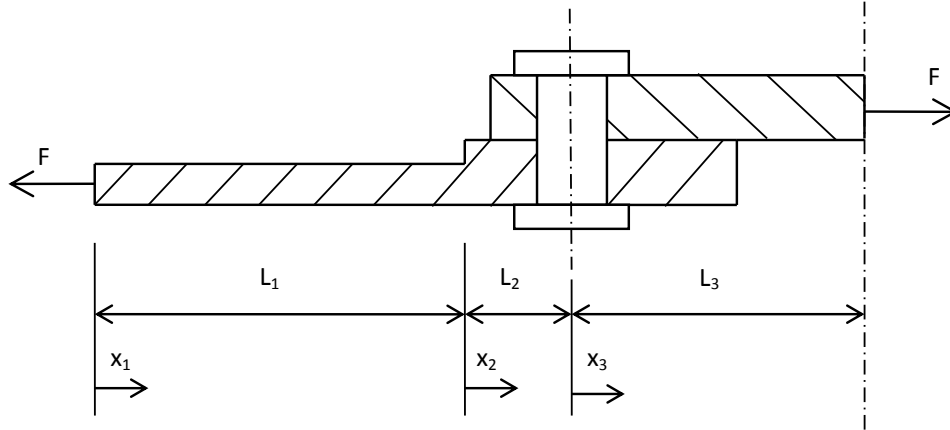
Figure 5.2 Geometry of the symmetrical joint of two sheets
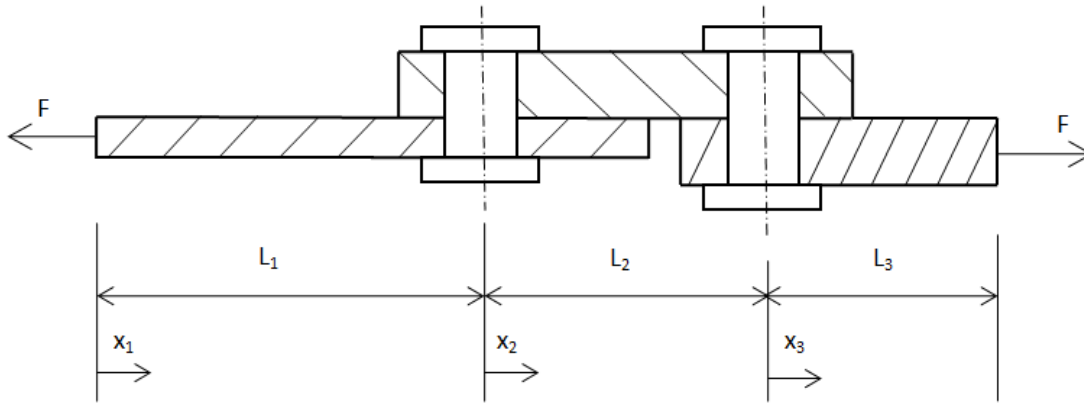
Figure 5.3 Geometry of the asymmetrical joint of two sheets

After applying the boundary conditions on equations (5.6) and (5.7) we get a system of linear equations, with CA_i and CB_i as variables in following form:

$$\begin{bmatrix} AC & AS \\ Sn & Cn \end{bmatrix} \begin{bmatrix} CA_1 \\ \dots \\ CA_{n+1} \\ CB_1 \\ \dots \\ CB_{n+1} \end{bmatrix} = \begin{bmatrix} Z \\ -e_1 \\ \dots \\ -e_n \\ BC \end{bmatrix} \tag{5.8}$$

where:

$$BC = \begin{cases} \left(\dfrac{dw}{dx}\right)_{1,x_{n+1}=L_{n+1}} = 0 & \text{if symmetrical} \\[2em] (w_{n+1})_{x_{n+1}=L_{n+1}} = \delta & \text{if asymmetrical} \end{cases}$$

Z is a column vector of zeros with length $n+1$; δ represents relative displacement between the ends in direction perpendicular to the beam midline. Sub-matrices are all $(n+1)$ x $(n+1)$ large and are presented in Table 5.2. Coefficients C and S represent hyperbolic sine and cosine at ends of intervals:

$$C_i = \cosh(\alpha_I\, L_i)$$

$$S_i = \sinh(\alpha_I\, L_i)$$

25

Table 5.2 Definition of sub-matrices from equation (5.8) for symmetrical and asymmetrical joint

	Symmetrical joint	Asymmetrical joint
AC	$\begin{bmatrix} \alpha_1 C_1 & -\alpha_2 & 0 & 0 & \dots & 0 & 0 & 0 \\ 0 & \alpha_2 C_2 & -\alpha_3 & 0 & \dots & 0 & 0 & 0 \\ \dots & \dots & \dots & \dots & \dots & \dots & \dots & \dots \\ 0 & 0 & 0 & 0 & \dots & 0 & \alpha_n C_n & -\alpha_{n+1} \end{bmatrix}$	$\begin{bmatrix} \alpha_1 C_1 & -\alpha_2 & 0 & 0 & \dots & 0 & 0 & 0 & 0 \\ 0 & \alpha_2 C_2 & -\alpha_3 & 0 & \dots & 0 & 0 & 0 & 0 \\ \dots & \dots & \dots & \dots & \dots & \dots & \dots & \dots & \dots \\ 0 & 0 & 0 & 0 & \dots & 0 & \alpha_n C_n & -\alpha_n & 0 \\ 0 & 0 & 0 & 0 & \dots & 0 & 0 & 0 & 0 \end{bmatrix}$
AS	$\begin{bmatrix} \alpha_1 S_1 & 0 & 0 & \dots & 0 & 0 \\ 0 & \alpha_2 S_2 & 0 & \dots & 0 & 0 \\ \dots & \dots & \dots & \dots & \dots & \dots \\ 0 & 0 & 0 & \dots & 0 & \alpha_{n+1} S_{n+1} \end{bmatrix}$	$\begin{bmatrix} \alpha_1 S_1 & 0 & 0 & \dots & 0 & 0 & 0 \\ 0 & \alpha_2 S_2 & 0 & \dots & 0 & 0 & 0 \\ \dots & \dots & \dots & \dots & \dots & \dots & \dots \\ 0 & 0 & 0 & \dots & 0 & \alpha_n S_n & 0 \\ 1 & 0 & 0 & \dots & 0 & 0 & 0 \end{bmatrix}$
Cn	$\begin{bmatrix} C_1 & -1 & 0 & 0 & \dots & 0 & 0 & 0 \\ 0 & C_2 & -1 & 0 & \dots & 0 & 0 & 0 \\ \dots & \dots & \dots & \dots & \dots & \dots & \dots & \dots \\ 0 & 0 & 0 & 0 & \dots & 0 & C_n & -1 \\ 1 & 0 & 0 & 0 & \dots & 0 & 0 & 0 \end{bmatrix}$	$\begin{bmatrix} C_1 & -1 & 0 & 0 & \dots & 0 & 0 & 0 \\ 0 & C_2 & -1 & 0 & \dots & 0 & 0 & 0 \\ \dots & \dots & \dots & \dots & \dots & \dots & \dots & \dots \\ 0 & 0 & 0 & 0 & \dots & 0 & C_n & -1 \\ 0 & 0 & 0 & 0 & \dots & 0 & 0 & C_{n+1} \end{bmatrix}$
Sn	$\begin{bmatrix} S_1 & 0 & 0 & \dots & 0 & 0 & 0 \\ 0 & S_2 & 0 & \dots & 0 & 0 & 0 \\ \dots & \dots & \dots & \dots & \dots & \dots & \dots \\ 0 & 0 & 0 & \dots & 0 & S_n & 0 \\ 0 & 0 & 0 & \dots & 0 & 0 & 0 \end{bmatrix}$	$\begin{bmatrix} S_1 & 0 & 0 & \dots & 0 & 0 & 0 \\ 0 & S_2 & 0 & \dots & 0 & 0 & 0 \\ \dots & \dots & \dots & \dots & \dots & \dots & \dots \\ 0 & 0 & 0 & \dots & 0 & S_n & 0 \\ 0 & 0 & 0 & \dots & 0 & 0 & S_{n+1} \end{bmatrix}$

By solving the system (5.8) and putting resultant coefficients *CA* and *CB* into equation (5.6), displacements *w* for each region are obtained. Inserting the results into equation (5.4), bending moment for each fastener *i* at part *k* is calculated at each region. To stay conservative, the maximum value of bending moment from areas adjacent to the fastener is chosen, i.e. maximum of stresses at $x_i = L_i$ and $x_{i+1} = 0$.

$$M_{b_{i,k}} = F \max\left\{\frac{(EJ)_{i,k}}{\left((E_{eff}J)\right)_i} CA_i \, sinh(\alpha_i L_i) + CB_i \, cosh(\alpha_i L_i) \; ; \; \frac{(EJ)_{i+1,k}}{\left(E_{eff}J\right)_{i+1}} CB_{i+1}\right\} \tag{5.9}$$

where *(EJ)$_{i,k}$* is a bending stiffness for segment *i* and part *k*; *(E$_{eff}$ J)$_i$* is bending stiffness for whole section for segment *i*; *E$_{eff}$* is effective Young's modulus for whole section, see eq. (5.10).

$$E_{eff} = \frac{\sum A_k E_k}{\sum A_k} \tag{5.10}$$

Bending stress is then calculated as a ratio between bending moment and the first moment of area (rectangular cross-section assumed):

$$\sigma_b = \frac{M_b}{\frac{1}{6} B_f \, t^2} \tag{5.11}$$

where *B$_f$* for given column is calculated as an average of size *B* of adjacent segments.

26
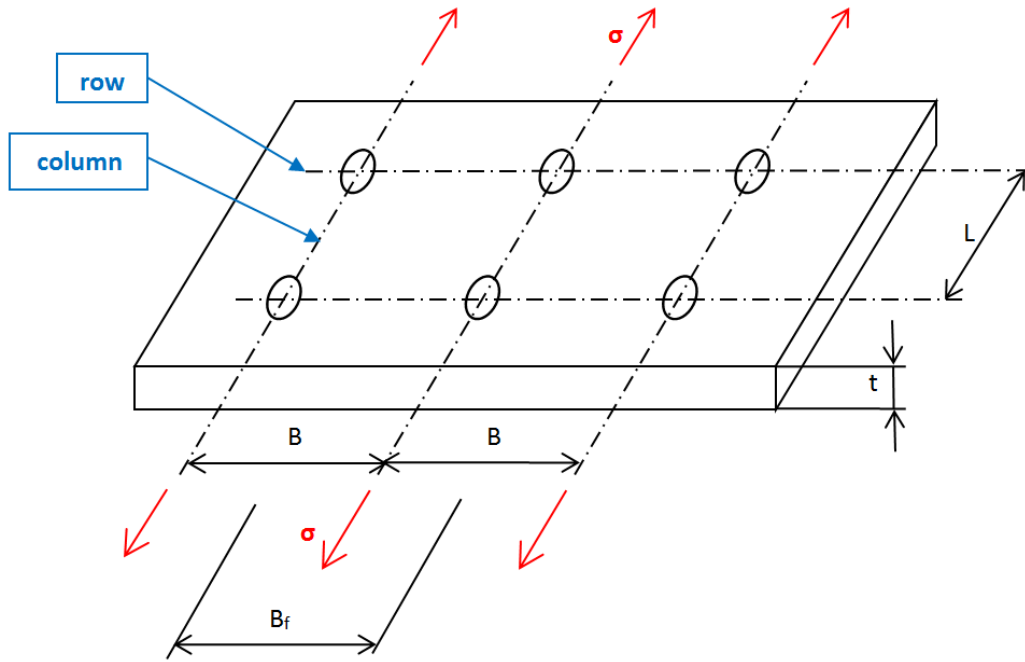
Figure 5.4 Notation of inter-fastener dimensions and terminology of fastener sets

5.3   Stress concentration factor

In a structure, it is generally hard to avoid having geometrical notches, such as holes. The notches cause inhomogeneous stress distribution leading to local increase of stress, see Figure 5.5. This amplification might be described using a factor representing the ratio between maximum (peak) stress and either nominal stress or by-pass stress, see (5.12). This factor depends on geometry and mean of loading of the structure. Since in AIMA uniaxial loading is assumed, only geometry matters. Solutions by Peterson [14] used in the analysis are presented further in the chapter.

$$K_{t_n} = \frac{\sigma_{max}}{\sigma_{nom}} \qquad\qquad K_{t_g} = \frac{\sigma_{max}}{\sigma} \qquad\qquad (5.12)$$
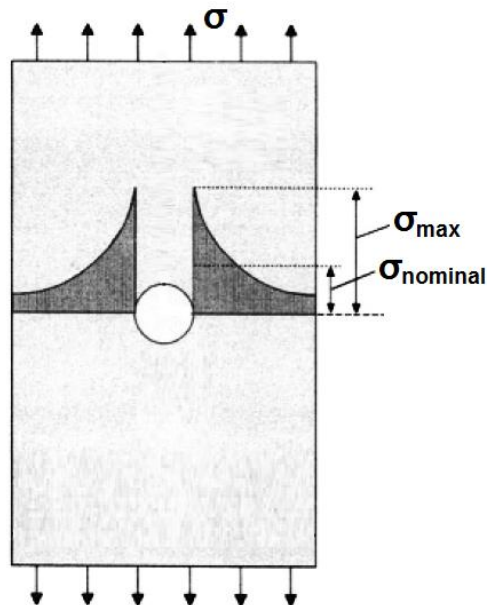
Figure 5.5 Stress concentration factor definition [16]

Circular hole in an infinite plate $\qquad K_{t_g} = 3$ $\qquad$ *(5.13)*

Elliptic hole in an infinite plate $\qquad K_{t_g} = 1 + \dfrac{2a_e}{b_e} = 1 + 2\sqrt{a_e/r}$ $\qquad$ *(5.14)*

U-shaped notch in a semi-finite plate $\qquad K_{t_g} = 0.855 + 2.21\sqrt{t_U/r}$ $\qquad$ *(5.15)*

Figure 5.6 Geometry of a row of circular holes in an infinite plate

Figure 5.7 Geometry of an elliptic hole in an infinite plate
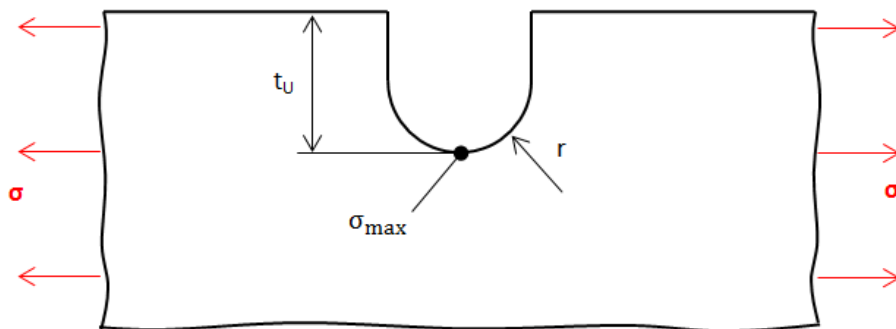
Figure 5.8 Geometry of a U-shaped notch in a semi-finite plate

28

6 Fatigue calculation

6.1 Introduction

As a fatigue is a matter of a long time, several stages of fatigue life can be defined, as displayed in Figure 6.1. The crack initiation period is of great importance when evaluating the fatigue life of a structure, because it takes significant portion of time, i.e. an error has the greatest impact on results. Description and asse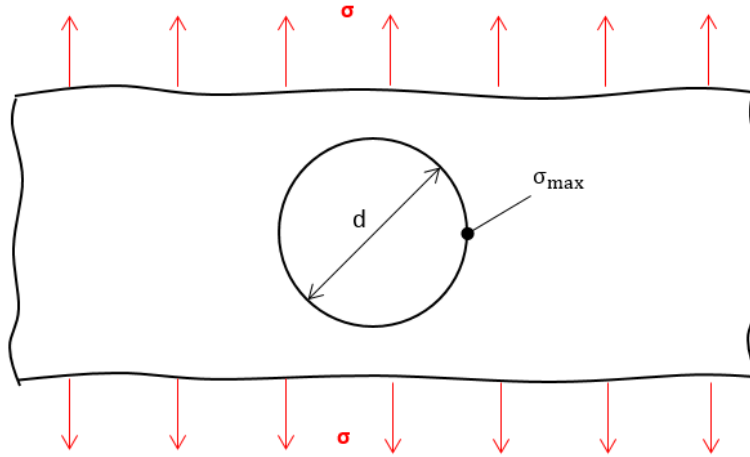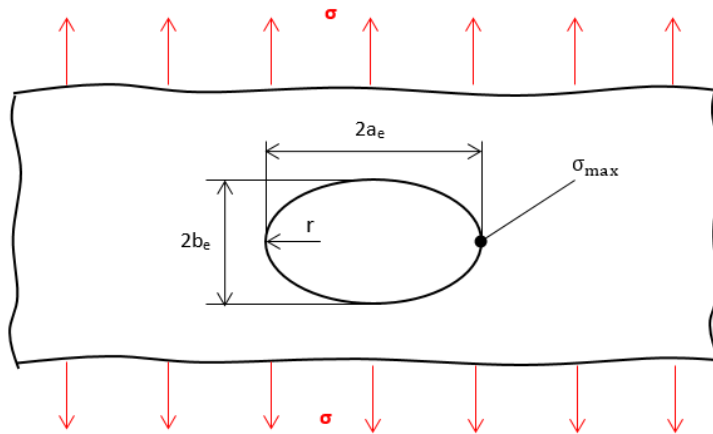ssment of the structure during this period is a core of the chapter. For detailed description of crack growth period and failure, see chapters 7 or 9, respectively.
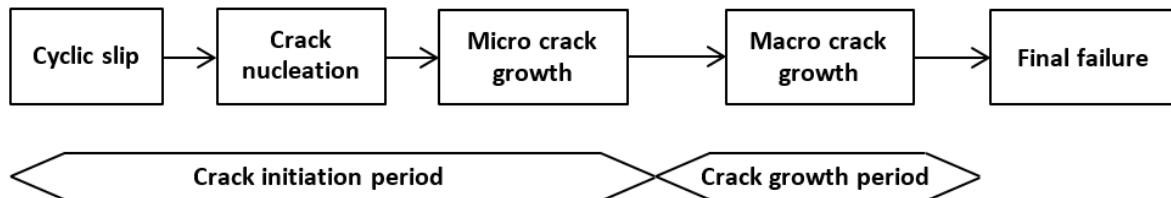
Figure 6.1 Fatigue life stages [16]

Fatigue crack initiation is a consequence of cyclic slip in slip bands. As a result of moving of dislocations, a plastic deformation in a micro-scale driven by a shear stress occurs. The quality of a material surface (e.g. roughness) is crucial during this stage, since any discontinuities create space for further micro-plastic deformation. Because the crack initiation mechanism itself is not subject of the thesis, for deeper study of cyclic slips and crack nucleation, reference [16] is recommended.
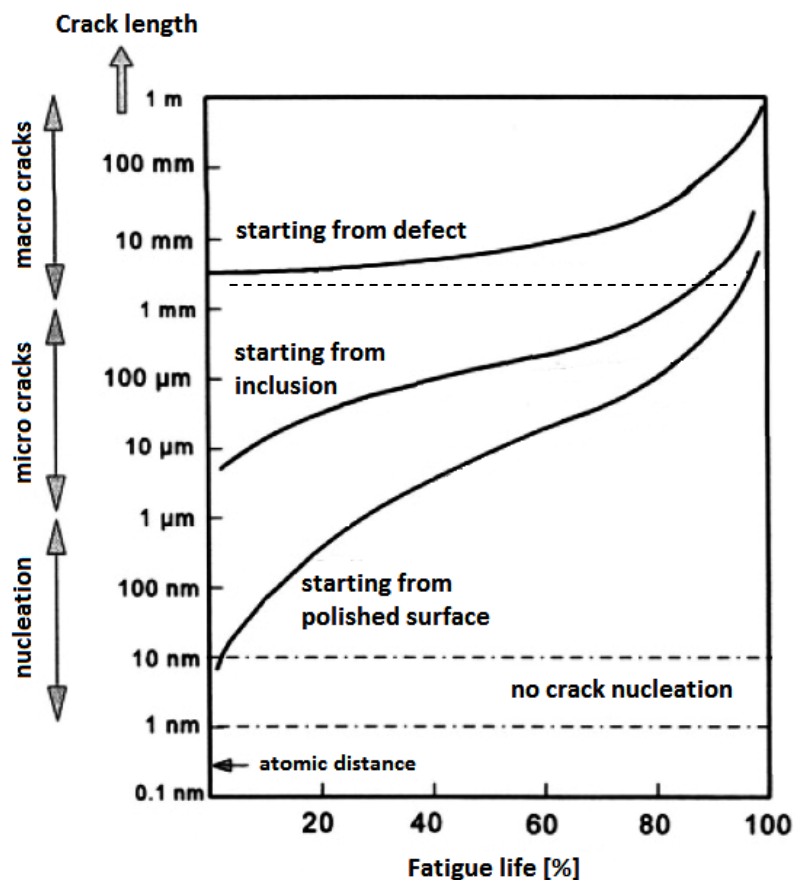
Figure 6.2 Length of crack initiated in various ways during fatigue life [16]

In Figure 6.2 lengths of crack originated at various surfaces during a fatigue life are displayed. It is clear that micro-cracks starting from the clear surface have size below 1 μm in the beginning of the fatigue life. In case of cracks starting from an inclusion, their size is comparable with the size of the inclusion, which may be still in sub-millimetre range. An example of inclusions in the material is impurities introduced during the melting production of the alloys. For cracks originating from a macroscopic defect the size can be of detectable length. In typical wing structure considered defects include material flaws, defects originating in drilling holes, flaws created during riveting etc.

Other important information emerging from the figure is the length of fatigue life with crack length below 1 mm. This value is typically believed to be a border between micro and macroscopic crack size, since a micro-crack growth no longer depends on the free surface conditions. Apparently, the major part of the fatigue life is spent here for the cracks starting from the clean surface or an inclusion. This leads to two conclusions:

- presence of material or manufacturing defects should be avoided
- accurate evaluation of fatigue life until the crack length is detectable is necessary

6.2 S-N curve

6.2.1   Definition

Stress levels in typical aircraft structures are usually low, meaning that so called high-cycle fatigue methods well describe the fatigue life of the structure. A parameter generally associated with the high-cycle fatigue is a Wöhler's curve, also known as S-N curve (Stress vs. Number of cycles). It displays a relation between the stress in a structure and number of cycles until a fatigue failure occurs. For application in the MSD analysis, a shifted S-N curve describing the period until a crack becomes macroscopic, i.e. 1 mm long, is derived.

To assemble the S-N curve a series of test at various stress levels is necessary to perform. The tests may be performed on test coupons, resulting in a material S-N curve, or on specimens representing a structural node. Afterwards, with employing regression methods a curve is obtained. Typically a linear model comparing the life with the stress in logarithmic scale is used. The curve can be then described by an equation (6.1), or (6.2) in non-logarithmic form. Typical confidence level used for sample data regression is 50 % or 95 %. For purposes of crack initiation in the MSD analysis, the mean curve is used for generating scenarios of Monte Carlo simulation.

$$\log N = \log A - m \log \sigma \qquad\qquad (6.1)$$

$$N = \frac{A}{\sigma^m} \qquad\qquad (6.2)$$

where *A* and *m* are parameters of the curve and are constants for given confidence level for a given material or a structural node.

For some materials, e.g. steel or titanium alloys, a stress level below no macro-cracks are initiated (fatigue limit) is typically defined. For another, such as aluminium, the limit does not exist, but the S-N curve slope may change for lower stresses. To consider this effect, the curve definition for the region below and over a certain number of cycles N_{knee}, so called S-N curve knee, may differ. Stress level associated with the cycle count is a knee stress σ_{knee}.

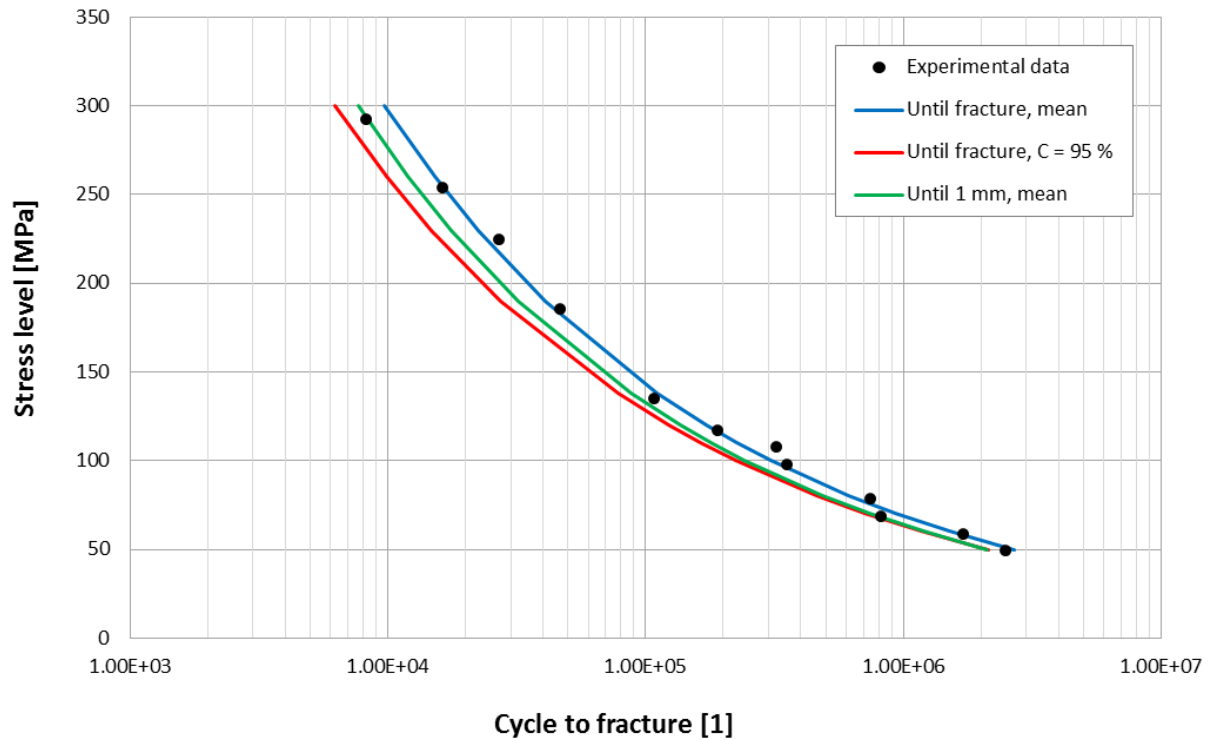## 6.2.2   S-N curve for detectable crack length

Figure 6.3 SN curve for a bottom panel splice joint based on data from [15]; C = confidence level

An example of an S-N curve for a bottom panel splice joint [15] is displayed in Figure 6.3. Alongside with experimental data and fitted curves, a shifted mean curve until a crack reaches length 1 mm with is displayed. To modify the curve, following procedure employing backwards extrapolation is performed. AFGROW or other crack growth software can be utilised.

1. Create model of the specimen in such way that expected crack growth will take the longest possible time. This includes assuming the crack to initiate as close as possible to the centre of the specimen and holes are substituted by the original material (presence of holes speeds up crack growth). Initial crack length is set to 1 mm, as we are searching for the S-N curve until crack reaches length 1 mm. An appropriate substitution is depicted in Figure 6.4.
2. Subtract time of the crack growth (from 1 mm long crack until fracture) from the time to fracture according to the test. This way we obtain time until the first crack with length 1 mm appears.
3. Regression of calculated shifted data to define a new S-N curve; or alternatively, define a coefficient of shifting n_{det}.

The shifting coefficient n_{det} defines the ratio between number of cycles for given stress level of shifted S-N curve and original curve, and its use is supported by AIMA. Downside of this approach compared to defining a new S-N curve is that all times to fracture are shifted by the same coefficient for all stress levels. Therefore, the minimum of n_{det} calculated for every stress level is recommended to use.
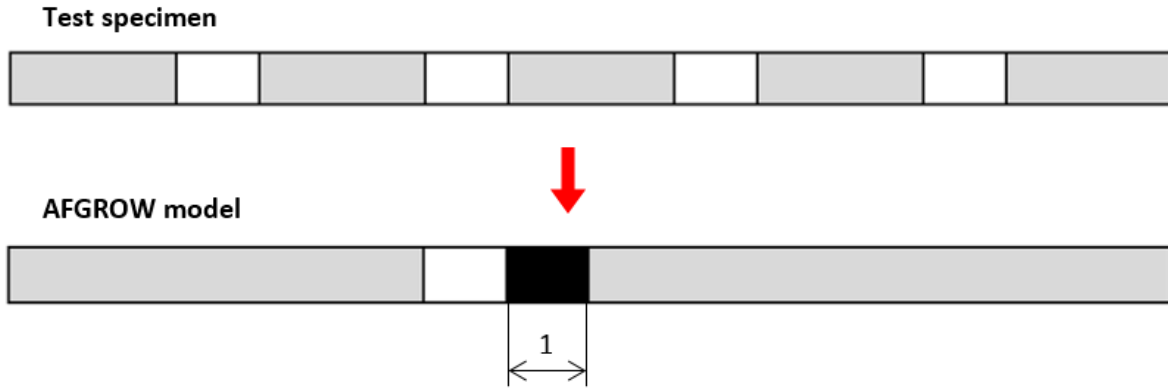
Test specimen

AFGROW model

1

Figure 6.4 Substitution of original test specimen geometry by a model geometry for calculation of a shifted S-N curve (cycles until 1 mm crack); Dimensions in [mm]

6.2.3   Scatter of data

As visible from Figure 6.3, the fitted curve does not fully correspond to the experimental data. Data for every stress level are fitted to the logarithmic lives with assumption of normal distribution. The scatter of data is described then by a logarithmic standard deviation of the S-N curve s_{log}. Apparently, the probability distribution of the S-N curve is log-normal. This fact serves as a basis for Monte Carlo simulation of MSD analysis. While calculated stress levels are deterministic (apart from randomness of material properties), number of cycles N until a crack becomes macroscopic, i.e. 1 mm long, is of stochastic nature. For purposes of MC simulation, N is determined by a following equation:

$$N = 10^{\log(A/\sigma^m)+f_N s_{log}}$$
<div align="right">(6.3)</div>

where f_N is a random number of standardized normal distribution expressing number of standard deviations from the mean. The AIMA algorithm utilises Matlab's function *normrnd* to create random logarithmic life based on the mean and standard deviation:

```
N = 10^normrnd( log10( A / S^m ) , s_log )
```

where S is stress σ and *s_log* is logarithmic standard deviation s_{log}.

6.2.4   Correction for mean value

The procedure of calculating life based on the loading stress presented in previous chapter utilises only one value. Depending on the S-N curve definition, it can be a stress amplitude for a cycle with zero mean stress, or it might be a maximum value of a cycle pulsating between zero and stress σ. However, there exist several types of cycles with various mean σ_m and amplitude σ_a, see chapter 6.3. The mean stress and amplitude are calculated as follows:

$$\sigma_m = \frac{\sigma_{max} + \sigma_{min}}{2} \qquad\qquad \sigma_a = \frac{\sigma_{max} - \sigma_{min}}{2}$$
<div align="right">(6.4)</div>

Now a question arises, how do we utilise the S-N curve to calculate fatigue life if there are two stress values at disposal – maximum and minimum stress (or stress mean and amplitude)? The answer is an application of some correction for mean value, which transforms a cycle into the cycle with zero mean, or into the cycle pulsating between value σ_{puls} and zero (Oding), see Figure 6.5. The most often used are shown in Figure 6.6. The diagram describes whether the fatigue failure occurs at the same number of cycles for the cycle with given mean and amplitude. If a point $[\sigma_m, \sigma_a]$ lies above the defined curve, failure occurs.

According to Yahr [33], the best compliance with reality for high-strength aluminium alloys is achieved by use of Gerber correction. Goodman correction is often used because of its simple definition. Both Soderberg and Oding corrections are relatively conservative. In spite of that, Oding correction is utilised in the MSD analysis, since stresses in the wing structure typically pulsate in tension. After all, this is a method used for fatigue analyses of wing structures in AI. For definition see equation (6.5).

$$\sigma_{puls} = \begin{cases} \sqrt{2\,\sigma_a\,(\sigma_a + \sigma_m)} & \text{if } \sigma_m \geq 0 \\ \sqrt{2}\,(\sigma_a + 0{,}2\sigma_m) & \text{if } \sigma_m < 0 \ \& \ \sigma_m + \sigma_a > 0 \\ 0 & \text{if } \sigma_m + \sigma_a < 0 \end{cases} \qquad (6.5)$$

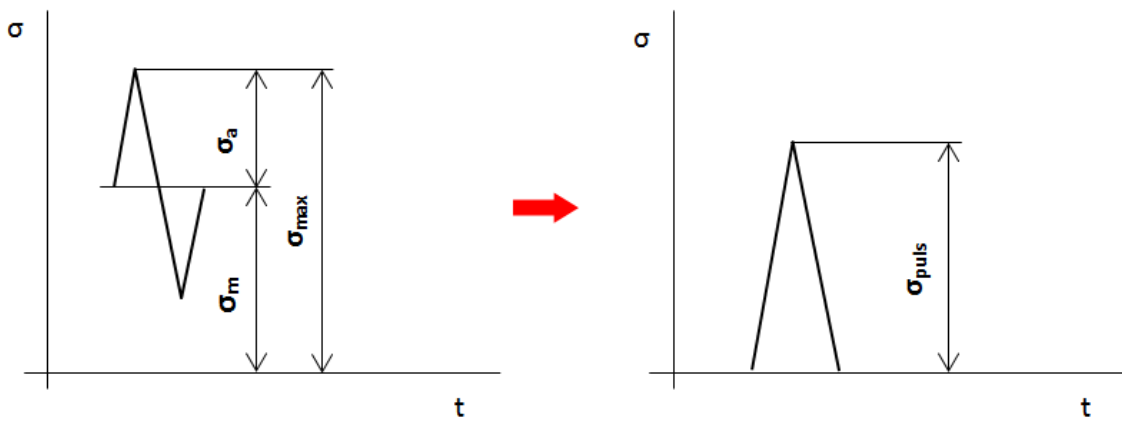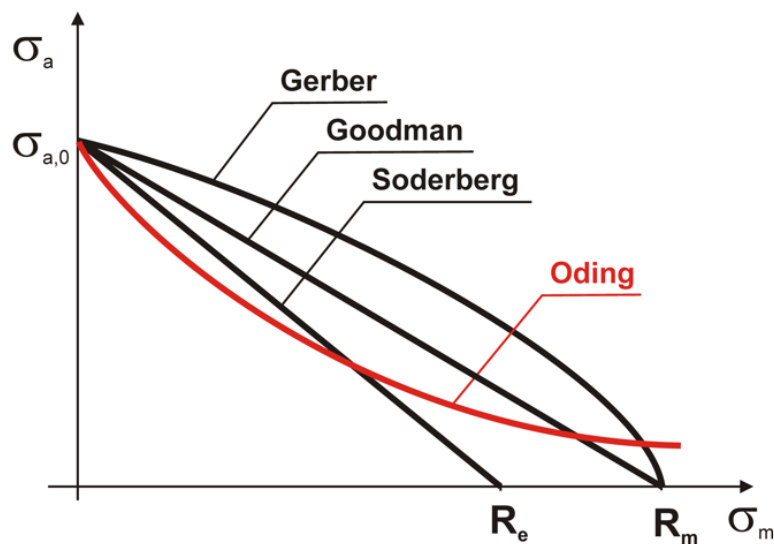**Figure 6.5 Definition of σ$_{puls}$ as follows from Oding correction**

Figure 6.6 Curves describing mean stress effects on fatigue life [19];
σ$_a$ – stress amplitude, σ$_m$ – mean stress, R$_e$ – yield strength, R$_m$ – ultimate strength

6.3 Variable amplitude loading

6.3.1 Cycle types

There are several types of cycles, as presented in Figure 6.7.

A — fully pulsating in compression $R \in (1, \infty)$

B — pulsating in compression $R = \pm\infty$

C — alternating asymmetrical (mean in compression) $R \in (-\infty, -1)$

D — alternating symmetrical $R = -1$

E — alternating asymmetrical (mean in tension) $R \in (-1, 0)$

F — pulsating in tension $R = 0$

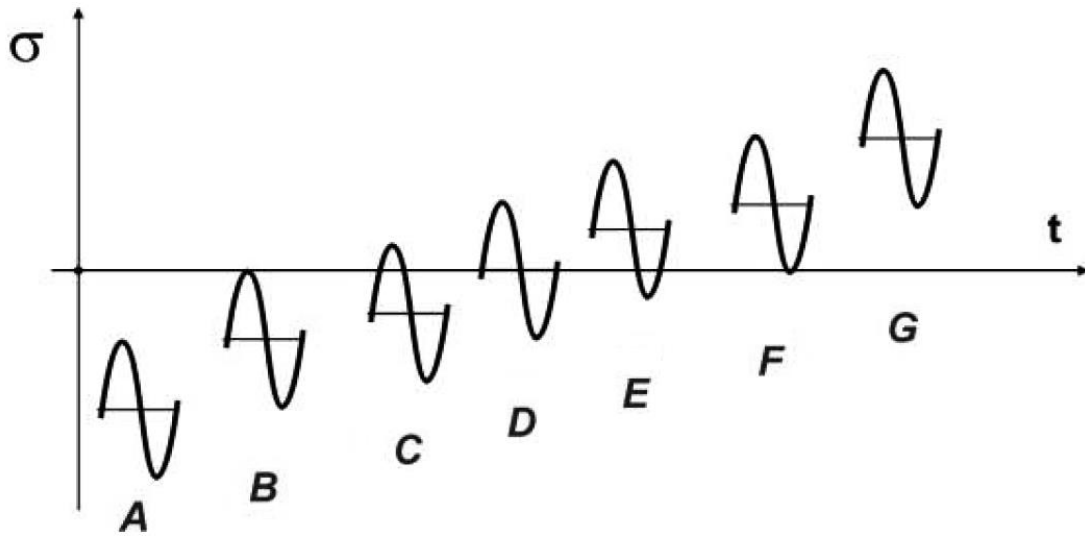G — fully pulsating in tension $R \in (0, 1)$

Figure 6.7 Cycle types [19]

The value R is so called asymmetry of the cycle. While its value does not play a big role in fatigue calculation, it is essential part of a Forman equation used for crack growth prediction (see chapter 7.1). It is defined as a ratio between maximum and minimum stress value of the cycle:

$$R = \frac{\sigma_{min}}{\sigma_{max}} \qquad (6.6)$$

6.3.2 Cumulative damage

Until now, loading of structure by cycles with constant mean and amplitude was considered. However, in practice this is a rare situation. Structures are typically loaded by series of cycles with variable mean stress and amplitude. To calculate fatigue life of the structure under this kind of loading, employing a cumulative damage model is necessary. The most widely used model (and the simplest) is a Palmgren-Miner rule (often just Miner rule) [34], written in form:

$$\sum_{i=1}^{N} \frac{n_i}{N_i} = c \qquad (6.7)$$

where n is number of cycles accumulated in given stress level, N is number of cycles to fatigue failure at given stress level, c is fraction of life consumed. In general, if damage fraction reaches 1, failure occurs.

Because the Miner rule is a simple rule, several limitations apply. Firstly, for "high-low" fatigue tests it is proved that failure occurs for c < 1, i.e. the rule is non-conservative. However, for tests with random loading history, a very good correlation is observed. A major limitation of the rule is not considering sequence effects, i.e. the order of cycles does not play a role. Finally, the linear life-stress relation assumed by the rule may not well describe reality in many applications.

6.3.3   Flight spectra

Loads typical for aircraft structure are variable. For fatigue calculation so called flight spectra are usually utilised. These spectra define the magnitude of the loads acting on the structure and probability of their occurrence. Load spectra of the L 410 NG airplane are presented in report [32]. Methodology of the calculation is described for example in [19]. In the thesis, only a brief description is presented.

Several types of loading spectra can be defined:

- gusts spectra
- manoeuvres spectra
- landing impact
- taxi spectra
- ground-air-ground (G-A-G) cycle

Typically, loads from the first four types of spectra are superimposed into the G-A-G cycle. Typical flight profile of L 410 NG with is described in report [36]. It is depicted in Figure 6.8 together with the description of basic flight phases.
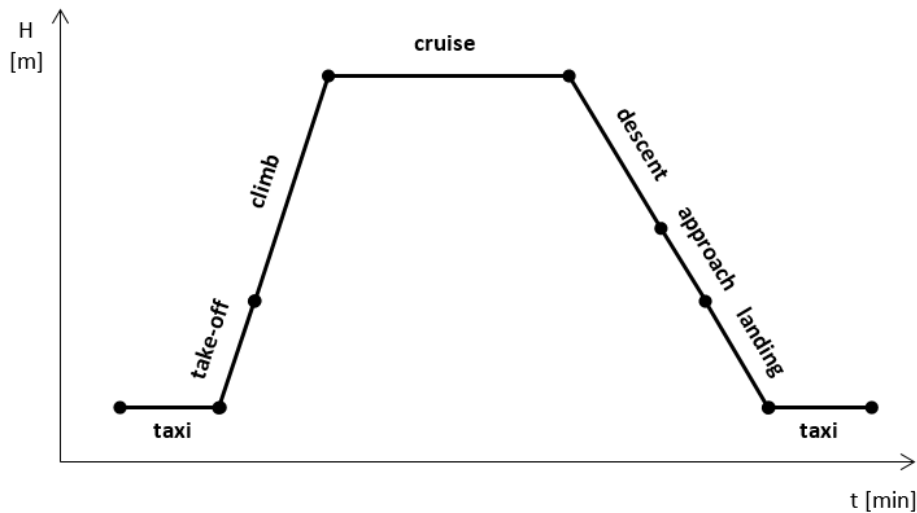
Figure 6.8 Typical flight profile; lengths of flight phases scaled

To calculate fatigue life of the aircraft structure, damage contributed by each type of spectrum has to be evaluated. Because during the taxi the fatigue critical part of the wing (bottom side) is in compression and thus not contributing to the fatigue damage accumulation, this spectrum is not included in the calculation. The fatigue life can be calculated as follows:

$$N = \frac{t_{FD}}{D_{gust} + D_{man} + D_{lndg} + D_{GAG}}$$

(6.8)

where D is damage caused by gust or manoeuvre spectrum, landing impact and G-A-G cycle during one flight and t_{FD} is a flight duration in [FH].

To obtain damage caused by each type of spectrum during every flight phase it is necessary to know magnitudes of the loads and their frequencies. Because any load magnitudes are hardly the

same, the frequencies of the loads are defined for some ranges, so called probability classes. Every class is defined by a mean load (gust speed, load factor etc.) and cumulative frequency. Generally, the most severe conditions are present only occasionally, while loads with only small amplitude are represented in ample amount, as it is illustrated in Figure 6.9.
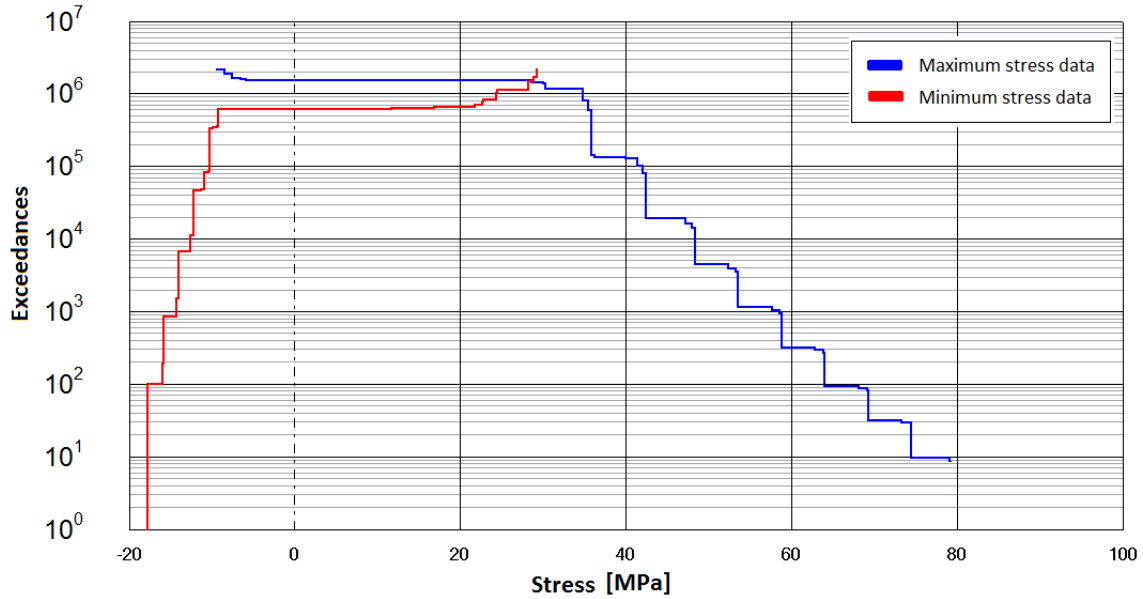

Figure 6.9 Exceedance plot of a loading sequence; Bottom panel L 410 NG

The following procedure applies for fatigue life calculation:

1. Determine the stress level based on the bending moment for each probability class and flight stage:

$$\sigma_{max,min} = M_{max,min}\, f \qquad (6.9)$$

where *f* is a stress increment per bending moment in cruise in [MPa/Nm].

2. Mean stress and amplitude are derived from the maximum and minimum value according to equation (6.4).
3. Oding correction, see eq. (6.5), is applied to define σ_{puls}
4. The fatigue life is calculated from the S-N curve, equation (6.2)
5. A partial damage $D_{i,j}$ is derived for given spectrum, class and flight stage:

$$D_{i,j} = \frac{n_{i,j}}{N_{i,j}} \qquad (6.10)$$

where n is a cumulative frequency of the load and *N* is a number of cycles to fatigue failure for given stress level.

6. Palmgren-Miner rule is applied to obtain the damage by a given spectrum:

$$D = \sum_{i=1}^{k}\sum_{j=1}^{l} D_{i,j} \qquad (6.11)$$

where *i* is an index of the flight stage (1 = take-off, 2 = climb, 3 = cruise, 4 = descent, 5 = approach and 6 = landing), *j* is an index of a probability class, *k* is a number of stages (for landing impact and G-A-G cycle k = 1) and l is number of classes.

7. Number of cycles to fatigue failure is calculated with use of equation (6.8).

6.4 Damage accumulation during crack growth period

The fatigue calculation gave us periods until a crack 1 mm long is reached for every fastener at its both sides in direction of potential crack growth, i.e. perpendicular to the major principal stress. Based on these values, the damage at the moment of initiation of the first crack may be calculated. The relation (2.1) in chapter 2.4.1 is used for calculation of the initial damage. During the crack growth phase, other holes still need to accumulate more damage until a crack appears. The rate of damage is described by the equation (6.12) [10]. N_{init} represents a number of cycles to the first crack initiation and $N_{a=1mm}$ is a number of cycles required to crack initiation for each fastener independently. Remaining parameters are about to be described later on.

$$D = D_{init} + \sum_{i=N_{init}}^{N_{a=1mm}} \frac{1}{N_{a=1mm}} \left(k_{net}\, k_{cr,opp}\, k_{cr,vic} \right)^m \qquad (6.12)$$

This relation is based on the Palmgren-Miner's rule (see chapter 6.3.2) with taking into account the fact that the crack presence speeds up the damage accumulation. Schmidt suggests considering three influences [10]:

- net section loss (k_{net})
- damage increase at an uncracked side of a cracked hole ($k_{cr,opp}$)
- vicinity of a crack ($k_{cr,vic}$)

It is appropriate to point out that the damage accumulation influences are powered by an S-N curve exponent m. This power originates in a relation between the stress and cycle count, as shown in an S-N curve definition, see equation (6.2).

6.4.1 Damage accumulation due to net section loss

Cracks existing in the structure increase the net-section stress, since the load is transferred by the smaller section area. Coefficient k_{net} taking this effect into account is calculated as follows:

$$k_{net} = \frac{W}{W - \sum a} \qquad (6.13)$$

where W is a specimen width and $\sum a$ is total length of cracks.

6.4.2 Damage accumulation at an uncracked side of a cracked hole

Another effect having a significant influence on the damage accumulation is a crack presence on the uncracked side of the hole. According to [14], two holes connected by a slit can be substituted by an elliptic hole, with error below 2 %. This principle applies on a hole with a crack as well. Provided the crack reaches the edge, a substitution by a U-notch or an elliptic notch is appropriate. The approach is depicted in Figure 6.10. The influence of the crack at a remote side of a hole is described by one of equations (6.14), depending on whether the crack reached the edge or not.

$$k_{cr,opp} = \frac{K_{t_{ellipse}}}{K_{t_{circle}}} \qquad\qquad k_{cr,opp} = \frac{K_{t_{U-notch}}}{K_{t_{circle}}} \qquad (6.14)$$

where K_t are stress concentration factors for a circle, and the ellipse or the U-notch obtained by the substitution. They are calculated with use of equations (5.13) to (5.15).
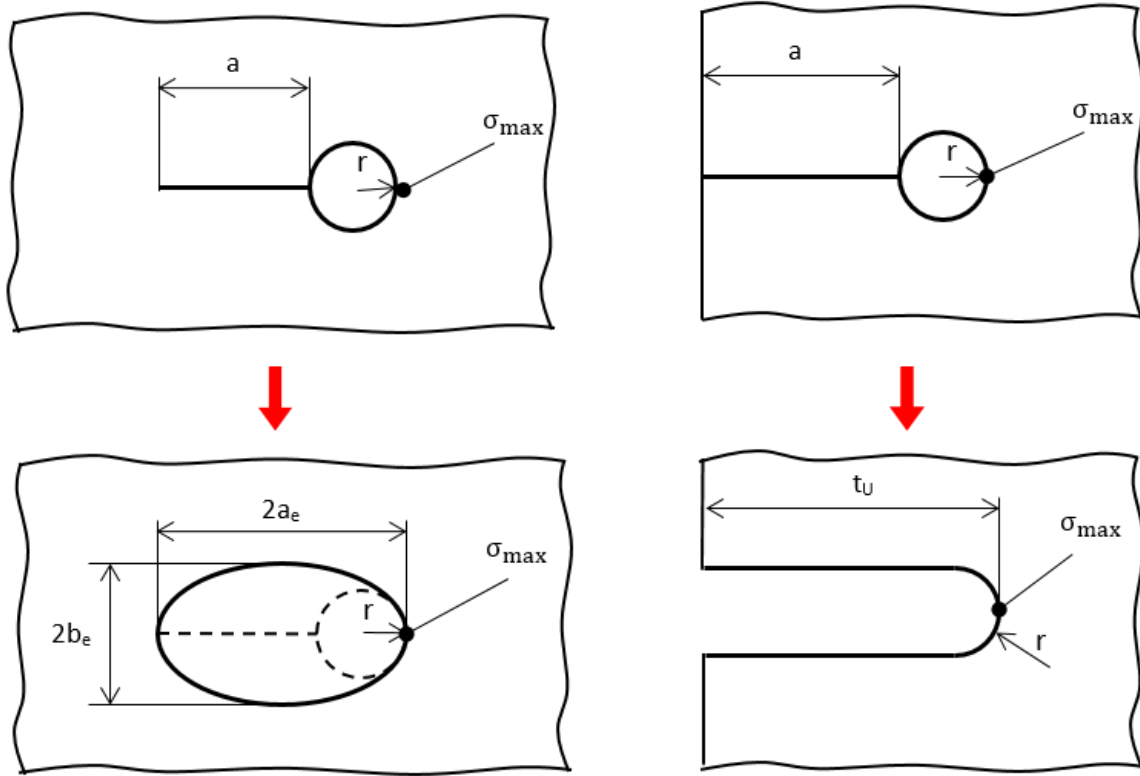
Figure 6.10 Substitution of a circular hole with a crack by an elliptic hole or a U-notch [14]

6.4.3   Damage accumulation at a hole in vicinity of a crack

When a crack is approaching a hole the stress at the place of interest in Figure 6.11 increases. Because the stress concentration factor (SCF) values for a hole in vicinity of a crack were not provided in available literature, they were calculated with help of AFGROW. According to Rooke and Tweed [5], stress intensity factor (SIF) K at a cracked hole for zero crack length is related to SCF at an elliptic hole according to equation (6.15). This applies for circular hole too, as a circle is a special case of an ellipse.

$$\lim_{a \to 0} \frac{K_I}{\sigma\sqrt{\pi a}} = 1.1215\, K_t \qquad (6.15)$$
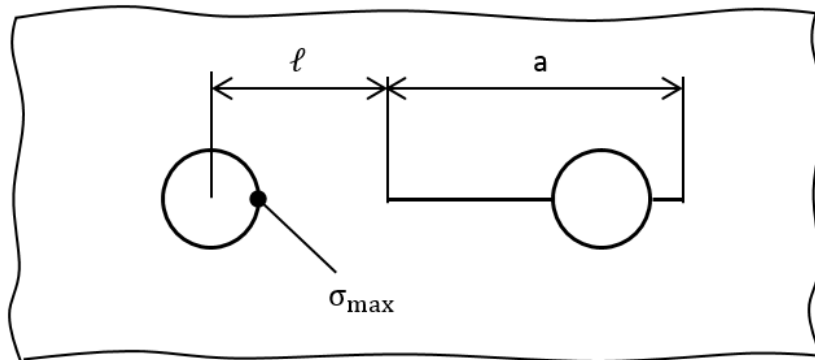

Figure 6.11 Crack approaching an uncracked hole

38

Following procedure exploiting the equation (6.15) to obtain SCF is performed:

1. Stress intensity factor at the crack tip A as depicted in Figure 6.12 is calculated for various a/ℓ ratios. Models with combinations of lengths a = [1, 5, 10, 20, 50, 100, 200, 500] and ℓ = [2, 4, 10, 20, 50], were used.
2. Equation (6.15) is used to determine stress concentration factor K_t.
3. Obtained SCF is normalized to SCF at a circular hole in an infinite plate, i.e. to $K_{t,circle}$ = 3.
4. Regression is performed to obtain relation between SCF and a/ℓ.

Dimensions in the model were chosen with respect to geometrical boundaries so they do not influence the results, thus W = 2000 mm. The leading crack length is assumed extremely small (1 μm), so it approximates a zero crack length well. Diameter of the hole was set to 2 mm. However, because it does not have influence on the SCF value (for infinite plate case), it does not play a role.

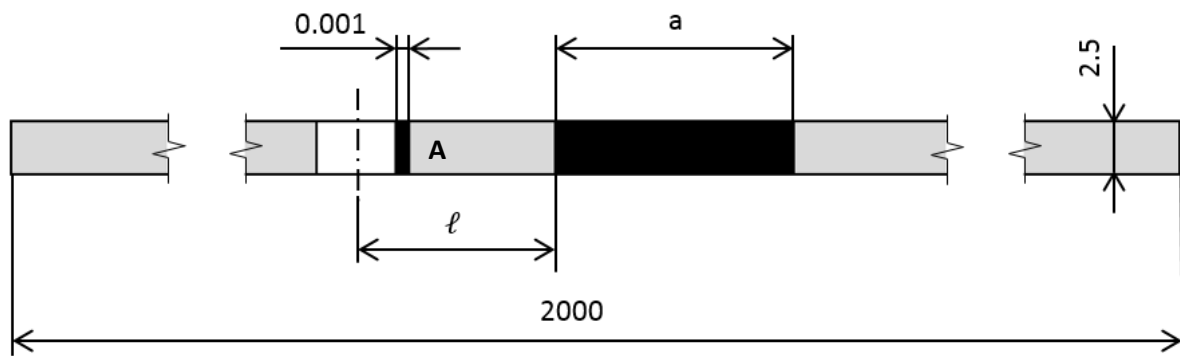Values of calculated normalized values of stress concentration factor $k_{cr,vic}$ are presented in Table 6.1.

Figure 6.12 Dimensions of AFGROW model for stress concentration factor calculation in [mm]

Table 6.1 Values of normalized stress concentration factor for various crack lengths and distances

		ℓ [mm]				
		2	**4**	**10**	**20**	**50**
a [mm]	**1**	1.0490	1.0106	1.0020	1.0000	1.0000
	5	1.3693	1.1245	1.0284	1.0111	1.0014
	10	1.7351	1.2719	1.0719	1.0306	1.0082
	20	2.2718	1.5619	1.1913	1.0759	1.0271
	50	3.2391	2.3893	1.5214	1.2420	1.0764
	100	3.5024	2.9760	1.9917	1.4859	1.1667
	200	3.6457	3.3589	2.6337	1.9366	1.3772
	500	4.1049	3.9742	3.5943	3.0075	2.0078

Finally, values presented in Table 6.1 are processed to obtain a rate of influence of the crack on the SCF, see Figure 6.13. The threshold value for change of approximating functions is determined by a maximum of the parabola approximating the lower region.

$$k_{cr,vic} = \begin{cases} -0.011(a/\ell)^2 + 0.1069(a/\ell) + 1 & \text{if } (a/\ell) \leq 48 \\ 2.6064(a/\ell)^{0.084} & \text{if } (a/\ell) > 48 \end{cases} \qquad (6.16)$$
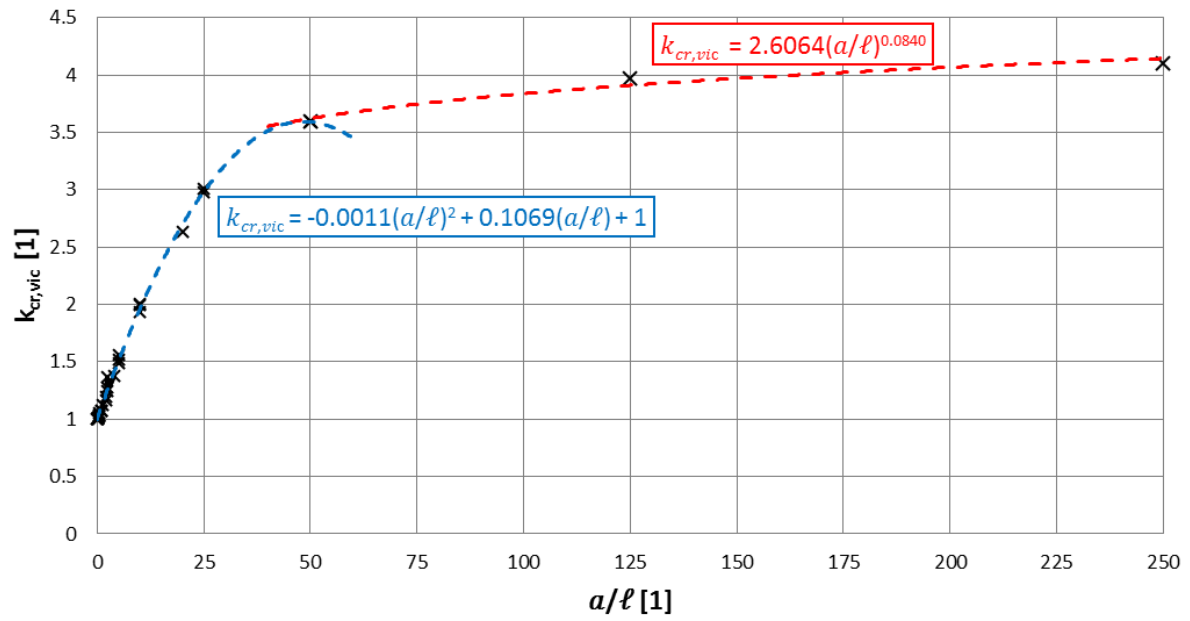
Figure 6.13 Relation between normalized stress concentration factor of a hole near a crack and ratio between crack length and crack-to-hole distance

7   Crack growth

7.1   Introduction

In previous chapter the methods of estimating the crack initiation period were introduced. Once a crack reaches macroscopic dimensions, its growth rate depends on the crack growth resistance of the material as a bulk property. It was observed from tests on central crack tension (CCT) specimens, also known as middle tension (M(T)) specimens, that crack growth rate da/dN for given stress ratio R depends on the stress amplitude, as depicted in Figure 7.1. Because stress in the area near the crack tip is dominated by a stress intensity factor (SIF), described in detail in chapter 8, trying to find a relation between the crack growth rate and the SIF amplitude suggests. The result of such an approach is displayed in Figure 7.2.
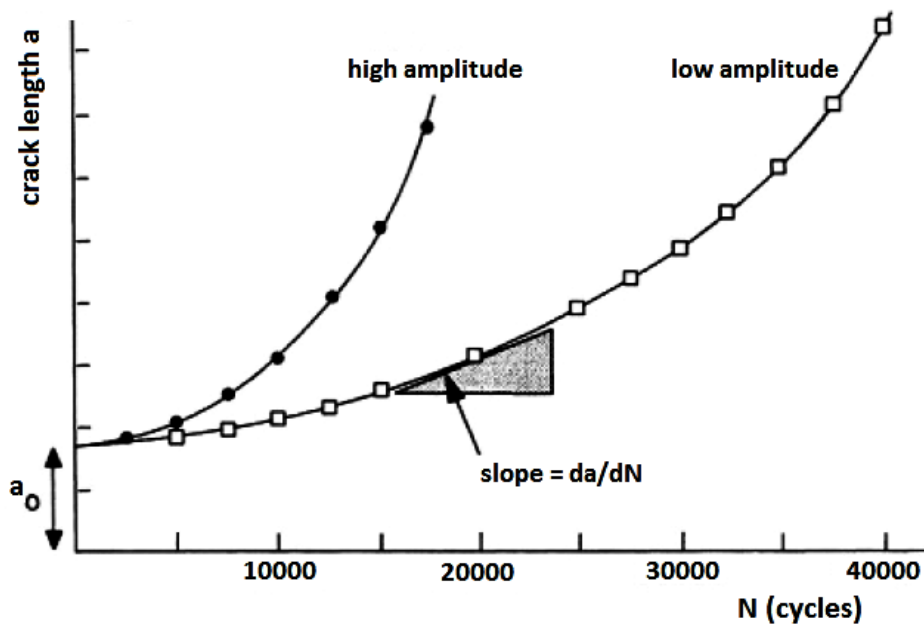

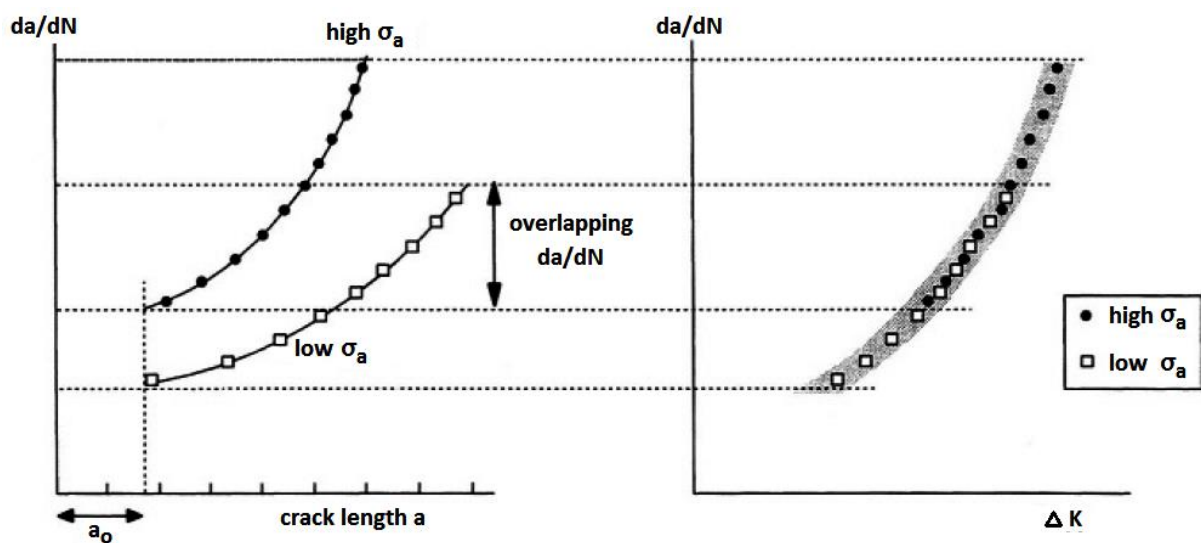Figure 7.1 Crack growth curve under various stress amplitudes (same stress ratio R) [16]

Figure 7.2 Derivation of crack growth rate – SIF amplitude curve [16]

41

7.2 Crack growth regions

Depending on the ΔK magnitude, several regions of a crack growth might be defined, as depicted in Figure 7.3. It was observed that when decreasing the SIF amplitude at the macro-crack tip, we arrive in the region where crack growth significantly slows down and sequentially stops. The value of the SIF amplitude below which the crack no longer grows is referred as a threshold SIF (ΔK_{th}). Crack is generally assumed not growing if the crack growth rate drops below 10^{-10} m/cycle. Recommended procedures for determining the value are presented in ASTM Standard E647 [35].

For higher SIF amplitudes, in so called Paris region, the crack growth rate can be described by a power function, as proposed by Paris [16]:

$$\frac{da}{dN} = C_p \, (\Delta K)^{n_f} \tag{7.1}$$

where C and n_f are material constants.

Nevertheless, this relation does not account for R-effect or asymptotic behaviour in the regions I and III. For that reason, Forman suggested an equation considering an influence of the stress ratio and accelerated crack growth in the third region.

$$\frac{da}{dN} = C_f \frac{(\Delta K)^{n_f}}{(1-R)K_C - \Delta K} = C_f \frac{(\Delta K)^{n_f}}{(1-R)(K_C - K_{max})} \tag{7.2}$$

Apparently, when K approaches the plane stress fracture toughness value for given stress ratio R, the crack growth rate goes to infinity, denoting the fracture. However, the equation still does not consider the threshold region; it only extrapolates the crack growth rate from the Paris region, leading to faster crack growth for low SIF amplitudes than in reality. Because of this, Forman equation offers a conservative approach which is desirable for variable amplitude crack growth predictions.
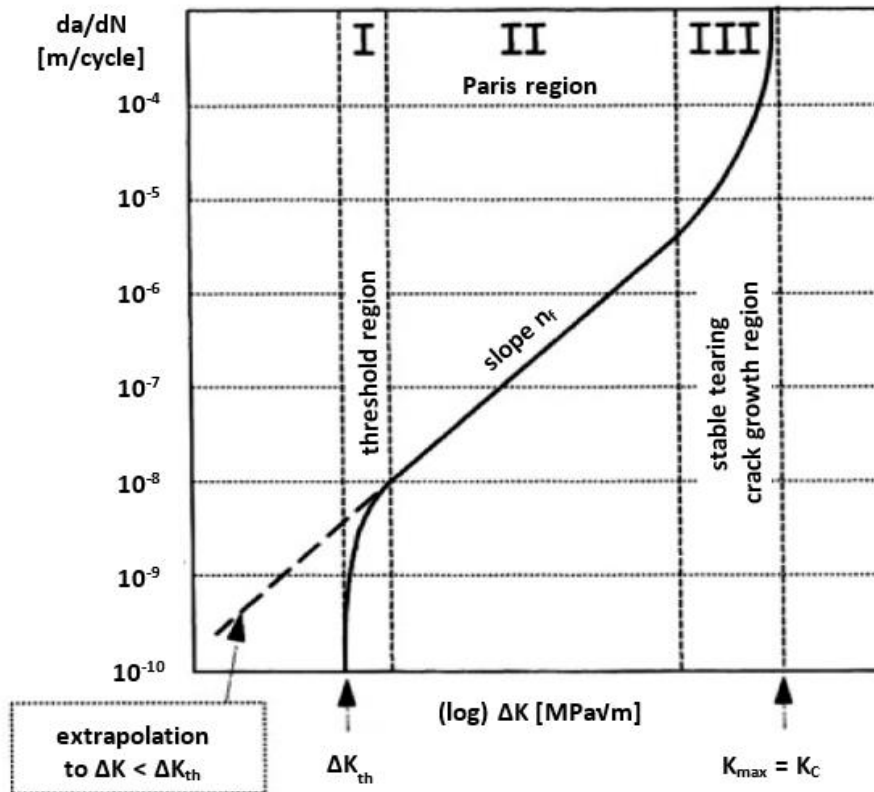

Figure 7.3 Crack growth regions [16]

In order to satisfy both asymptotic regions, equations by Priddle, equation (7.3), or by Klesnil and Lukáš, eq. (7.4), are suggested.

$$\frac{da}{dN} = C_f \frac{(\Delta K - \Delta K_{th})^{n_f}}{(1 - R)K_C - \Delta K}$$

(7.3)

$$\frac{da}{dN} = A(1 - R)^\gamma$$

(7.4)

where A and γ are material constants.

The crack growth rate in the region of stable tearing crack growth is relatively high, in order of 0.01 mm/cycle and above. Local areas of ductile tearing are observed. Despite that the crack growth appears to be stable, only a short life is expected until a fracture occurs.

7.3 Crack closure

Until now, it was assumed that displacements during the crack unloading return to zero when SIF is zero. However, it was observed that as a result of plastic deformation at the crack tip, the crack is already closed at positive SIF value. This leads to decrease of effective stress intensity factor used for crack growth prediction.

This phenomenon has a great impact on the growth rate of cracks loaded by randomized sequence. Provided a cycle with significantly higher amplitude (overload cycle) preceded, a large plastic zone PZ is created when unloading the crack. This leads to decrease of effective SIF of following cycles, until the crack gets out of the area dominated by the plastic zone PZ. This effect, resulting in slower crack growth, is called crack growth retardation and can be simulated by several models:

- yield zone models (Wheeler, Willenborg, etc.)
- crack closure models (PREFFAS, CORPUS, Hsu, etc.)
- strip yield models (FASTRAN, STRIPY, etc.)

The complexity and accuracy of the models is different, although still increasing the complexity of the calculation. Because the computational time is precious during the MC simulation and linear model excluding the cycle interaction effects gives conservative results, the retardation is not included in the AIMA algorithm. Therefore, no more focus on the topic is made, for an insight reference [16] is recommended.

7.4 Sequence processing

When performing a crack growth prediction or fatigue analysis, we manipulate with cycles. However, when having a sequence of cycles at disposal, it is important to process the data in order to obtain separate cycles which would serve as an input for the analysis. Several counting methods were developed. Single counting methods define the cycle based on one parameter, usually location of an extreme, level crossing or amplitude. Such methods are for example:

- peak counting
- level crossing counting

More advanced methods utilise two parameters to define a cycle, usually location of both extremes. These methods include:

- range counting
- range pair counting
- racetrack counting
- rain flow counting

In AI, the range pair counting method is used for processing a loading sequence. A decomposition of a segment of the sequence is displayed in Figure 7.4. The cycle is counted if following conditions are satisfied (different for segments with increasing and decreasing load).

Increasing load: $X_{p-2} > X_{p-3}$ & $X_{p-1} \geq X_{p-3}$ & $X_p \geq X_{p-2}$ *(7.5)*

Decreasing load: $X_{p-2} < X_{p-3}$ & $X_{p-1} \leq X_{p-3}$ & $X_p \leq X_{p-2}$ *(7.6)*
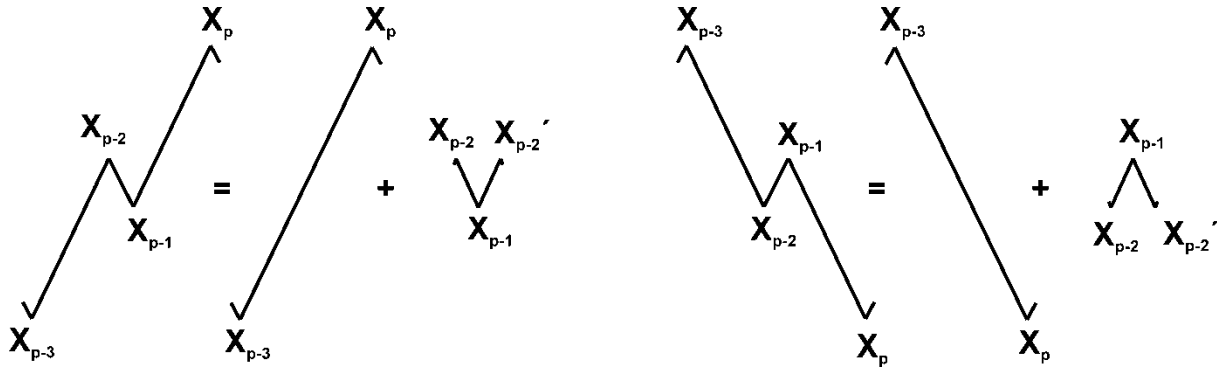

Figure 7.4 Range pair counting method definition [19]

7.5   Link-up of cracks

When performing an MSD analysis, defining the moment when opposing cracks connect is important. Residual strength of the remaining segment needs to be determined. Swift in [9] presents an analysis of failure modes of unstiffened centre cracked panels of various widths. He concluded that for panels wider than 1270 mm the failure due to high SIF occurs; otherwise net section yielding is a dominant failure mode. The relation is illustrated in Figure 7.5. In terms of the MSD analysis, the effective width of the panel *W* is restricted by the holes presence. With respect to the spacing of the holes the effective width is defined as the width B_f from Figure 5.4. Because practically the rivet spacing in any structure does not even get close to the value 1270 mm, we can conclude that the net-section yielding will be virtually always the criterion of the ligament failure in MSD analyses.
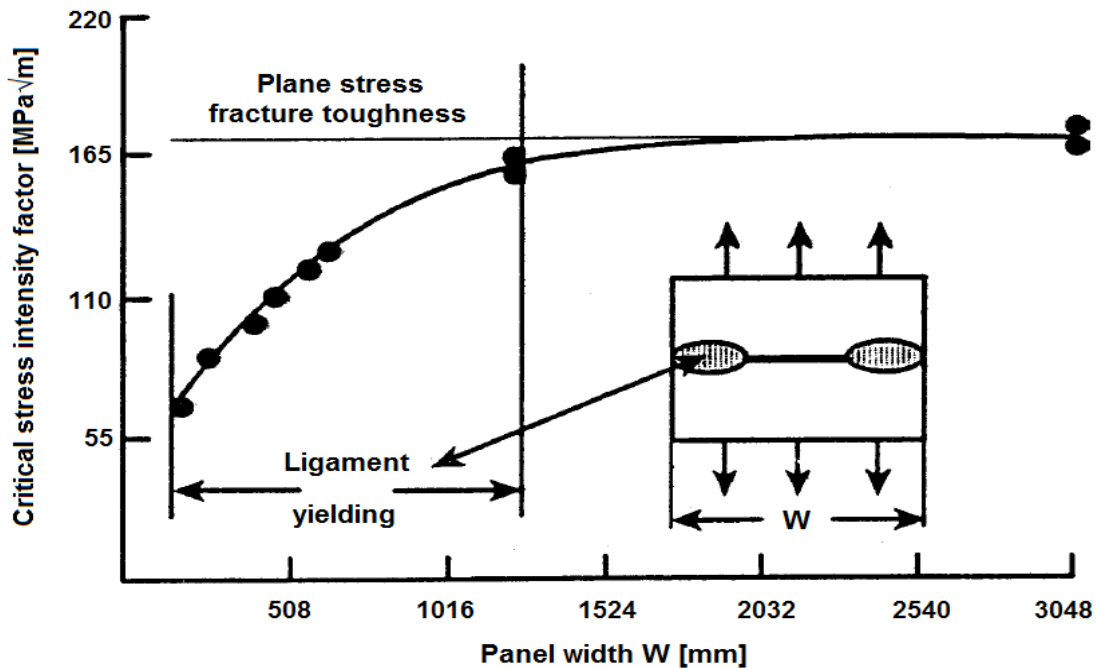

Figure 7.5 Relation between panel width and failure mode [9];
conversion from imperial to metric units performed

The crack link-up may be based on direct comparison of the net section force in the remaining ligament to the yield strength, as proposed by Schmidt [10], see Figure 7.6a.

Another approach by Swift [9] suggests defining the link-up by touching the plastic zones of two near crack tips, i.e. their summed length reaches ligament length, see Figure 7.6b. After condition (7.7) is met, failure of the ligament occurs and cracks unite in one larger crack.

$$r_{p_1} + r_{p_2} = B - (r_1 + r_2) - (a_1 + a_2) \qquad (7.7)$$

where B is distance between centres of holes, a is crack length and r is radius of holes.

Deviations between the models are small, since both of them are based on net section yielding. Moreover, with decreasing ligament length, stress intensity factor at the crack tip grows significantly (see chapter 8.6.2) leading to the fast crack growth. Therefore, possible deviations would be in order of several cycles.
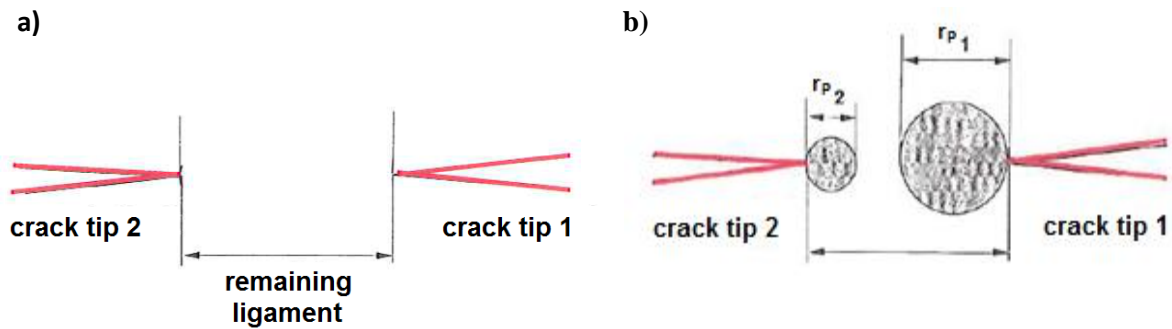
Figure 7.6 Principle of link-up criteria [10];
a) net section criterion, b) Swift's criterion of touching plastic zones

After connecting cracks, it is necessary to redefine geometry of the model for further SIF calculations. According to Harter [11], when calculating the SIF at crack tips A and B, as marked in Figure 7.7, substituting holes by a crack is suitable. This method gives an error below 1 % for any reasonable geometry (analysis was performed for spacing B ≥ 2d).

Figure 7.7 Substitution for modelling linked-up cracks. Based on [11]

8 Stress intensity factor

8.1 Introduction

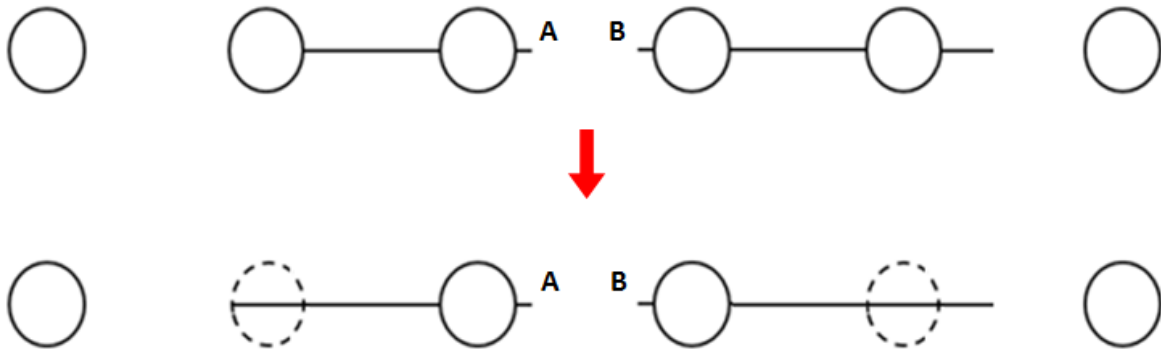Stress concentration factor as a mean of considering stress distribution change around notches was discussed in chapter 5.3. A crack can be modelled as an elliptic hole with zero height, thus there exists a solution for stress value near a crack tip in an infinite plate. However, since a crack is a notch with a zero tip radius, value of K_t would be infinite for any crack length, hence this approach is no longer applicable for description of stress state. A new concept using stress intensity factor (SIF) was introduced by Irwin [16]. Its application to predict crack growth is referred as linear elastic fracture mechanics (LEFM). Stress intensity factor can be calculated using formula (7.2).

$$K = \beta\sigma\sqrt{\pi a} \qquad (8.1)$$

where σ is applied remote stress, a is crack length and β is a factor depending on geometry of the component or specimen and the type of loading, so called shape function.

There are three basic modes of crack opening, as depicted in Figure 8.1. As experience shows, fatigue cracks usually grow in direction perpendicular to the major principal stress, i.e. they tend to grow under the mode I. Even if a crack initiates under pure shear loading, a rapid transition into the crack growth in the mode I occurs. In structures with dominant tensile loading, the crack growth direction is perpendicular to the remote stress.

Mode I
Opening in tension

Mode II
In-plane shear

Mode III
Transverse shear
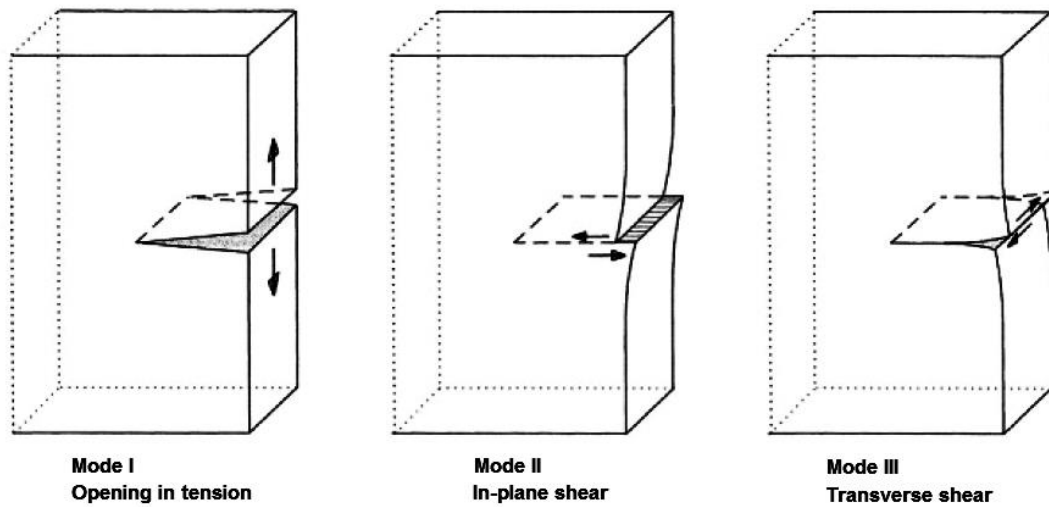
Figure 8.1 Crack opening modes [16]

8.2 Crack tip plasticity

Stress state near the crack tip may be described by eq. (8.2) [16], where $\sigma_{i,j}$ are stresses from Cauchy stress tensor and $f_{i,j}(\theta)$ are functions (8.3) depending on the position to the crack tip. Coordinates are defined in Figure 8.2. This equation is valid for r = 0, however for r reasonably small compared to crack length it still provides a good approximation.

$$\sigma_{i,j} = \frac{K}{\sqrt{2\pi r}}f_{i,j}(\theta) \qquad (8.2)$$

$$f_{ij} = \begin{bmatrix} \cos\frac{\theta}{2}\left(1 - \sin\frac{\theta}{2}\sin\frac{3\theta}{2}\right) & \cos\frac{\theta}{2}\sin\frac{\theta}{2}\sin\frac{3\theta}{2} & 0 \\ \cos\frac{\theta}{2}\sin\frac{\theta}{2}\sin\frac{3\theta}{2} & \cos\frac{\theta}{2}\left(1 + \sin\frac{\theta}{2}\sin\frac{3\theta}{2}\right) & 0 \\ 0 & 0 & f_{zz} \end{bmatrix} \tag{8.3}$$

where f_{zz} depends on the state of stress; v is Poisson's ratio.

$$f_{zz} = \begin{cases} 0 & \text{for plane stress} \\ 2v\cos\frac{\theta}{2} & \text{for plane strain} \end{cases}$$
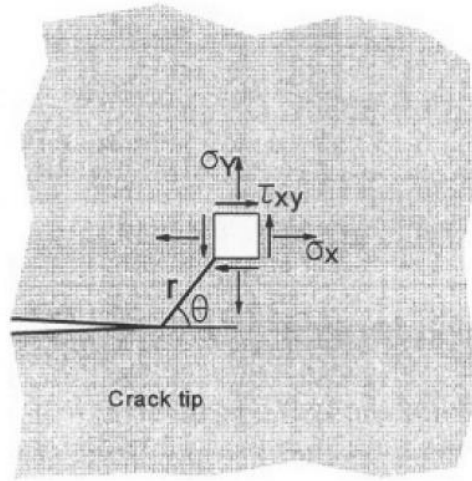

Figure 8.2 Definition of coordinates [16]

Apparently, as r → 0, stress goes to infinity. Of course this is not possible and a small plastic zone is created near the crack tip as a consequence, see Figure 8.4. Let r_e be a maximum value of r where equation (8.2) is still applicable, defining thus so called K-dominated zone; and r_p – a size of the plastic zone. Then we can expect that if the plastic zone is significantly smaller than r_e-zone, the stress redistribution on periphery of the K-dominated zone will be negligible. According to [6] and [16] the conditions on applicability of SIF approach (8.4) apply. The condition (8.5) suggested by ASTM [25] is slightly less strict than (8.4).

$$a > 10\, r_e \qquad\qquad\qquad\qquad r_e > r_p \tag{8.4}$$

$$a > 2.5\left(\frac{K}{R_{p0.2}}\right)^2 \tag{8.5}$$

Before we proceed to estimating the plastic zone size, a description of its shape under different stress state takes place. An uncracked metal plate loaded in uniaxial tension is in a plane stress state. When a crack is present, areas remote from the crack tip are still unaffected, while a highly stressed area near the crack tip is prevented from contracting in through-the-thickness direction, i.e. it is in a state of plane strain. However, when the plastic zone is of size comparable to the specimen thickness, through-the-thickness stress cannot be fully developed, meaning that the crack tip area is in a state of the plane stress. Description of stress states in a thick and a thin plate is displayed in Figure 8.3. Conditions (8.6) apply on the specimen thickness.

Plane stress: $\qquad t \ll 2.5\left(\frac{K}{R_{p0.2}}\right)^2 \qquad$ Plane strain: $\qquad t \geq 2.5\left(\frac{K}{R_{p0.2}}\right)^2 \tag{8.6}$
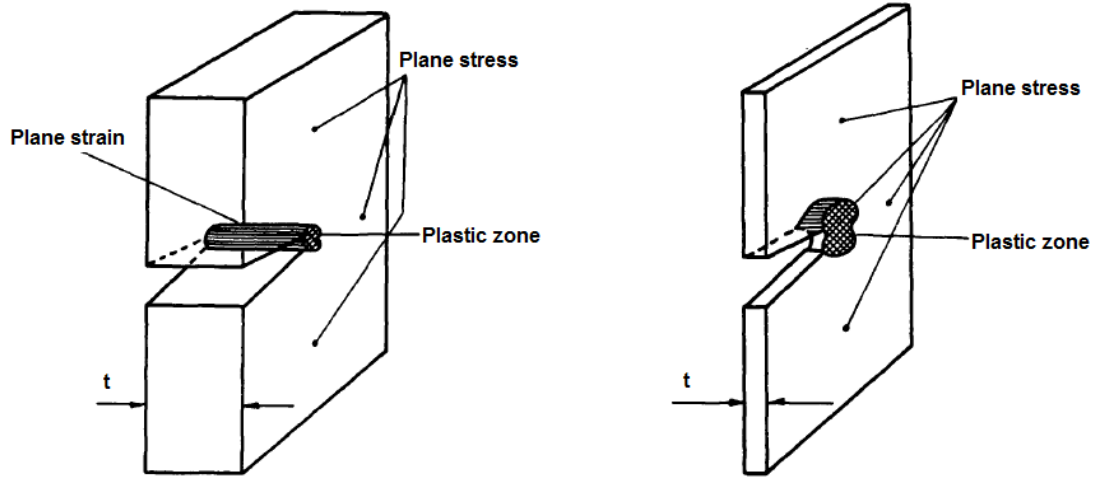
Figure 8.3 Stress state at the crack tip depending on the specimen thickness [29]

To estimate size of the plastic zone for a plane stress situation, equation (8.2) is used. Stress in direction of loading σ_y is distributed along x axis (i.e. θ = 0°) as follows:

$$\sigma_y = \frac{K}{\sqrt{2\pi r}}$$

(8.7)

This serves as a basis for evaluation of r_p, provided σ_y = $R_{p0.2}$:

$$r_p = \frac{1}{2\pi}\left(\frac{K}{R_{p0.2}}\right)^2$$

(8.8)

However, this relation does not take into account redistribution of stress over yield strength (hatched area in Figure 8.4). Hence Schijve [16] estimates its size to be twice as big as the equation (8.8) suggests, see eq. (8.9).
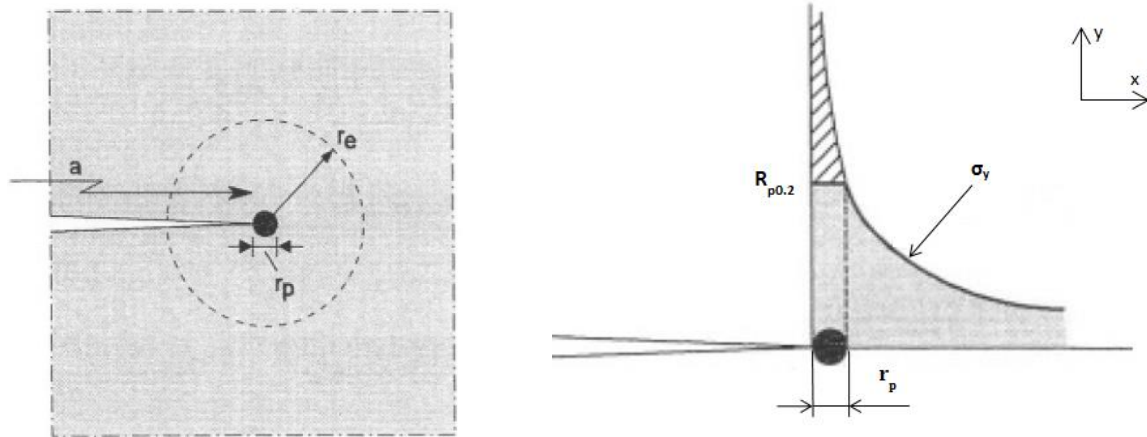
Figure 8.4 K-dominated zone around plastic zone at crack tip [16]

For plane strain, estimate might be made by utilising a yield criterion such as Von Mises. Since lateral contraction is constrained for a plain strain, effective yield strength is higher, leading to eq. (8.10). The AIMA algorithm assumes the plane stress as it gives larger plastic zones, thus being conservative even if the plane strain state was prevailing.

Plane stress:
$$r_p = \frac{1}{\pi}\left(\frac{K}{R_{p0.2}}\right)^2$$

(8.9)

Plane strain:
$$r_p = \frac{1}{3\pi}\left(\frac{K}{R_{p0.2}}\right)^2$$
(8.10)

8.3 Linear elastic fracture mechanics applicability

As it was stated before, applicability of LEFM is limited by size of plastic zone. In case the conditions (8.4) were not met, more complex theory of elastic-plastic fracture mechanics (EPFM) would need to be employed. After putting equation (8.1) into equation (8.5) and rearranging, we obtain condition on maximum stress when LEFM is valid:

$$\beta\,\sigma < 0.3568\,R_{p0.2}$$
(8.11)

Assuming a single crack at a hole (initiated with length 1 mm) in a large plate, β varies between 1.504 for d = 3 mm and 2.506 for d = 6 mm. Then we get maximum allowable stress to meet condition (8.5) as σ = 0.237 $R_{p0.2}$ for d = 3 mm and σ = 0.142 $R_{p0.2}$ for d = 6 mm. For the larger hole maximum allowed stress is then around 60 MPa for aluminium (7475-T7351 alloy [38]). This value is relatively high in terms of fatigue or MSD analysis. It is felicitous to note that the condition (8.11) is derived for the plane stress; for the plane strain the allowed stress level would be higher.

Moreover, since a crack growth stage holds a short time compared to fatigue crack initiation in a structure's life, an error caused by employing the LEFM outside of a region of its validity is not expected to be significant. On top of that, according to [26], it gives conservative results compared to the EPFM.

As illustrated in an example in Figure 8.5, the initiation takes more than 80 % of fatigue life of the specimen showed in Figure 10.6 for any stress level. The linear elastic fracture mechanics was employed. Irregularity of the initiation time between stress levels is a result of randomizing the initial state, because only one run of Monte Carlo simulation was performed.
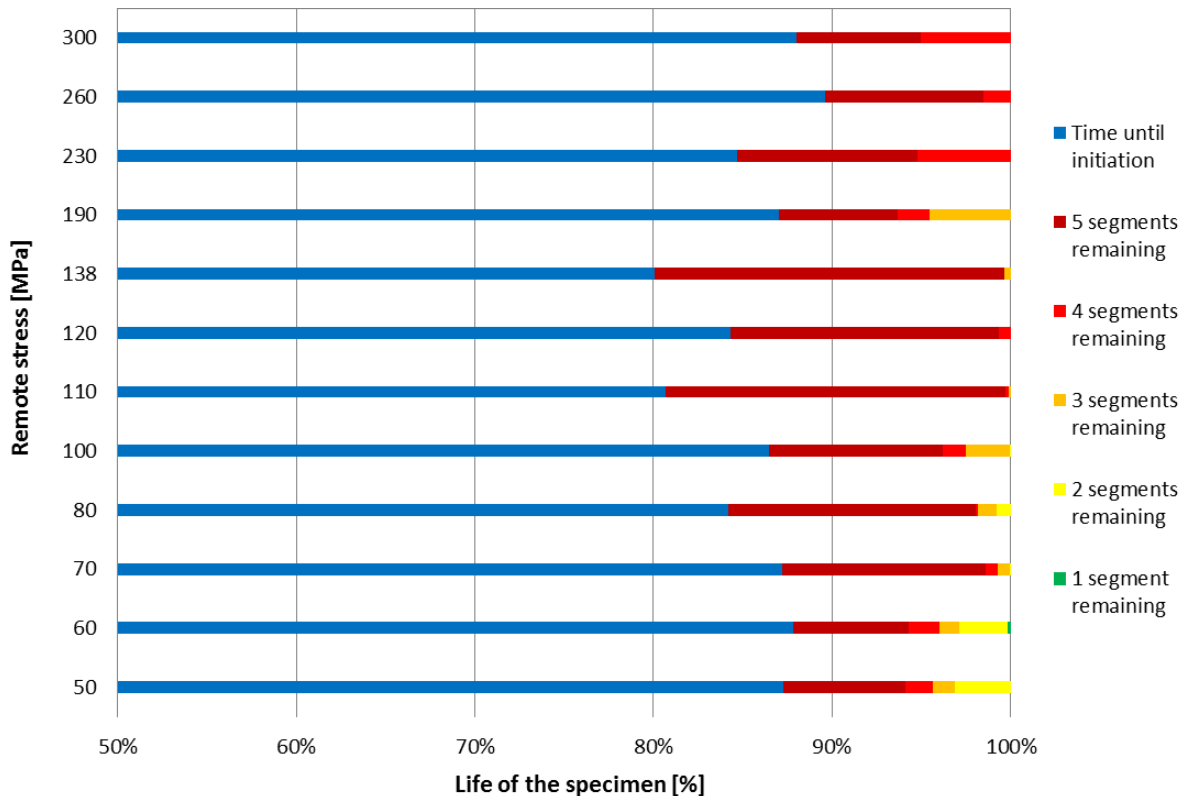

Figure 8.5 Remaining number of segments of the test specimen during its life for various stress levels. Initial damage (hence position of initial crack as well) randomized.

49

8.4   Stress intensity factor compounding method

Solutions to β function are generally at disposal for simple configurations. To evaluate complex geometries, Bombardier et al. [21] suggest compounding the final β function of known solutions.

1. β for a single crack
    1.1. Crack in infinite plate
    1.2. Finite width correction
    1.3. Offset correction
2. Crack interaction

Then final stress intensity factor is obtained as a product of all above mentioned values. Example of applying this method is provided by Kathiresan et al. [23]. A solution for an offset single crack at a hole in finite plane is desired. It can be composed of solutions for single crack at a hole in infinite plate and centre crack offset from the edge and centre crack in infinite plate, see equation (8.12). Graphical demonstration is shown in Figure 8.6.

$$\beta_{single,offset} = \beta_{single,infinite} \frac{\beta_{centre,offset}}{\beta_{centre,infinite}} \qquad (8.12)$$
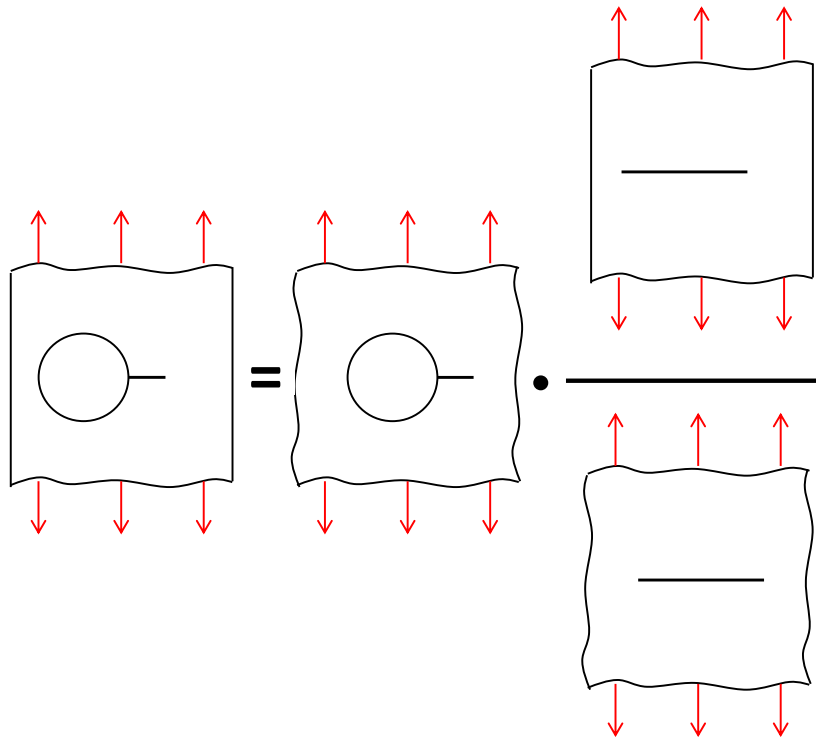

Figure 8.6   Example of compounding method (based on [23]):
Desired geometry = Single crack at hole in infinite plane * Offset centre crack / Centre crack in infinite plane

8.5   Stress intensity factor for a single crack

Because Schmidt in [10] suggests using through the thickness cracks 1 mm long as initial cracks for MSD analyses, all possible crack geometries are covered by five closed-form solutions. An option of a panel with stringers was not implemented to simplify the computation. Because the stringers actually slow down the crack growth, this assumption does not even put us in danger of over-estimating a WFD free period. Following solutions are employed:

  – Single crack at a hole
  – Edge crack
  – Centre through crack
  – Two cracks at a hole of equal length (referred as double symmetrical crack as well)
  – Two cracks at a hole of unequal length (referred as double asymmetrical crack as well)

Moreover, since the approach of using maximum stress (superposition of axial and bending stress) augmented by pin load effects according equation (5.2) with assumption of loading just in column-wise direction (see Figure 5.4) is used, only one load type is considered: axial loading. This allows increasing time effectiveness of the calculation, while staying conservative.
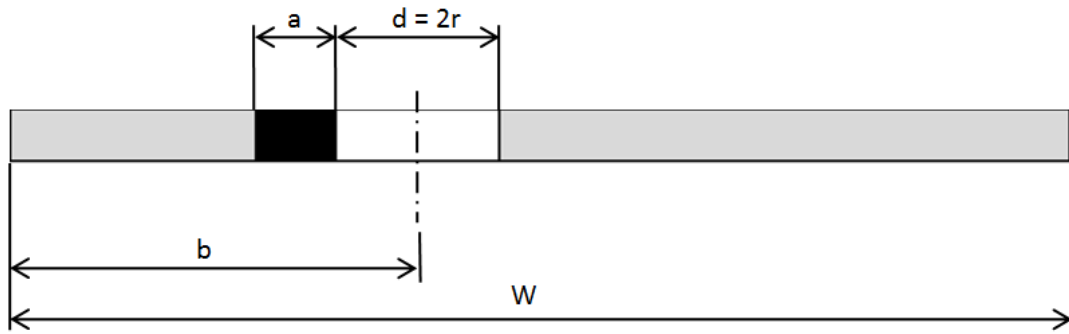
8.5.1   Single crack at a hole

Figure 8.7 Geometry of specimen with a single crack at a hole

Shape function β for given geometry consists of infinite plane solution β_∞, two finite width corrections F_w and F_{ww}, and offset correction F_{off}. Solution presented below was acquired from [1].

$$\beta = \beta_\infty F_w F_{ww} F_{off} \tag{8.13}$$

Infinite plane solution:

$$\beta_\infty = 0.9196 \left(\frac{r}{r+a}\right)^4 + 0.642 \left(\frac{r}{r+a}\right)^3 + 0.3415 \left(\frac{r}{r+a}\right)^2 + 0.7548 \left(\frac{r}{r+a}\right) + 0.7071 \tag{8.14}$$

Finite width corrections:

$$F_w = \sqrt{\sec\left(\frac{\pi r}{W}\right) \sec\left(\frac{\pi(r+a/2)}{W-a}\right)} \tag{8.15}$$

$$F_{ww} = 1 - \left(\min\left\{2.275;\ \left(2.65 - 0.24\left(2.75 - \frac{W}{d}\right)^2\right)\right\}^{\frac{-W}{d}}\right)\left(\frac{2a}{W-d}\right)^{\frac{W}{d}+0.5} \tag{8.16}$$

The solution is valid if:

$$a/r > 0 \qquad\qquad \frac{r + a/2}{W - a} < 0.5 \qquad\qquad (8.17)$$

The first condition (8.17) is fulfilled in all cases, since crack length and radius are positive values. The other condition (8.17) is met always if $r < W/12$, because if $a/r > 5$ the model for centre crack is used. If $r \geq W/12$, not satisfying the condition is still improbable because generally a crack at the other side of the hole initiates before it reaches sufficient length a, transiting to the model of two crack at a hole.

Offset correction varies depending on b related to $W/2$.
For b < W/2:

$$F_{off} = \frac{sin\left(\left(\frac{d + a}{b - a/2}\right)\left(\frac{W - 2b}{W}\right)\right)}{\left(\frac{d + a}{b - a/2}\right)\left(\frac{W - 2b}{W}\right)} F_C \qquad\qquad (8.18)$$

where:

$$F_C = \begin{cases} 1 & \text{if } F_G < 0.0468 \\ \left(1 - (0.45F_G - 0.021)\left(\frac{a}{b - d/2}\right)^{16}\right) & \text{if } F_G \geq 0.0468 \end{cases} \qquad\qquad (8.19)$$

$$F_G = \min\left\{0.7; \left(\frac{2b}{W} + \frac{d}{2b}\right)\right\} \qquad\qquad (8.20)$$

For b > W/2:

$$F_{off} = F_{AFHB} F_{BW} \qquad\qquad (8.21)$$

$$F_{AFHB} = 1 + \frac{\sqrt{\left(sec\left(\frac{\pi d}{14}\left(\frac{2}{W - b} + \frac{1.5}{b}\right)\right)\right) - 1}}{1 + 0.21 \sin\left(8 \tan^{-1}\left(\frac{2b - W}{W}\right)^{0.9}\right)} \qquad\qquad (8.22)$$

$$F_{BW} = 1 + (F_{max} \sin(\pi \, tanh(2\delta_{BW}^{1.1} + (1.18\delta_{BW})^7))) \qquad\qquad (8.23)$$

where:

$$\delta_{BW} = \frac{d + a}{2b - a} \qquad\qquad (8.24)$$

$$F_{max} = \frac{1}{2 \exp\left(10\left(1 - \frac{b}{W}\right) + 4.2\left(1 - \frac{b}{W}\right)^2 + \left(3\left(1 - \frac{b}{W}\right)\right)^{14}\right)} \qquad\qquad (8.25)$$
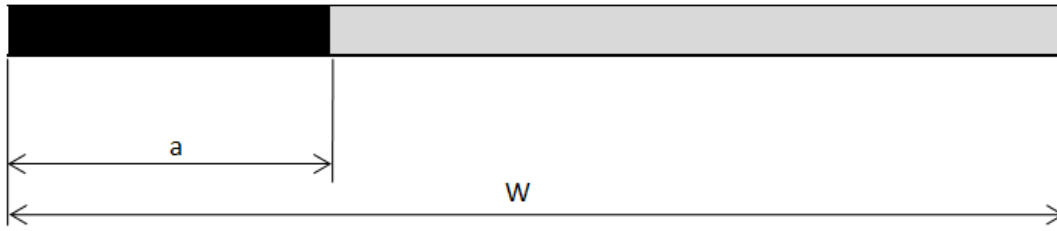
8.5.2   Edge crack

Figure 8.8 Geometry of specimen with an edge crack

When calculating stress intensity factor for an edge crack, it is important to be aware whether the in-plane bending is constrained or not. The constraint is assumed if analysed fastener row is a central row, since surrounding structure helps holding a cracked plate together. On the other hand, for boundary rows, there is nothing that would prevent excessive crack opening, thus in-plane bending is assumed during the calculation. If used for the central rows, this approach gives conservative results since it does not consider an influence of spars and stringers present in the wing structure. For row labels definition see Figure 8.9.
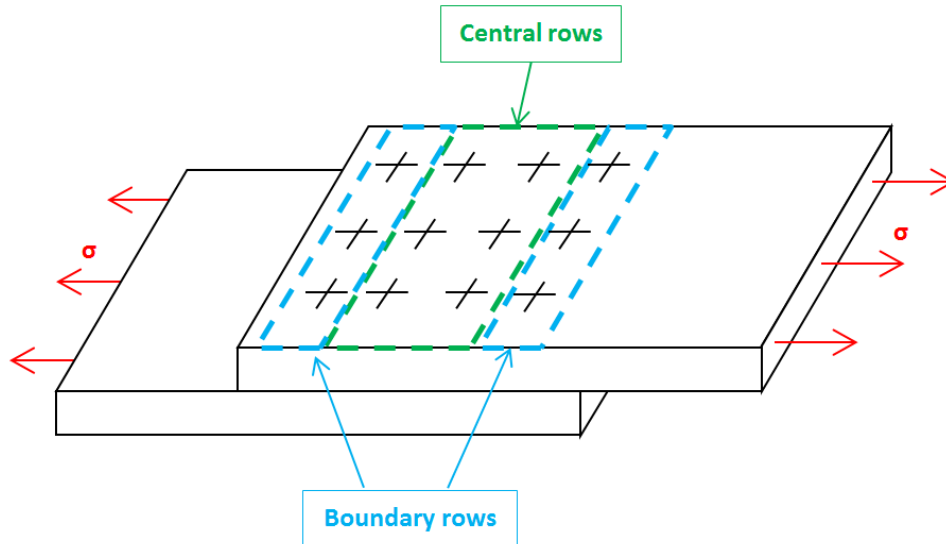

Figure 8.9 Definition of row labels for purposes of SIF calculation for the edge crack

Solution to SIF for non-constrained bending was provided by Tada [4] having accuracy better than 0.5% for any a/W.

$$\beta = \frac{\left(0.752 + 2.02\left(\frac{a}{W}\right) + 0.37\left(1 - \sin\left(\frac{\pi a}{2W}\right)\right)^3\right)}{\cos\left(\frac{\pi a}{2W}\right)} \sqrt{\frac{2W}{\pi a} \tan\left(\frac{\pi a}{2W}\right)} \qquad (8.26)$$

In case we assume restrained bending due to surrounding structure, a relation obtained by Harris [3] is applied, see eq. (8.27). This solution differs by less than 5 % for a/W < 0.12 compared to eq. (8.26). Then it gives significantly lower values of β.

$$\beta = \frac{5}{\sqrt{20 - 13\left(\frac{a}{W}\right) - 7\left(\frac{a}{W}\right)^2}} \qquad (8.27)$$
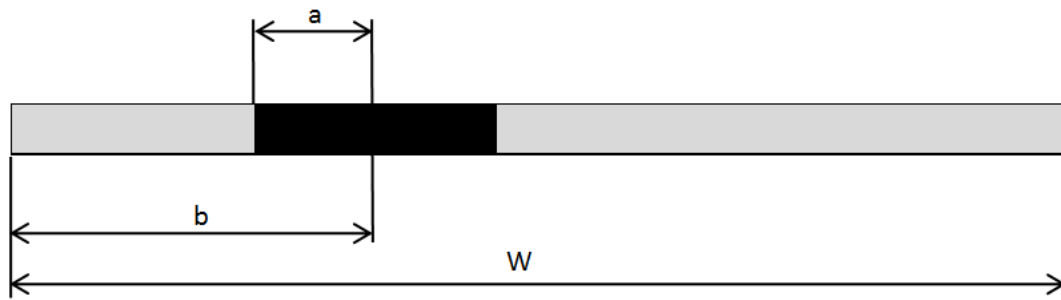
8.5.3   Centre through crack

Figure 8.10 Geometry of specimen with a central through crack

Model of the centre crack is used if the length of both cracks at a hole exceed a/r > 10. Deviations caused by using the model instead of the model of two cracks at a hole of unequal length are displayed in Figure 8.11. Apparently if both cracks are of equal length (ratio = 100 %), the error is around 5 %. Then with the increasing difference between the crack lengths (decreasing the ratio), the deviation from this value is increasing approximately linearly. It reaches 15 % at ratio 80 % in case of shorter of the cracks and 5 % at ratio around 62 % for longer of the cracks.

Commonly, unless a large stress gradient is present in vicinity of the hole (uniform stress assumed in algorithm), crack lengths does not usually vary significantly. The only exception is after a crack link-up occurs. After applying the substitution suggested by Harter [11] (see Figure 7.7) on the geometry, the ratio between crack lengths is usually significantly lower than 80 %. Thus employing the centre crack model would lead to underestimating of the SIF at the tip of the shorter crack. On the contrary, an error in SIF value for the longer crack is noticeably lower. Moreover, for the longer crack the centre crack model gives higher SIF values, hence it is conservative. To conclude, after the crack link-up happening, using a combination of the centre crack model for the longer crack and the model of asymmetrical double crack at a hole for the shorter crack is suitable.
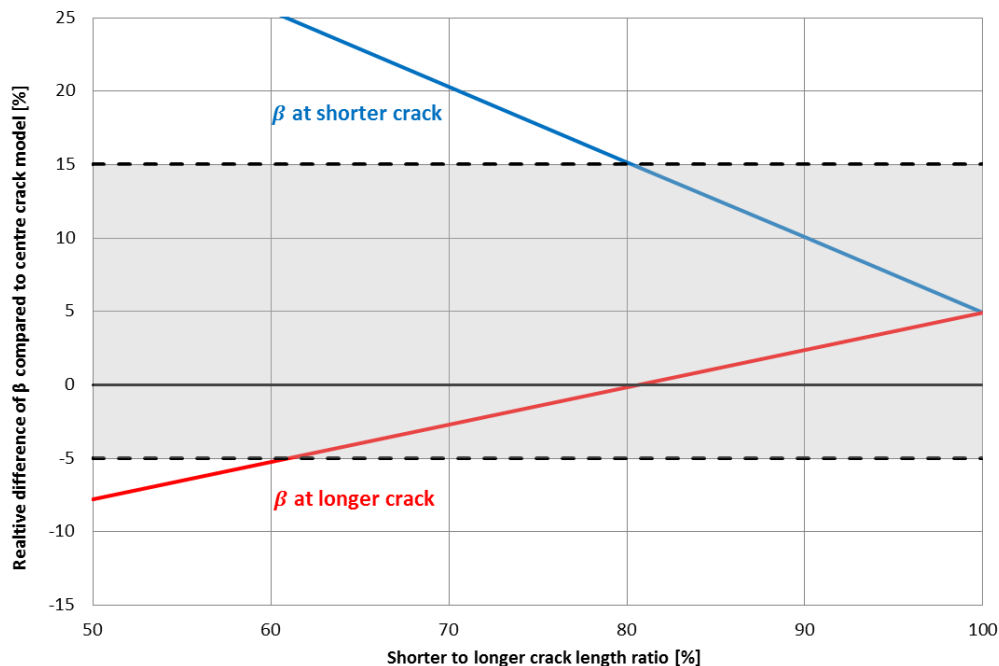

Figure 8.11 Difference of β obtained from double crack at hole of unequal length model compared to centre crack model for various crack length ratios. Ratio 100 % applies for symmetrical model.

If the crack centre is located in the centre of the specimen, i.e. b = W/2, Feddersen formula modified by Tada [4] is used, yielding error below 0.1 % for any crack length.

$$\beta = \left(1 - 0.025\left(\frac{a}{W}\right)^2 + 0.06\left(\frac{a}{W}\right)^4\right)\sqrt{\sec\left(\frac{\pi a}{2b}\right)} \tag{8.28}$$

However, if the crack is offset, more complex approach according to Harter [1] has to be applied. Stress intensity factor varies between the crack tip closer (crack tip A in Figure 8.12) and further (crack tip B) from the near plate edge; solutions are presented in equations (8.29) and (8.30). It is important to state that b marks the distance from the nearer edge to the crack centre, i.e. b < W/2 for all geometries.

$$\beta_{close} = (1 - 0.025\lambda^2 + 0.6\lambda^4 - \gamma_{cls}\lambda^{11})\sqrt{\sec\left(\frac{\pi\lambda}{2}\right)\frac{\sin\left(2\lambda - \frac{4a}{W}\right)}{2\lambda - \frac{4a}{W}}} \tag{8.29}$$

$$\beta_{far} = \left(1 - 0.025\delta_c^2 + 0.6\delta_c^4 - \gamma_{far}\delta_c^{30}\right)\left(1 + \frac{\sqrt{\sec\left(\frac{1}{7}(2\pi\lambda + 1.5\pi\delta_c)\right) - 1}}{1 + 0.21\sin\left(8\tan^{-1}\left(\frac{\lambda - \delta_c}{\lambda + \delta_c}\right)^{0.9}\right)}\right) \tag{8.30}$$

where

$$\lambda = \frac{a}{b}, \qquad\qquad \delta_c = \frac{a}{W - b}$$

Values of correction factor γ are linearly interpolated from the Table 8.1 based on the ratio b/W. The highlighted ones were obtained by extrapolation from the FEM values provided by Harter [1].

Table 8.1 Values of correction factor γ for crack tip closer (crack tip A in Figure 8.12) and further from the plate edge (crack tip B)

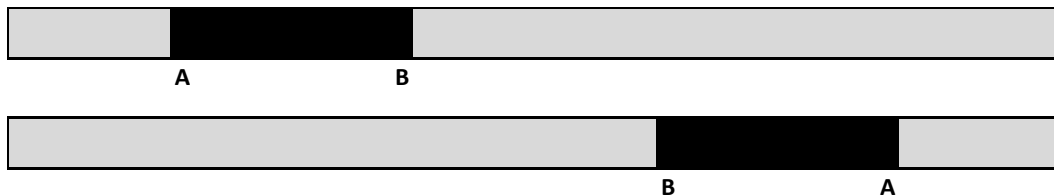| b/W	Closer crack tip (γ_{cls})	Further crack tip (γ_{far})
0	*0.5776*	*0*
0.10	0.3820	0.1140
0.25	0.1360	0.2860
0.40	0	0
0.50	0	0

Figure 8.12 Definition of closer (A) and further (B) crack tip for offset centre crack calculation

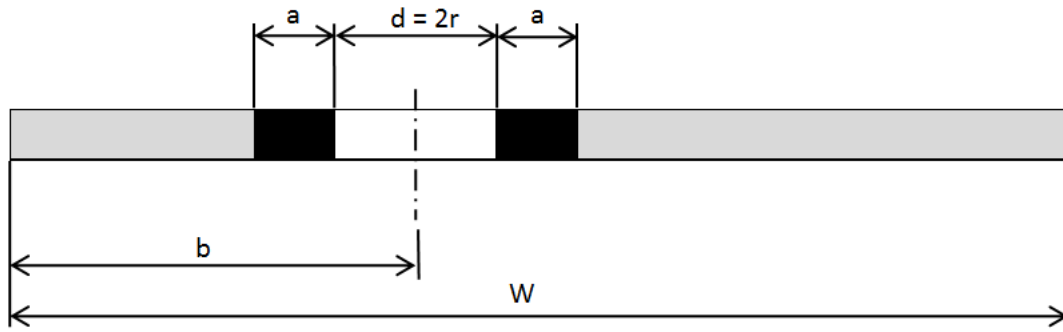### 8.5.4   Two cracks at a hole of equal length

Figure 8.13 Geometry of specimen with two cracks at a hole of equal length

The model of double crack at a hole of equal length is used for holes with cracks with relative crack length difference under 5 %, i.e. even for cracks of unequal length. As visible from Figure 8.14, difference between models is less than 3 % within the region. Moreover, the error causes β to be higher, staying thus conservative. For a/r > 10 centre crack model is used.
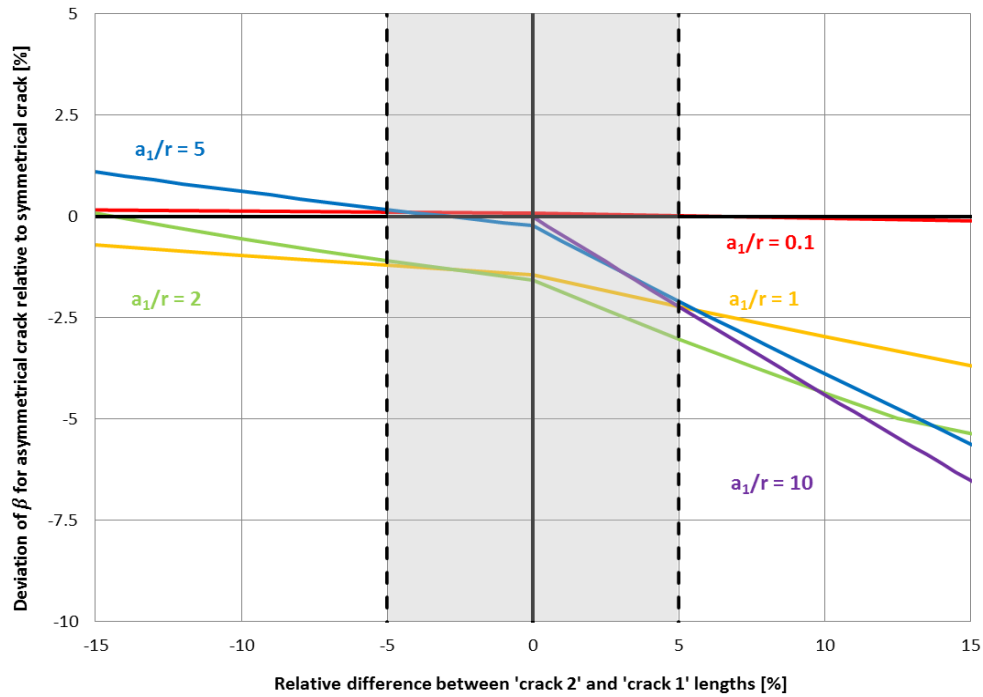
Figure 8.14 Relative difference between β value for asymmetrical and symmetrical crack related to crack length difference. 5% crack length difference marked (a_2/a_1)

The solution to the problem is provided by Harter [1] based on FEM calculations using StressCheck. Set of values is presented in Table 8.2. For longer cracks, i.e. a/r > 1.75, β might be obtained using the formula (8.31) with error less than 0.5 %.

$$\beta_\infty = \sqrt{1 + \frac{r}{a}} \qquad (8.31)$$

Table 8.2 Set of values for β calculation for two cracks at a hole of equal length for a/r < 1.75

a/r [1]	β [1]
0	3.365
0.05	3.056
0.10	2.807
0.15	2.595
0.20	2.425
0.30	2.158
0.40	1.967
0.50	1.824
0.625	1.686
0.75	1.590
1.00	1.450
1.25	1.360
1.50	1.300
1.75	1.250

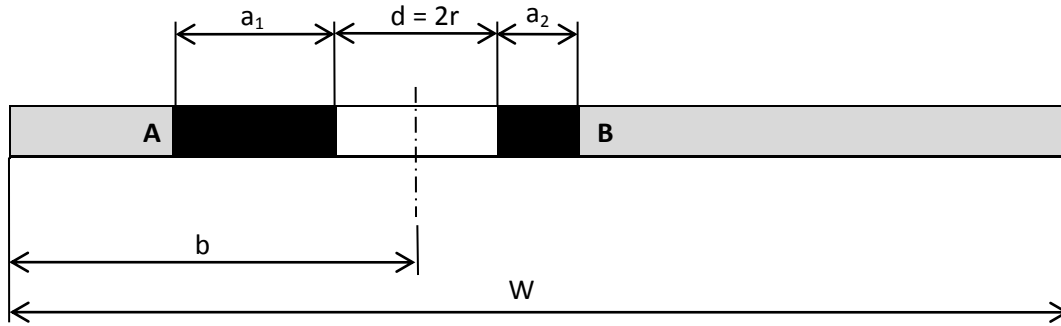### 8.5.5 Two cracks at a hole of unequal length

Figure 8.15 Geometry of specimen with two cracks of unequal length

Calculating the SIF at cracks at a hole of unequal length requires employing numerical methods because of its more complex nature. Rooke and Tweed [5] came up with a solution based on procedure by Erdogan and Gubta. Calculated values of β for crack lengths in range of a/r = 0.2 to a/r = 10 are presented in Table 8.3.

Limiting values (marked red) are derived from the stress concentration factor (SCF) for an elliptic hole based on the equation (6.15) [5], for clarity restated below. After employing the substitution by Peterson [14] presented in Figure 6.10, the SCF may be calculated with use of equation (5.14).

$$\lim_{a_2 \to 0} \frac{K_I}{\sigma \sqrt{\pi a_2}} = 1.1215 \, K_t \qquad (8.32)$$

Values highlighted by blue were not provided by Rooke and Tweed, but instead a series of simulations in AFGROW was performed in order to obtain β values for a/r > 10. Geometry of the specimen is displayed in Figure 8.16. Because the solution is for a cracked hole in an infinite plate, a large specimen width was chosen to ensure that the geometrical boundaries will not influence the solution. A hole diameter was set to be d = 2, i.e. radius r = 1 mm. Then solution for given lengths $a_{1,2}$ is automatically a solution for a combination of $(a/r)_{1,2}$.
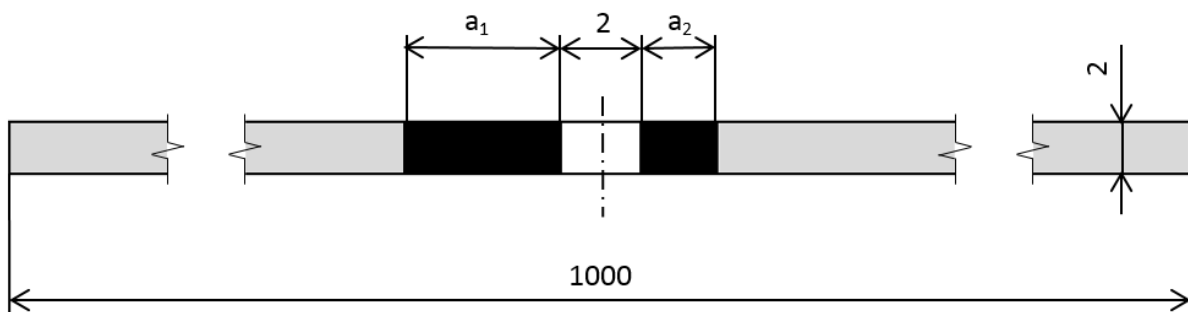
Figure 8.16 Dimensions of the specimen in [mm] used for obtaining β values in AFGROW

To obtain desired β at crack tip B (see Figure 8.15), it is necessary to interpolate between tabular data for given a_1/r and a_2/r. If β at crack tip A is desired, a_1 and a_2 must be swapped for purposes of the interpolation! For example, let us have r = 2 mm, a_1 = 4 mm, a_2 = 10 mm. Then $β_A$ is 1.522 (as a_1^*/r = 5, a_2^*/r = 2) and $β_B$ is 0.950 (as a_1^*/r = 5, a_2^*/r = 2).

Table 8.3 Values of β_∞ at crack 2 (point B) for given length of 'crack 1'

		a_1/r [1]											
		0	**0.5**	**1.0**	**2.0**	**5.0**	**10.0**	**20.0**	**30.0**	**50.0**	**75.0**	**100.0**	**200.0**
	0	3.3640	3.5751	3.8714	4.2900	5.4100	6.8200	8.5607	10.0935	12.5586	15.0389	17.1397	23.6634
	0.2	2.3730	2.5200	2.7100	3.0520	3.8660	4.8920	7.3745	8.8825	11.3095	13.7536	15.8247	22.0325
	0.3	2.0920	2.2210	2.3880	2.6900	3.4100	4.3200	6.32	7.6062	9.6787	11.7668	13.5365	18.8418
	0.5	1.7270	1.8320	1.9680	2.2130	2.8030	3.5550	4.9953	6.0036	7.6304	9.2708	10.6618	14.8685
	0.7	1.5170	1.5950	1.7100	1.9180	2.4230	3.0700	4.1982	5.0388	6.3967	7.7671	8.9297	12.4769
a_2/r [1]	**1.0**	1.3060	1.3780	1.4710	1.6430	2.0610	2.6040	3.447	4.1649	5.2781	6.4031	7.358	10.3298
	1.5	1.1270	1.1820	1.2540	1.3880	1.7190	2.1560	2.816	3.3624	4.2496	5.1488	5.9138	8.3117
	2.0	1.0300	1.0750	1.1340	1.2440	1.5220	1.8930	2.4501	2.9165	3.6763	4.4486	5.1073	7.1866
	3.0	0.9300	0.9620	1.0050	1.0870	1.3000	1.5900	2.0375	2.4112	3.0241	3.6504	4.1872	5.906
	5.0	0.8450	0.8660	0.8950	0.9500	1.0980	1.3060	1.6426	1.9229	2.3867	2.8627	3.2701	4.5483
	10.0	0.7790	0.7900	0.8060	0.8360	0.9220	1.0490	1.2657	1.4506	1.7644	2.0942	2.3823	3.3416

8.5.6   Offset correction for double crack at a hole

Both models for symmetrical and asymmetrical double crack at a hole use correction for the offset calculated by the compounding method (see Chapter 8.4). Therefore it is gained as a ratio between an offset centre crack (equations (8.29) and (8.30)) and a centre crack located in the centre of the specimen (see eq. (8.28)). Geometry is modified according to Figure 8.17, while dimensions are calculated according to relations (8.34).

$$F_{off} = \frac{\beta_{offset}}{\beta_{centre}} \qquad (8.33)$$
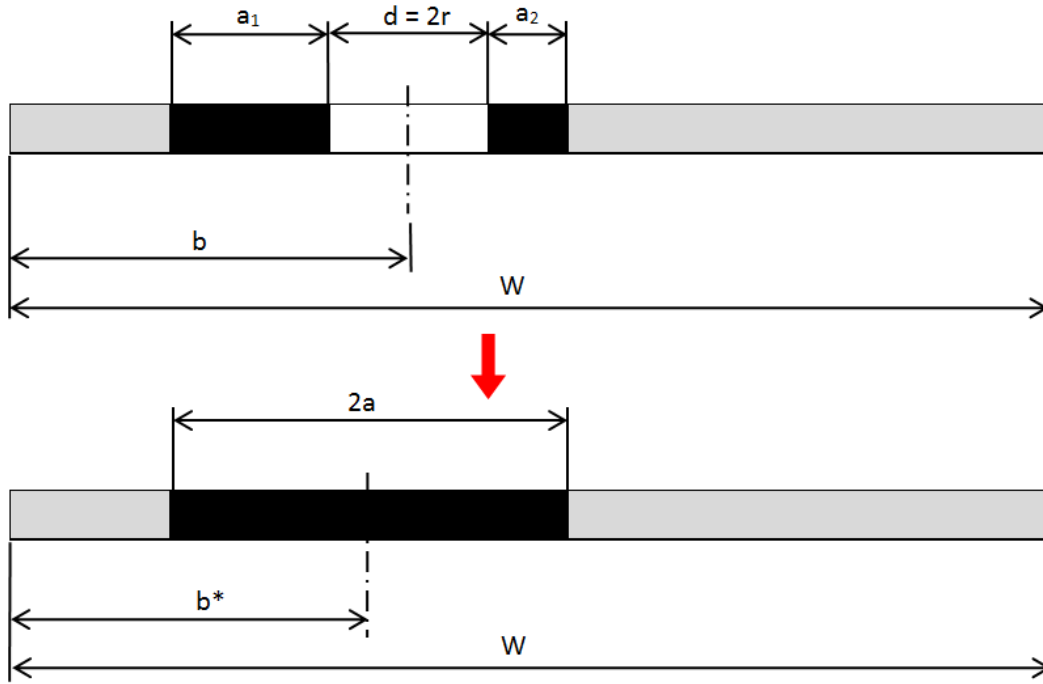

Figure 8.17 Transformation of geometry of a double crack at a hole into a centre crack

$$a = \frac{a_1 + a_2}{2} + r \qquad\qquad b^* = b - \frac{a_1 - a_2}{2} \qquad (8.34)$$

8.6   Crack interaction

If several cracks are present in the specimen, the SIF at the crack tip is influenced not only by the crack and specimen geometry, but also by the presence of other cracks. According to Harter [1], even configuration with two cracks in the finite plane is very complex task because of high amount of possible geometries. Adding more cracks would lead to enormous number of combinations, thus a simplification is necessary.

The solution for β_{cor} might be obtained by FEM [1], [2] or by analytical methods [4]. In terms of the task, we assume simplification of basic geometry (see Figure 8.18a) when calculating β_{cor} for crack A and B. The hole (cracked or uncracked) further from the analysed crack is assumed to be a through centre crack. On the other hand, the adjacent crack might be treated depending on whether it is cracked or not. This is depicted in Figure 8.18b and Figure 8.18c.
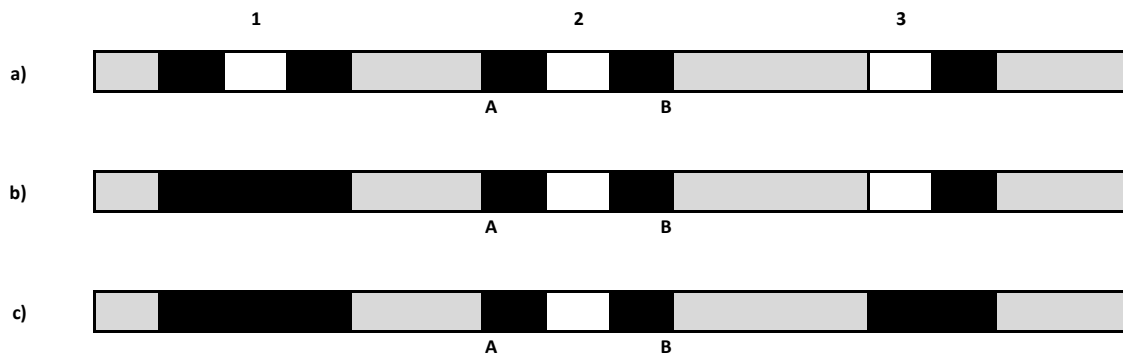

Figure 8.18 Geometry of the specimen with multiple holes:
a) basic geometry, b) simplified geometry for calculation of SIF at crack tip B,
c) simplified geometry for calculation of SIF at crack tip A

8.6.1   Crack approaching an uncracked hole

If a crack is approaching an uncracked hole (see crack B in Figure 8.18b for simplified geometry), a solution proposed by Newman [2] is implemented. The solution is presented in a form of a table, see Table 8.4, dimensions are displayed in Figure 8.19. Highlighted values were not provided by Newman, but they have been extrapolated from available ones instead to satisfy as many as possible geometries. For these purposes, Matlab functions *inpaint_nans* by D'Ericco [20] (green) and *polyfit* (blue) were used. An error caused by extrapolating data is negligible since a use of extrapolated values is improbable for any usual geometry.
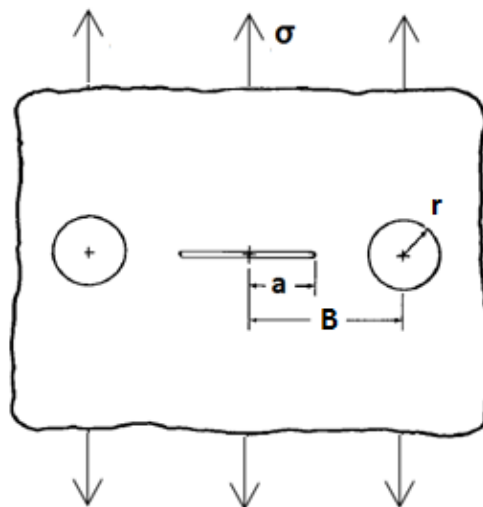

Figure 8.19 Geometry of a crack approaching the uncracked hole [2]

61

Table 8.4 Values of shape function β at crack approaching a hole [2]

		B/r [1]					
		1.15	**1.25**	**1.5**	**2**	**4**	**∞**
	0	*4.3924*	*3.2606*	*2.1514*	*1.4676*	*1.0755*	1
	0.01	4.3975	3.263	2.153	1.4687	1.0761	1
	0.1	4.416	3.2739	2.1612	1.4738	1.0774	1
	0.2	4.4751	3.3143	2.1875	1.4898	1.0816	1
$\dfrac{a}{B-r}$	**0.3**	4.5853	3.3856	2.2338	1.5183	1.0892	1
	0.4	4.7308	3.4946	2.3045	1.5624	1.1017	1
[1]	**0.5**	4.9593	3.6538	2.4076	1.6279	1.1215	1
	0.6	5.289	3.885	2.5575	1.7249	1.1538	1
	0.7	5.7816	4.2271	2.7824	1.874	1.2101	1
	0.8	*6.4363*	4.7825	3.1504	2.123	1.3202	1
	0.9	*7.4152*	5.8028	3.8661	2.635	1.5927	1
	1	*8.5243*	*6.9246*	*4.6431*	*3.1856*	*1.8794*	1

8.6.2   Crack approaching a cracked hole

If the opposing hole is cracked (see crack A in Figure 8.18c for simplified geometry), a solution by Yokobori and Isida [4] is used. This solution was developed by complex potentials method, giving exact results. Downside of this solution is that it does not provide β values for the crack tip further from the neighbouring crack. This is not the case of solutions provided by Rooke and Cartwright [3] in Ch. 1.2.3. However, it is far more complex than solution in [4], so to save computational time the former was implemented. The geometry of the configuration is presented in Figure 8.20; solutions are presented in equations (8.35) and (8.36).
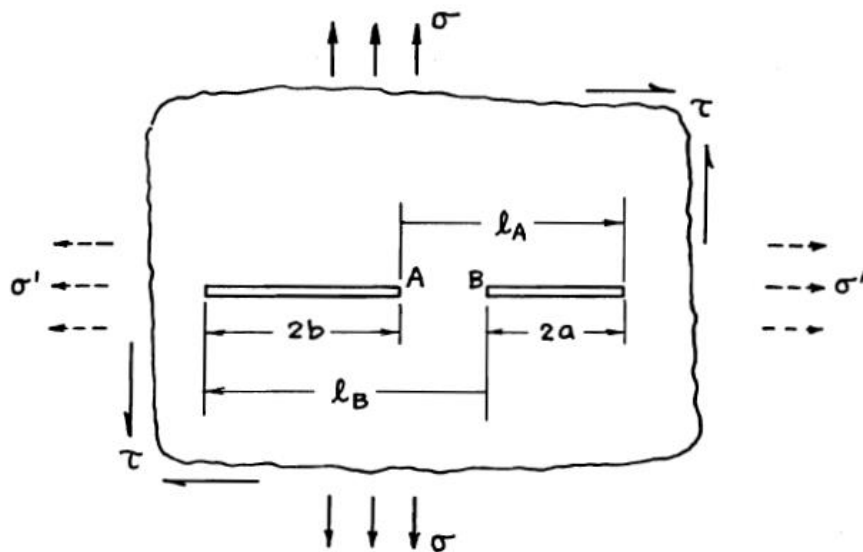
Figure 8.20 Geometry of configuration of two neighbouring cracks [4]

$$\beta_A = \frac{1}{\sqrt{1 - \alpha_A}}\left(1 - \frac{1}{\alpha_B}\left(1 - \frac{E(k)}{K(k)}\right)\right) \tag{8.35}$$

$$\beta_B = \frac{1}{\sqrt{1 - \alpha_B}}\left(1 - \frac{1}{\alpha_A}\left(1 - \frac{E(k)}{K(k)}\right)\right) \tag{8.36}$$

where

$$\alpha_A = \frac{2a}{l_A} \qquad\qquad \alpha_B = \frac{2b}{l_B} \qquad\qquad k = \sqrt{\alpha_A \alpha_B}$$

E(k) is elliptic integral of the first kind and *K(k)* is elliptic integral of the second kind:

$$K(k) = \int_0^{\pi/2} \frac{d\phi}{\sqrt{1 - k^2 sin\phi}} \tag{8.37}$$

$$E(k) = \int_0^{\pi/2} \sqrt{1 - k^2 sin\phi}\; d\phi \tag{8.38}$$

Approximate solutions to integrals (8.37) and (8.38) were proposed by Vatankhah [7]. The error of the solution for the integral of the first kind is below 0.31 % and for the second kind less than 0.12 %.

$$K(k) \approx \frac{0.371}{\sqrt{1 - 0.977\; k^2}} + \frac{1.195}{\sqrt{1 - 0.411\; k^2}} \tag{8.39}$$

$$E(k) \approx 0.406\sqrt{1 - 0.978k^2} + 1.165\sqrt{1 - 0.348k^2} \tag{8.40}$$

Both solutions [3] and [4] are developed for the infinite plane. Finite width effects are considered in solutions for a single hole/crack, see chapter 8.5. If more than two cracks are present in the specimen, the SIF is increased even more. To evaluate its rate, a method described in next chapter is employed.

8.6.3   Influence of other cracks

To take in consideration influence of the further cracks, it is necessary to compound shape functions for every pair of crack tip and holes in the structure. For higher number of holes, this approach would lead to a large number of calculations. However, according to [22] if space between two holes is greater than 3 times a hole radius (usually met), considering only effects of two neighbouring holes gives error under 3 %. Therefore we can neglect this effect.

Naturally, the presence of other cracks does have an influence on the SIF at the crack tip, by increasing the load due to net section loss. It is described by a coefficient below:

$$K_{NS} = \frac{W}{W - \sum_{i=1}^{j} a_i + \sum_{i=1} a_i} \tag{8.41}$$

where *i* − index of an inspected cracked hole and *i+1* its neighbour, *j* − number of fasteners, *W* − width of the specimen, $\sum_{i=1} a_i$ − sum of crack lengths at the inspected hole.

9   Residual strength

As required by FAR 23.573 (b) (see chapter 3.1), the structure must be able to withstand the critical limit flight loads during the operation. The problem is that with increasing extent of damage, whichever local or at multiple sites, the ability of the structure to withstand such loads is decreasing to the level when the structure would fail.

To evaluate the point when this critical state occurs, several failure criteria were developed, as presented in [6]:

   − net section yield
   − unstable tear
      − apparent fracture toughness
      − crack growth resistance curve (R curve)
      − EPFM criteria (J-integral resistance curve, crack tip opening displacement, etc.)

In addition, freedom from buckling would be necessary to consider. However, because the buckling is already evaluated for the structure with local damage, i.e. one large crack (equivalent to developed stage of MSD), in compliance with FAR 23.573, it is not included in the MSD analysis.

9.1   Net section yield

The simplest of the criteria is based on comparison of net section stress with the yield strength $R_{p0.2}$ or the flow stress σ_0 of the material. The flow stress is usually estimated as an average value of yield and ultimate strength of the material. This criterion should be considered mainly for the uncracked structure.

$$\sigma_{RS}\frac{W}{W-\Sigma a} \geq R_{p0.2} \ \ (\text{or } \sigma_0) \tag{9.1}$$

where W is total width of the specimen, σ_{RS} is limit load case stress level and Σa is total length of cracks in the cross-section.

9.2   Unstable tear

9.2.1   Fracture toughness

As a net section yield criterion serves well for evaluating of the uncracked structures, for a cracked structure, the Irwin's criterion based on stress intensity factor is more suitable. Despite its simple definition, see equation (9.2), a value of fracture toughness K_C is required to be known.

$$K \geq K_C \tag{9.2}$$

The fracture toughness (FT) is a material property, measuring resistance of the material to the fracture. Compared to yield strength, it depends not only on temperature or strain state but also on the stress state. That is the reason why the thickness of the test specimen has to be considered in the analysis.

When the thickness is in an order of the crack tip plastic zone size, the FT reaches its maximum value. On the contrary, with increasing thickness of the specimen, the stress state transits to the plane strain, leading to decrease of the plastic zone size. The FT gradually falls to the value of plane strain fracture toughness K_{IC}. This value is virtually independent of thickness. Figure 9.1 displays the relation between the specimen thickness and fracture toughness.
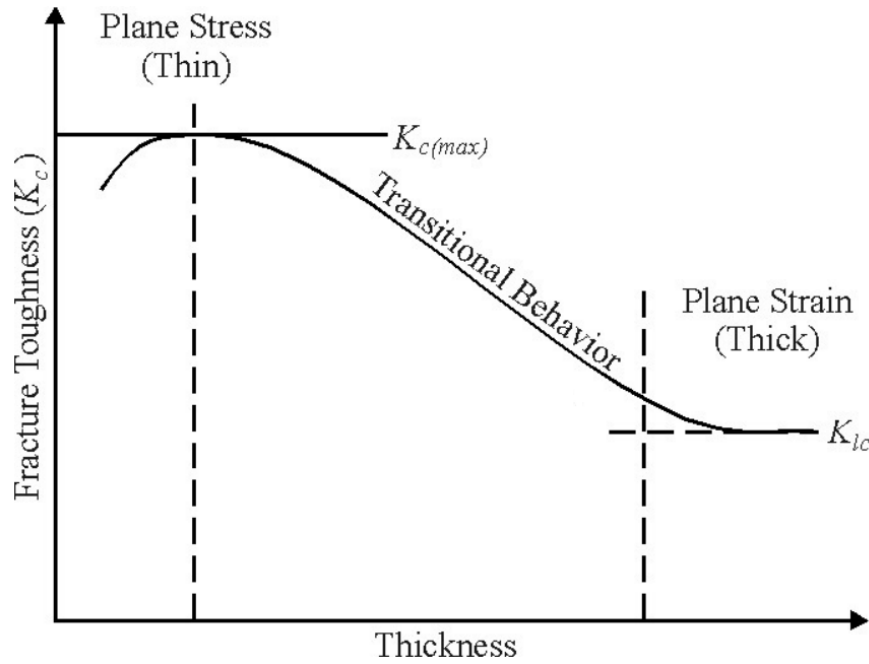
Figure 9.1 Fracture toughness as a function of thickness [6]

9.2.2   Crack growth resistance curve

For thin metal sheets and tough materials, i.e. under the plane stress state, a tearing mode of fracture is typical. Because a large amount of energy is consumed for plastic deformation creation at the crack tip, the crack growth resistance (K_R) of the material is higher than for a part under the state of plane strain.

In Figure 9.2a there is fracture behaviour as a function of SIF displayed, where applied stresses are $\sigma_A > \sigma_B > \sigma_C$. These curves can be assembled into one curve, using the amount of movement of the crack as a variable. A curve obtained in such a way is called a crack growth resistance curve, also known as an R curve, and is displayed in Figure 9.2b. Apparently the SIF associated with the fracture is not constant and furthermore it depends on the crack length as well. As a result, employing a two-parametrical criterion is required.
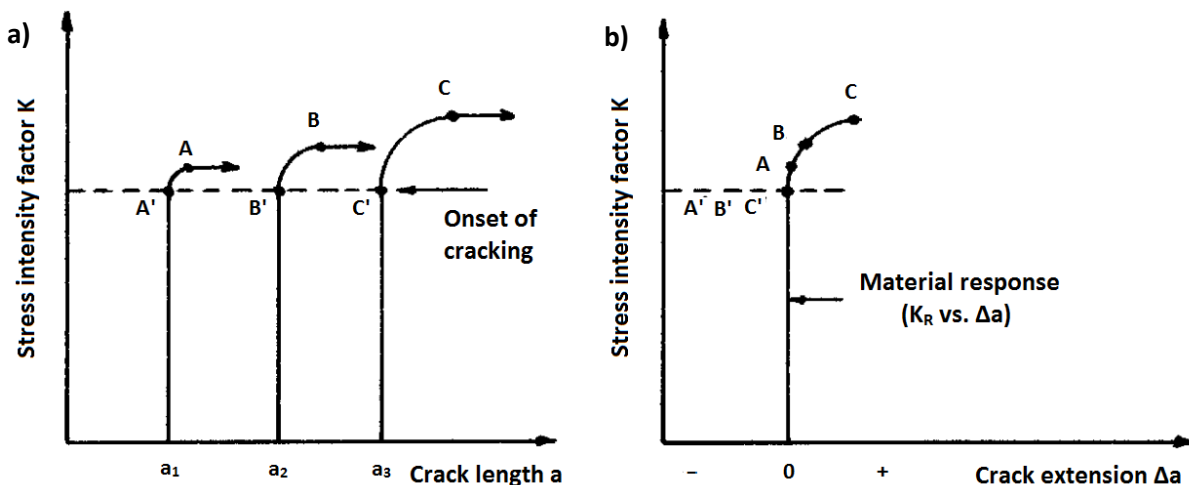
Figure 9.2 Tearing fracture behaviour and derivation of R curve; $\sigma_A > \sigma_B > \sigma_C$ [6]

A tearing fracture occurs when SIF at the crack tip reaches or exceeds the crack growth resistance. The other condition necessary to be met is that energy available to extend the crack surpasses the crack growth resistance, i.e. the rate of change of K exceeds the rate of change of K_R. The criteria are displayed below [6].

$$K \geq K_R \hspace{6cm} (9.3)$$

$$\frac{\partial K}{\partial a} \geq \frac{\partial K_R}{\partial a} \hspace{5cm} (9.4)$$

Based on conditions (9.3) and (9.4), various crack growth behaviour depending on stress level may be defined, see Figure 9.3. For low stress (σ_1), hence low stress intensity factor ($K < K_R$), the crack is stable, i.e. does not grow. If $K = K_R$, but the condition (9.4) is not satisfied, even the crack grows, its growth is stable (σ_2). However, if both conditions are met (high SIF, σ_3), the crack grows unstably, i.e. fracture occurs.
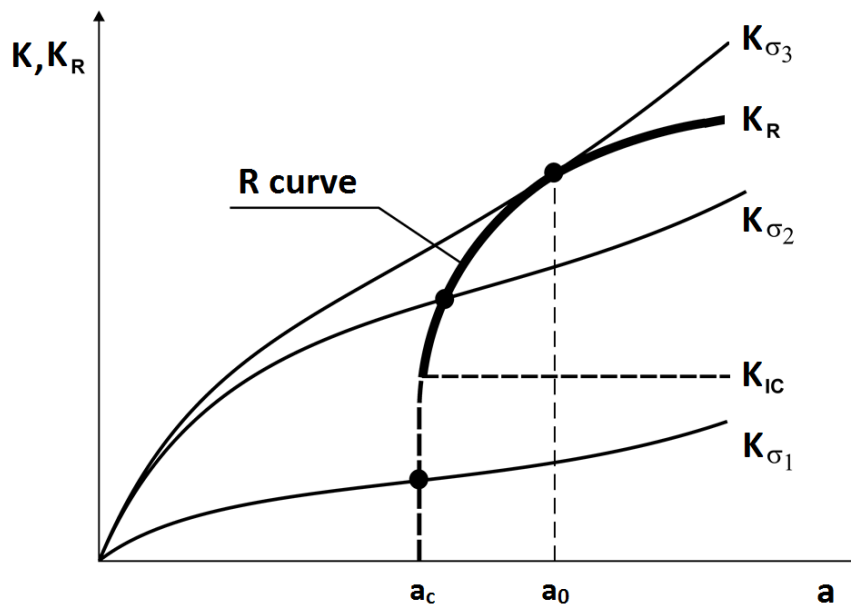

Figure 9.3 R curve and various load levels; $\sigma_1 < \sigma_2 < \sigma_3$ [19]

9.2.3   Elastic-plastic fracture mechanics criteria

For completeness, criteria used for fracture evaluation in elastic-plastic fracture mechanics are stated. Because the EPFM is not used in AIMA, only superficial information is provided. The most common approaches used are J-integral and crack tip opening displacement (CTOD) method.

The J-integral approach works analogically to the R-curve method, using J_R curve instead of R curve. Criteria are displayed in (9.5) [6], where J is an applied J-integral and J_R is a value of J-integral representing the material's fracture resistance.

$$J \geq J_R \hspace{3cm} \frac{d\sqrt{J}}{da} \geq \frac{\partial\sqrt{J_R}}{\partial a} \hspace{2cm} (9.5)$$

Another way how to describe fracture behaviour is by a critical value of CTOD δ_c. The extent of crack tip opening depends on geometry and loads, and is in a unique relation with J-integral for given material, as stated in [31].

10 AIMA

10.1 Introduction

Based on the theory presented in the thesis, an algorithm for MSD analyses was developed, named AIMA: Aircraft Industries MSD Analysis. The algorithm is written in Matlab version 7.10.0 (R2010a) with full compatibility with GNU Octave 4.0.0, as an open-source alternative to Matlab. However, to run the algorithm on Octave, several packages have to be installed. The script *first_run.m* serves this purpose.

It is important to note that performance of Octave is much lower than of Matlab, since the Just-in-time compiler is still not implemented in Octave. This feature helps accelerating for-loops by compiling the content.

10.2 Algorithm design

AIMA is designed to offer a complete MSD analysis of a WFD susceptible structure, based on a probabilistic approach (Monte Carlo simulation). It supports majority of all possible lap or splice joint configurations by enabling entering an arbitrary number of connected parts, allowing various positions of fasteners and thickness transitions in direction parallel and perpendicular to the remote loading. A structure is loaded by local remote stresses and by loads induced by fastener forces. These loads are usually obtained as a result of finite element method (FEM) analysis. Results include fatigue life to the crack initiation of single fasteners, fatigue lives of the structure during the Monte Carlo runs and their mean value, and finally, a cumulative probability function of WFD occurrence in the structure.

A flow chart of the algorithm is presented in Figure 10.1. Italic texts represent actions, diamonds with dashed frames are dialogs and texts in quotation marks are names of variables. The rest, i.e. non-italic signs are names of functions called. A design, functionality and restrictions of constituent functions of the algorithm are presented in the next sub-chapters.

A function *run.m* serves as a main function which calls sub-routines when necessary. Dashed fork blocks are dialogs within the main function. The function is divided into three main parts:

 − data preparation
 − Monte Carlo loop
 − post-processing

To enhance the performance of the algorithm, all variables that are not dependent on randomized variables are predefined or pre-calculated before the Monte Carlo loop itself starts. Afterwards, a core of the program follows. Result of the MC simulation is a set of points when the WFD failure occurred. These data are consequently processed in order to offer the user all desired outputs.
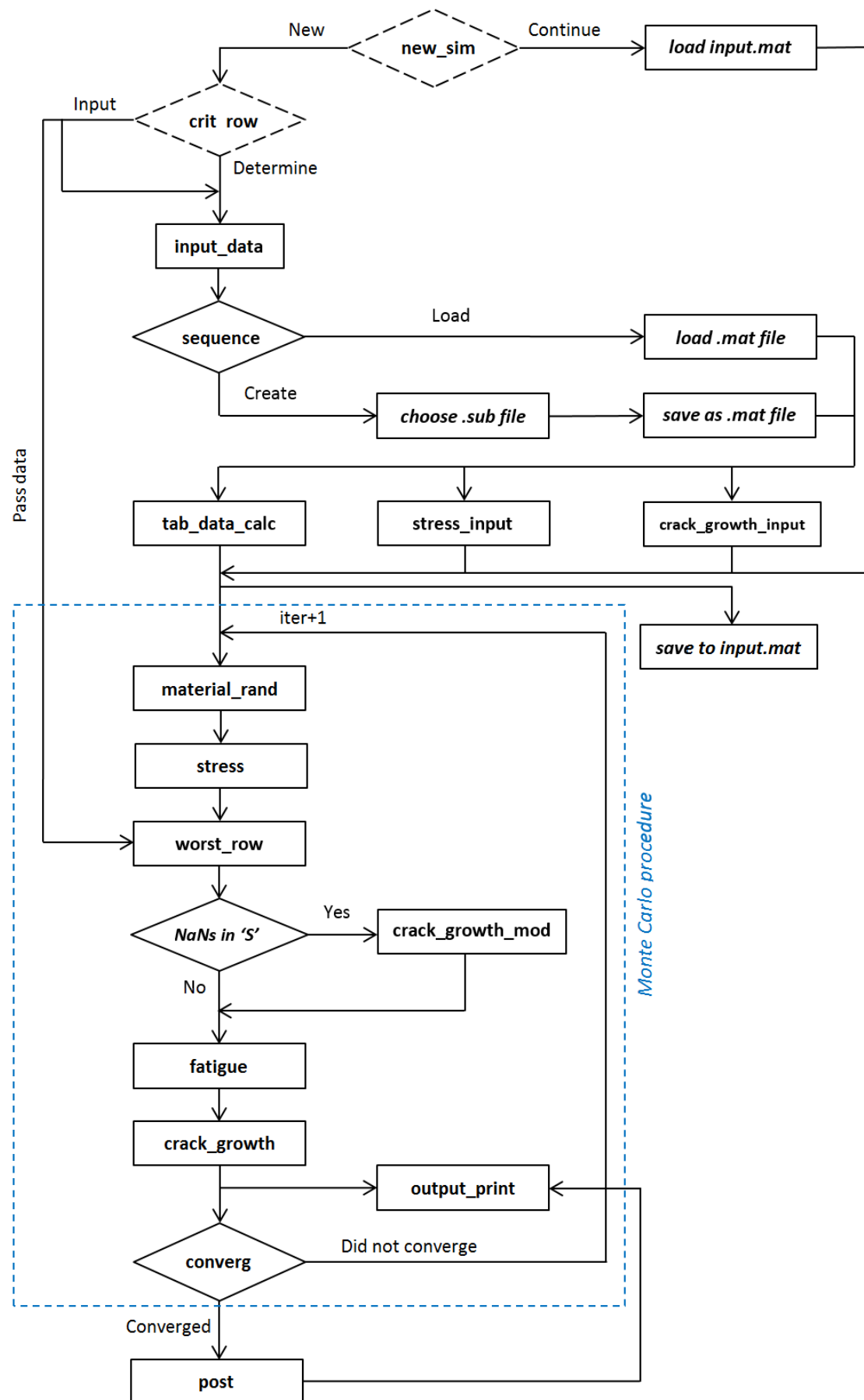
Figure 10.1 AIMA algorithm flowchart

10.2.1   run.m

run.m is a main function of AIMA. It calls all sub-functions necessary for the analysis. Before proceeding to executing the code itself, it clears both workspace and command line window.

After calling the *run.m*, a user is asked by a dialog to decide whether he wants to create a new simulation or to continue, i.e. add more MC runs from the provided input data. This is beneficial if the user decided to stop MC simulation prematurely, e.g. after 50 runs. If a new simulation is started, sub-functions are called successively until the Monte Carlo loop is reached. Then all variables in the workspace are saved into a file *input.mat,* located in the folder *\data*. If the user desires to continue the simulation from previously saved point, the file *input.mat* is loaded, providing all variables for the Monte Carlo loop.

Users often dispose of the MSD critical part and the row position, for example based on the experiment. In that case, answering "Input" on a dialog question is recommended. The user is able to enter ID of the critical part and the fastener row. Otherwise, AIMA determines them (with use of function *worst_row.m*).

Besides, the user is asked to define convergence criteria of Monte Carlo simulation and maximum allowed number of runs. It is important to note that the simulation requires at least twice the confidence band length runs to achieve the convergence. It is strongly recommended to leave convergence band width and length at default values. If the user cancels the dialog, pre-written default values are used.

10.2.2   input_data.m

This function is responsible for processing all the data provided by the user in a form of an Excel file. All standard Excel suffixes *.xls*, *.xlsx*, *.xlsm*, *.xltx* and *.xltm* are supported; however open source alternatives like OpenOffice.org were not tested for compatibility. An example input file of the test specimen described in Figure 10.6 is shown in Appendix A (load data differ, since for the specimen all by-pass stresses and forces were set to zero).

10.2.3   sequence.m

A loading sequence is an essential part of the crack growth prediction analysis. The format of a sequence file in AIMA is based on the AFGROW spectrum file *.sub*, with preserving the full compatibility. A passage of the sequence *.sub* file is displayed below:

```
34.62       22.02       1
34.62       28.32       1
34.62       22.02       1
34.62       28.32       3
40.92       22.02       1
34.62       28.32       4
40.92       22.02       1
34.62       28.32       2
40.92       28.32       1
```

The first two columns represent the maximum and minimum stress of the cycle. The last column expresses a number of repetitions of given cycle, i.e. row.

For improving the performance of the algorithm, a sequence is rearranged in such a way that only maxima and minima of the cycles are present, eliminating thus the third column. That means that if a cycle appears three times in a row according to the *.sub* file, it is put in the sequence three times. Even though this approach requires more memory, it simplifies the sequence in the form

which can be processed faster. Furthermore, even whole spectrum of L 410 NG requires circa 70 MB of RAM memory, a negligible amount in terms of present computers. The processed sequence is saved as a *.mat* file, allowing thus faster future use.

During the run of AIMA, the user is asked by a dialog whether he wants to load already existing *.mat* file or to create a new sequence. In the latter case, he is demanded to choose sequence *.sub* files. If more files are chosen they are arranged in an alpha-numerical order. For this reason, it is recommended that all *.sub* files should differ only in ending number. A principle of processing the sequence into a structure *sq* with members *value*, *dS* (representing peak-to-peak stress amplitude Δσ) and *R* (for stress ratio) is presented below. Calculation of *Δσ* and *R* takes place in the function *crack_growth_input.m*.

SQ_01.sub			**sq.value**	**sq.dS**	**sq.R**	
34.62 22.02	1		34.62 22.02	12.60	0.6360	
34.62 28.32	3		34.62 28.32	6.30	0.8180	
			34.62 28.32	6.30	0.8180	3x
SQ_02.sub			34.62 28.32	6.30	0.8180	
40.92 22.02	2		40.92 22.02	18.90	0.5381	2x
34.62 28.32	1		40.92 22.02	18.90	0.5381	
			34.62 28.32	6.30	0.8180	
SQ_03.sub			40.92 22.02	18.90	0.5381	
40.92 22.02	1		34.62 28.32	6.30	0.8180	
34.62 28.32	2		34.62 28.32	6.30	0.8180	2x
40.92 28.32	1		40.92 28.32	18.90	0.5381	

10.2.4   tab_data_calc.m

The only task of this function is to load tabular data saved as *.txt* files into workspace. The text files are used to prevent compatibility issues between Matlab and Octave. The data include following tables:

- cumulative frequencies for gust spectrum (*cumul_freq_gusts.txt*)
- cumulative frequencies for manoeuvres spectrum (*cumul_freq_manoeuvres.txt*)
- cumulative frequencies for landing (*cumul_freq_landing.txt*)
- data for β calculation of a double symmetrical crack at hole for a/r ≤ 1.75 (*HDblS.txt*)
- data for β calculation of a double asymmetrical crack at hole (*HDblA.txt*)
- data for β calculation of crack interacting with a crack or a hole (*beta_infl_hole.txt*)

The form of typical *cumul_freq_*.txt* files is presented in appendices B to D.

10.2.5   stress_input.m

Once data were imported from the input Excel spreadsheet, some geometrical parameters are necessary to modify to be usable in the stress calculation. Moreover, a variable *sym* is created, storing information about symmetry of the analysed structure.

10.2.6   crack_growth_input.m

The function carries the initial values of variables used in *crack_growth.m*, as well as commands for processing a sequence (creating members *.R* and *.dS*, as described in chapter 10.2.3) and preparation of geometrical characteristics required for calculation.

10.2.7 material_rand.m

When producing any machines, it is impossible to manufacture constituent parts of semi-products with the same material properties. To consider this factor, guaranteed material properties (or defined by some confidence level) may be used. Another approach, suitable for the Monte Carlo simulation, is to exploit this random behaviour of the properties. Therefore, values of Young's modulus E and yield strength $R_{p0.2}$ are randomized for every MC run (normal distribution assumed).

But what if two or three parts in the joint origin from the same semi-product series? Then the function assigns the same value of E and $R_{p0.2}$ for given parts. The user can control which parts are from the same series by assigning them identical ID in the header of *Material_Properties* sheet of the input Excel file, as shown in Figure 10.2. The results of material properties generation (7475-T7351 alloy [38]) for both examples are shown in Table 10.1. Identical values of E and $R_{p0.2}$ of parts 2 and 3 in Case b) are highlighted.

Table 10.1 Comparison of generated material properties

Part ID		1	2	3	4
Case a)	Young's modulus [MPa]	70034	71901	66007	70502
	Yield strength [MPa]	421.36	407.28	414.85	421.57
Case b)	Young's modulus [MPa]	69081	71405	71405	71301
	Yield strength [MPa]	424.42	408.14	408.14	432.72

a)	PART			
	PART 1	PART 2	PART 3	PART 4
Identification of semiproduct series (identical number means that parts are made of the same series of semiproduct)	0	1	2	3

b)	PART			
	PART 1	PART 2	PART 3	PART 4
Identification of semiproduct series (identical number means that parts are made of the same series of semiproduct)	0	2	2	3

Figure 10.2 Material ID of the manufacturing series;
a) each part is from different series, b) parts 2 and 3 are from the same series '2'

10.2.8 stress.m

After obtaining the Young's modulus randomised value, we can proceed to the calculation of stresses at each fastener hole. It is carried out according to the methodology described in chapter 5.

10.2.9 worst_row.m

The purpose of the function is to find the most MSD critical row and stresses at the fasteners. If a user chose the option "Input" when "Determine critical row of fasteners or Input ID of the row?" dialog popped up, the IDs of the critical row and the part are already defined. This is a recommended approach if relevant test data are available. If the user let the application to find the critical part and row, the function *worst_row.m* finds them. A simple criterion is used: the fastener with the maximum stress determines the critical row, since the initiation period length depends on the stress with power of S-N curve exponent.

Moreover, the function determines whether the row is central or boundary (for definitions see Figure 8.9), which serves for the calculation of stress intensity factor for the edge crack.

10.2.10 crack_growth_mod.m

The function is run only in case any position in the row contains *NaN* stress value, i.e. the variable *S.max.nan* calculated by *worst_row.m* is equal to 1. This situation might occur if any thickness transition along the row (i.e. a hole has zero diameter and zero stress) is present, or if there are two parallel rows with various positions of the holes, such as Figure 10.3 displays. An example of calculated stresses *S.max.val* for the first row at positions x_1 to x_n would look like this:

```
x = [10 25 30 45 50 65 70 85]
B = [15 5 15 5 15 5 15]
S.max.val = [NaN  25.50  NaN  30.25  NaN  22.75  NaN  20.00]
```

where segment widths *B* are calculated based on the values of vector *x*.

It is clear that some *NaN* values appear in the vector *S.max.val*. These would cause many problems during the crack growth prediction. Hence the function gets rid of the *NaN*s and modifies the segment lengths to the lengths between holes in a given row, i.e. calculates width of segments based only on *x* values not containing *NaN* stress. This modification results in following:

```
x = [35 55 75 95]
B = [20 20 20]
S.max.val = [25.50  30.25  22.75  20.00]
```
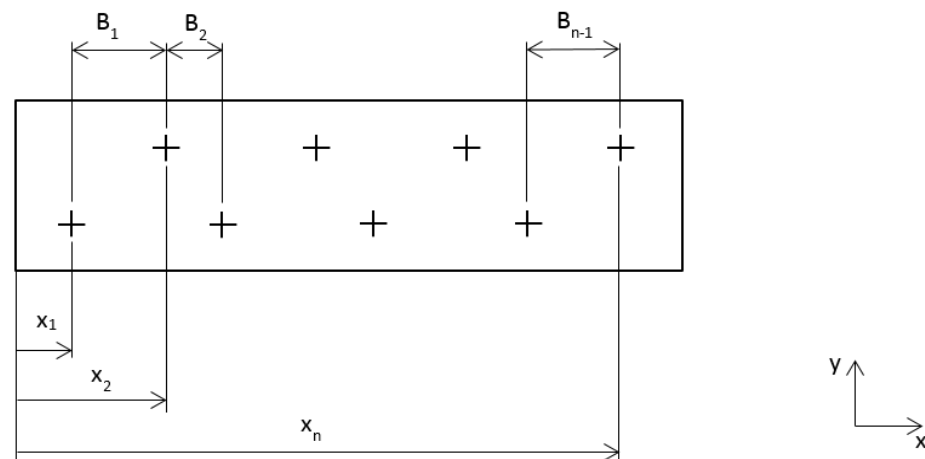

Figure 10.3 Example geometry

10.2.11 fatigue.m

The function is responsible for calculation of the crack initiation period based on the stress data coming from the *worst_row.m* function. Afterwards, the calculated values are randomized, separately for each side of the hole in expected crack growth direction, i.e. perpendicular to the remote stress direction.

If the user desires to perform fatigue analysis with applying a constant amplitude, all the moments in the *Fatigue* sheet of the input Excel spreadsheet should be set to zero.

10.2.12 crack_growth.m

It is the core and the most complex function of AIMA, responsible for crack growth prediction. It is based on the theory described in chapters 6.4, 7, 8 and 9. The flow chart of the function is displayed in Figure 10.4. The function is divided into two main parts: preparation of inputs for a crack growth loop, and the loop itself.
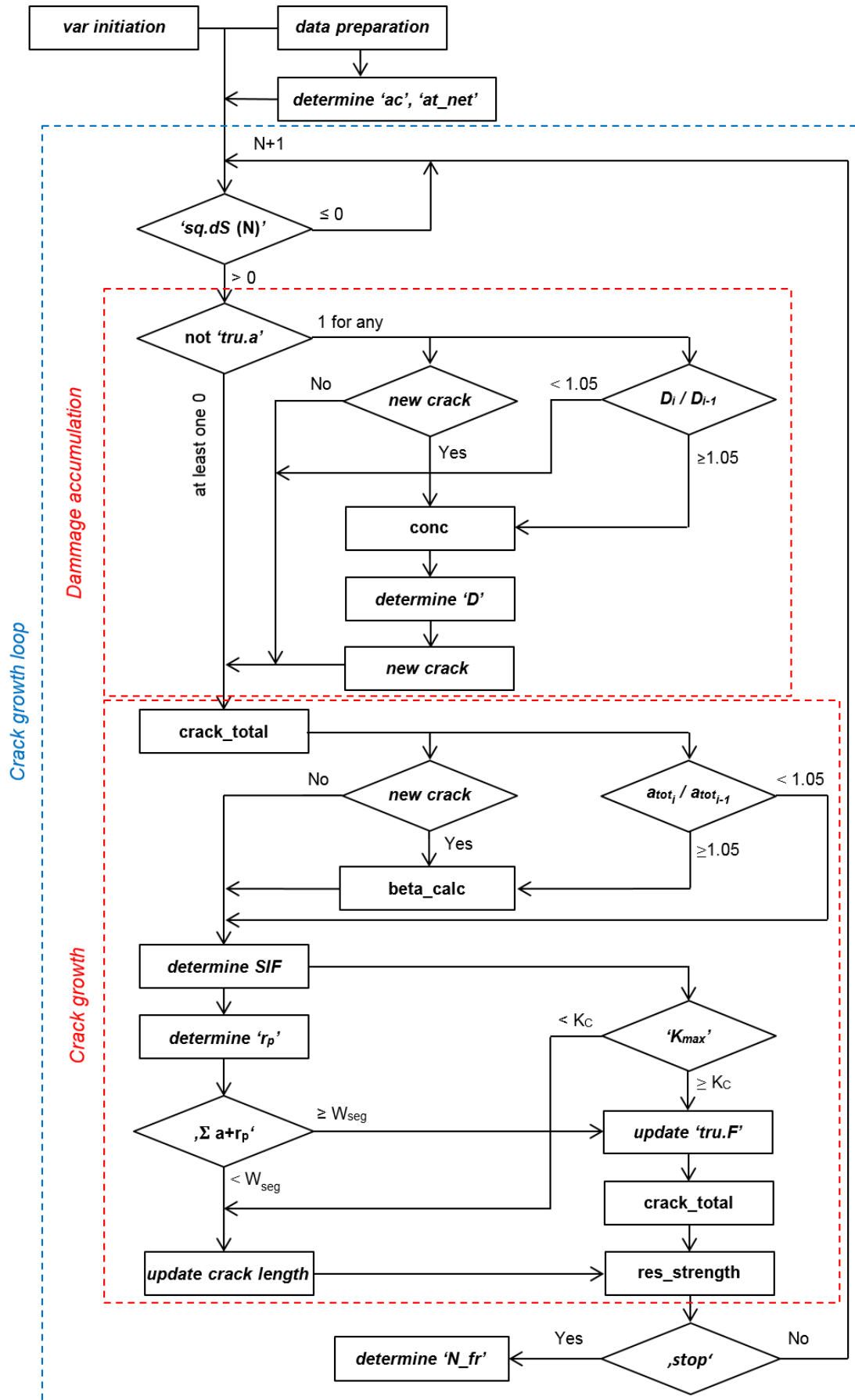
Figure 10.4 *crack_growth.m* flowchart

73

10.2.12.1 Inputs preparation

Firstly, it is necessary to pre-calculate variables that are going to be used frequently in the loop, and to define initial values of variables which are going to change over time. These variables include critical crack lengths, used for residual strength evaluation. One very important parameter is defined: stress multiplication factor (SMF), which puts into relation the stresses in the structure and the stresses used for derivation of the sequence. The SMF can be calculated as follows:

$$SMF = \frac{\sigma}{\sigma_{1g}} \tag{10.1}$$

where σ_{1g} is an average stress level during the cruise with load factor g = 1. This value is defined by the user and is located in the *Load* sheet of the input file.

Other important parameters necessary to pre-calculate are critical crack lengths for net section yield and unstable tear, which serve as stop criteria in the function *res_strength.m*.

Because of possible variable thickness along the row, the crack length multiplied by the thickness is used for assessing the structure. Critical value of a product crack length – thickness, is based on equation (9.1):

$$at_{net} = \left(1 - \frac{\sigma_{RS}}{R_{p0.2}}\right) \sum_{j=1}^{n} \left(B_{f_j} - d_j\right) t_j \tag{10.2}$$

where B_f – width of the segment as defined in Figure 5.4, d – hole diameter, j – ID of a hole, n – number of holes, σ_{RS} – limit load case stress, $R_{p0.2}$ – yield strength.

When a sum of all crack lengths multiplied by the thickness of the segment where the cracks are located exceeds the value at_{net}, a failure due to yielding of the structure is assumed.

In chapter 9.2 there were described means of evaluating residual strength of the structure failing by unstable tearing. Two methods of assessing the structure applicable for LEFM conditions were presented. AIMA utilises the single-parametrical criterion, i.e. compares the SIF in the structure with the plane stress fracture toughness K_C. As it was mentioned, this criterion offers less accurate results than if an R-curve was utilised. However, it does not require storing the values of crack lengths and SIF during the calculation, hence saving the computational time and memory. After all, a very short period is spent after the crack growth starts accelerating, allowing to neglect the error.
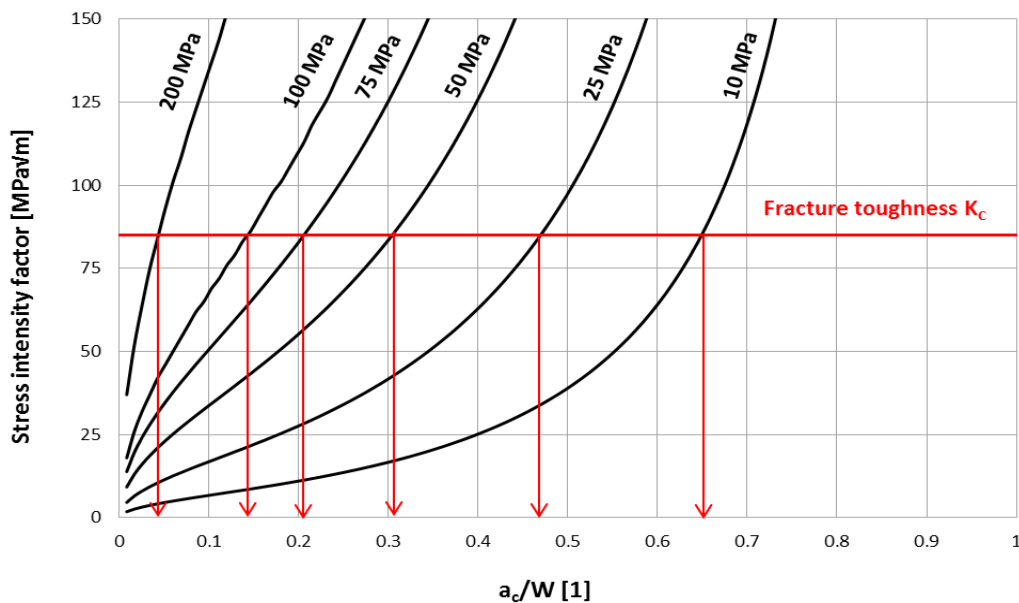

Figure 10.5 Critical edge crack length a$_c$ for various residual strength loads

74

Since a single parameter is assumed, it is possible to define a crack length a_c when SIF exceeds K_C. For a double crack at a hole, the SIF may decrease below the critical value for prolonging crack, since the shape function β is shrinking. However, once a crack gets to the edge, reaching the FT leads to successive failure of the segments, denoting the tearing fracture.

Based on the equations (8.1), (8.26) and (8.27) it is possible to define the critical edge crack length. Because of complex nature of β, it cannot be defined in a closed form. Therefore, we look for such crack length that SIF reaches the FT. In Figure 10.5 there is shown how the critical crack length is obtained for various limit loads.

10.2.12.2 Crack growth

The other part of the function deals with the cycle-by-cycle crack growth prediction. Cycles with zero or negative $\Delta\sigma$ does not contribute to the crack growth, therefore they are skipped.

Afterwards, if there are any fastener holes with still uninitiated cracks, the function proceeds to damage accumulation block. It is based on the methods described in chapter 6.4. The function *conc.m* takes care of stress concentration factor calculation. To save computational time this function is run only if a new crack appears, a failure of segment occurs or if damage has increased by 5 % since the last SCF update. Then the damage is updated according to equation (6.12). If the damage at any fastener hole side reaches a value 1, a new crack with initial length 1 mm is defined.

After updating the damage, the function proceeds to the crack growth part. Firstly, if any segment had failed, total crack lengths are calculated. These lengths correspond to the lengths as defined by a substitution by Harter, see Figure 7.7. Otherwise the total crack length is identical with a calculated crack length (see description of "update crack length").

Now the most complex part of the function comes: calculation of shape function β. To save computational time, it is run only for cracks meeting one of two conditions: either a crack is new or its length enlarged by 5 % since the previous β update. Methods described in chapters 8.4 to 8.6 apply. The function *beta_calc.m* determines the crack type and calls appropriate function for β calculation for each fastener hole. By the end, it calls *beta_interaction.m* which takes care of including crack interaction effects.

Consequently, stress intensity factor (maximum stress of a cycle K_{max} and peak-to-peak amplitude ΔK) and plastic zone size r_p are determined for every crack. If any SIF exceeds the fracture toughness, the failure of the segment is assumed. However, a segment usually fails by the Swift criterion, see equation (7.7). Information about the segments' status is stored in the matrix *tru.F*. If the segment failure occurred, total crack length is updated and after assessing the structure on limit loads it returns to the beginning of the loop. Provided no segment had failed, crack lengths are updated with respect to Forman equation (7.2). Since the equation is derived for continuous variables, it needs to be discretized:

$$a_i = a_{i-1} \max\left\{0;\; C_F \frac{(\Delta K_i)^{n_f}}{(1 - R_i)\, K_C - \Delta K}\, \Delta N\right\} \qquad (10.3)$$

where *i* is an index of the cycle number and *ΔN* is a step, always set equal to 1. Maximum is used to ensure that no negative crack length increments are counted in.

10.2.12.3 Residual strength

After obtaining new crack lengths, whether by Forman equation or as a result of failure of a segment, a capability of the structure to withstand residual strength limit loads is checked by the function *res_strength.m*.

Firstly, a condition on net-section yield (10.2) is evaluated. The evaluation of the unstable tear is conditioned by meeting one of two requirements. The first is when an edge crack length exceeds a critical crack length. Another is met if stress intensity factor K_{tear} calculated with the limit load σ_{RS} surpasses the fracture toughness value.

When evaluating the structure on unstable tear, a conservative assumption that all cracks had already initiated is made. The initial crack lengths are defined based on the actual accumulated damage according to eq. (10.4). This relation has no physical background and is only an approximation. Higher exponents would give much better fit to the growth of 1 μm crack until 1 mm, but the used value appears to be on the safe side.

$$a_{init_{RS}} = a_{init} D^{n_f} \qquad\qquad (10.4)$$

where a_{init} is initial crack length 1 mm, *D* is damage and n_f is Forman exponent.

This assumption results in immediate fracture if a quasi-U-shaped notch (see Figure 6.10) with over-critical length exists in the structure. Provided there is no edge crack yet, a crack growth loop without the damage accumulation part follows. If a domino segment failure does not occur, i.e. all SIF values drop below the fracture toughness, the loop is abandoned and the function assigns zero to variable *'stop'*.

10.2.12.4 Output results

After the fracture, number of cycles is recorded. These data are sent to *output_print.m* and written into *output.txt* and *cycle.txt.* In the latter file an ID of MC iteration, a number of cycles until the first crack appeared and time to fracture are printed. An example of *cycle.txt* is provided below:

```
Iter   Init    Failure
----------------
  1  129484   165113
  2  115237   148999
  3  117433   157316
  4  103330   144657
  5  106418   141459
         ...
```

10.2.13 converg.m

The function applies the algorithm presented in chapter 4.3.

10.2.14 output_print.m

The function writes results of an MC iteration into the file *output.txt*. Besides information about the used input file, sequence file and symmetry of the joint written by other functions, *output.txt* contains critical row and part IDs, number of cycles to 1 mm long crack for each side of every fastener hole and time to fracture for each MC iteration. Moreover, total calculation time is printed.

An example of the file *output.txt* for one MC iteration is shown below. Passages of the file enclosed by the blue frames are printed by various functions. Their names are displayed in the top right corner.

```
Data imported from:                                                    input_data.m
D:\Diplomka\MATLAB\Input\Bot_panel_0_MSD_input.xlsx
```

```
Sequence loaded from:                                                    sequence.m
D:\Diplomka\MATLAB\SQ\SQ_0093_AfgrowInput_RangePairFilterApplied.mat
```

```
The joint is symmetrical. Boundary condition of zero rotation          stress_calc.m
at symmetry axis chosen.
```

```
Critical row:     9                                                    output_print.m
Critical part:    2

Life for fasteners in the most critical row [Flight hours]:

-------------
Iteration 1
Left side:    117433  158198  170993  186447  143316  157961
Right side:   144165  138051  209511  151293  135559  137190

Failure after 165184 FH
```

```
Total time of calculation: 3367.26 s                                        run.m
```

10.2.15 post.m

The last executed function is a function *post.m*. It processes the data as described in chapter 4.4. Furthermore two plots are displayed. The first displays a trend of mean and standard deviation of the time to WFD occurrence with increasing number of Monte Carlo runs. The other one shows the probability distribution function and cumulative probability distribution function in relation with the number of cycles (flight hours).

10.3 Model validation

If AIMA is about to be used for WFD analyses of wing structures, validity of the results provided by the algorithm should be proved. The validation was performed on the fatigue test specimen used for derivation of the S-N curve for bottom panel splice joint. Geometry of the specimen is displayed in Figure 10.6. Uniform tensile stress levels used for S-N curve derivation are applied. A critical row is defined by the user with respect to the expected critical areas as depicted in the figure. Ten runs are performed for each stress level. An interval estimate of the mean value of cycles to fracture is calculated for confidence interval 95 % with use of eq. (10.5).

$$\langle \mu_{min}; \mu_{max} \rangle = \mu \pm \frac{t_\alpha s}{n - 1} \tag{10.5}$$

where μ and s are point estimates of the mean and standard deviation, t_α is the *(1-α)*th percentile of the Student distribution with confidence level α (α = 0.05 assumed) and *n-1* degrees of freedom, where *n* is a number of performed MC runs.

Results of the calculation are presented in Figure 10.7. Apparently, the results correspond to the experimental data. Especially for lower stresses (80 MPa and less), which are typical for WFD susceptible structures, the calculated values differ by less than 10 % from the 95 % confidence S-N curve. To conclude, the use of AIMA for MSD analysis is viable.
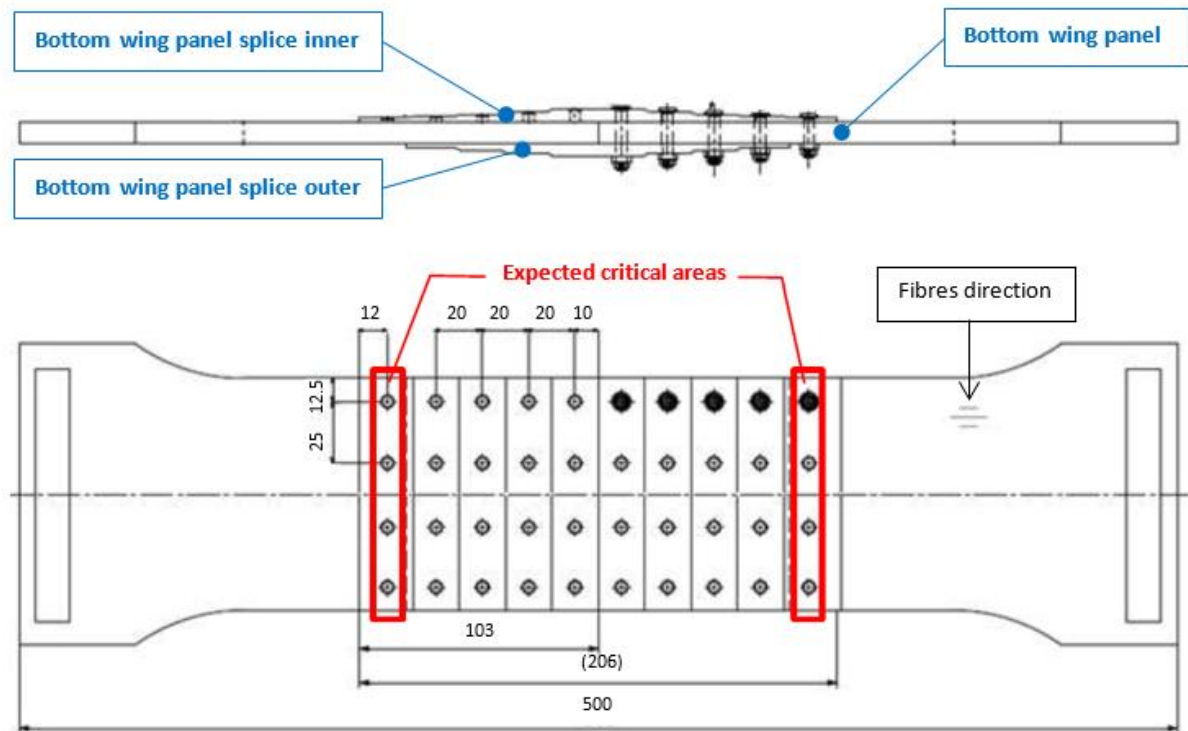
Figure 10.6 Geometry of the fatigue test specimen [15]
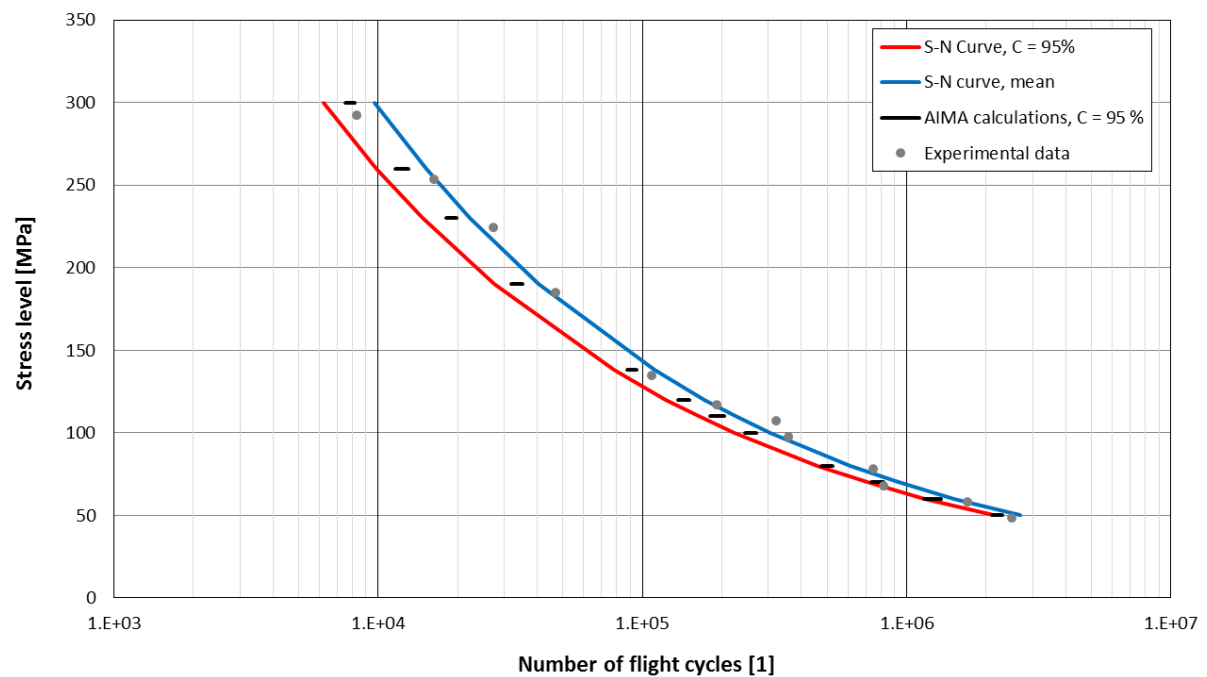
Figure 10.7 Comparison of fatigue life calculated by AIMA and by the test evidence (S-N curve)

11 Bottom panel splice joint analysis

To show capability of the AIMA algorithm, an analysis of one WFD susceptible area of the L 410 NG wing is performed. The bottom panel splice joint, as one of the most critical areas of the wing, suggests itself as an ideal candidate for such an analysis.

11.1 Geometry

The parts of which the joint is consisting are stated in Table 11.1. Basic information about the drawing number, semi-product and manufacturing process is provided. In Figure 11.1 there is geometry of the area displayed; front spar and top panel are set as semi-transparent.

Table 11.1 Drawing, semi-product and manufacturing process of analysed parts

Part	Drawing number, index and modification	Material, semi-product	Manufacturing process
Bottom integral panel	Y570245L/P, index A, ZKY001129	7475-T7351, 76 mm plate	Milled from plate Chromate coating
Outer bottom panel splice	Y571141N, index A, ZKY001336	7475-T7351, 35 mm plate	Milled from plate Chromate coating
Inner bottom panel splice	Y571143N, index A, ZKY001336	7475-T7351, 35 mm plate	Milled from plate Chromate coating
Rib 0	Y570086N, index A, ZKY000151	2124-T851, 50 mm plate	Milled from plate Chromate coating
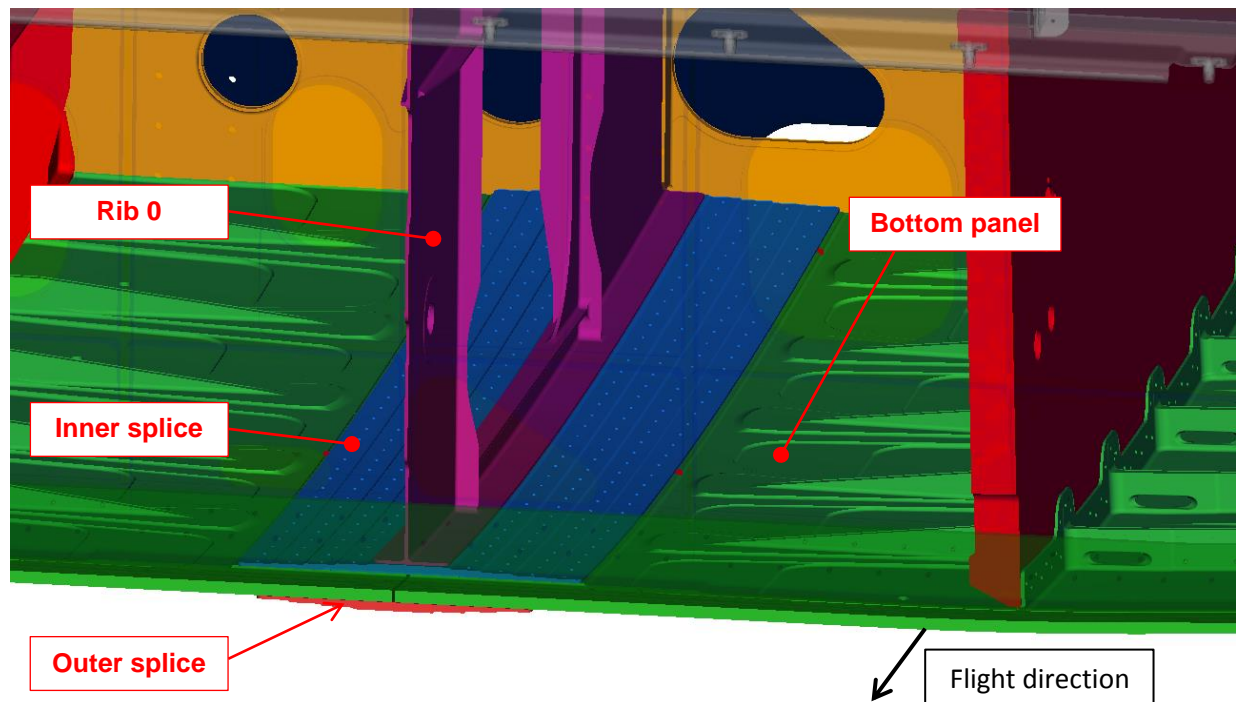
Figure 11.1 Geometry of the splice joint area

Fasteners Hi-Lite HST10 with diameter 3/16 in, i.e. 4.7625 mm, see [39], are used to connect the parts. Positions are defined in the drawing, see Appendix E. They are numbered in the form **ZXYYY** where *Z* is number of the part or a layer of CBUSH elements. *X* is an ID of the fastener row. Positions of holes or CBUSHes within the row are defined in the part *YYY*. Geometry is displayed in Figure 11.2 (blue signs for position of holes, red for position of CBUSH). The hole and the CBUSH at positions stated in the example below are highlighted (orange).
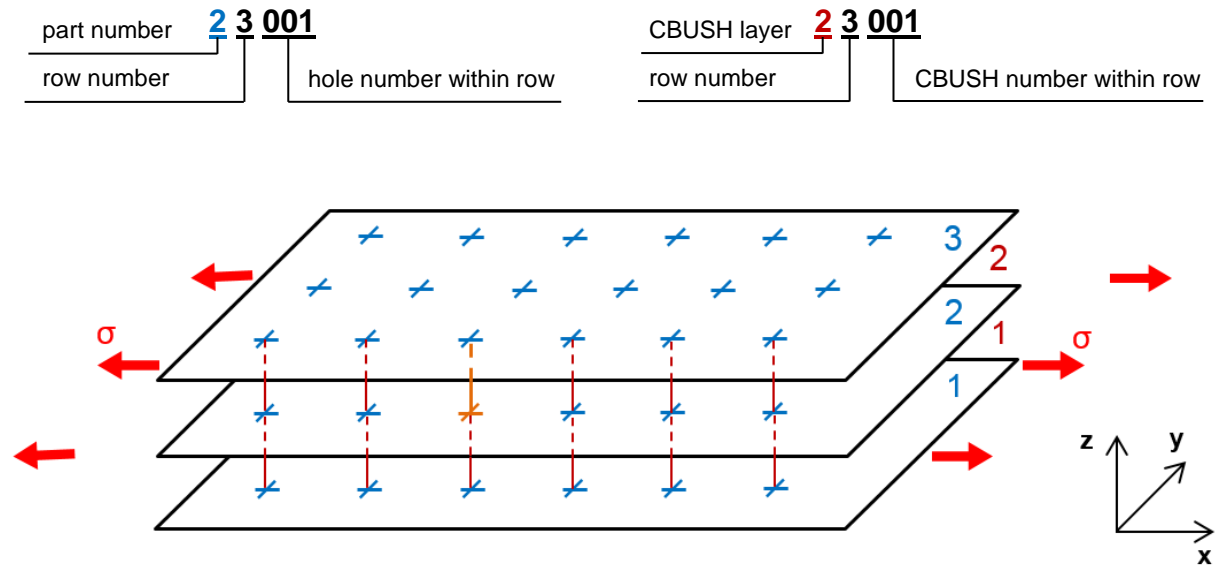
Figure 11.2 Fasteners position numbering;
blue: positions of centres of holes; red: positions of connecting elements (CBUSH)

The cross-section is identical for the whole length in chord-wise direction. Its shape is important for secondary bending stresses calculation and is modelled as a half in accordance with geometry shown in Figure 10.6. The geometry used in AIMA is displayed in Figure 11.3 with values presented in Table 11.2. Following numbering applies for the parts:

1. Outer bottom panel splice
2. Bottom panel
3. Inner bottom panel splice
4. Rib 0

Due to its negligible thickness in the section 0 (wing symmetry plane) and thus almost no forces transferred in the longitudinal direction, the rib is neglected in the analysis.

Table 11.2 Position of cross-section transitions and thickness of plates 1, 2 and 3 between the transitions

Position [mm]		x_1	x_2	x_3	x_4	x_5	x_6	x_7	x_8	x_9
		12.5	25.5	37.5	46.0	62.5	75.0	87.5	96.0	112.5
Diameter [mm]		4.763	0	4.763	0	4.763	0	4.763	0	4.763
Thickness [mm]	4	2.00	0	0	0	0	0	0	0	0	0
	3	5.50	5.50	4.50	4.50	3.50	3.50	2.50	2.50	2.00	0
	2	0	9.00	9.00	9.00	9.00	9.00	9.00	9.00	9.00	9.00
	1	5.50	5.50	4.50	4.50	3.25	3.25	2.00	0	0	0
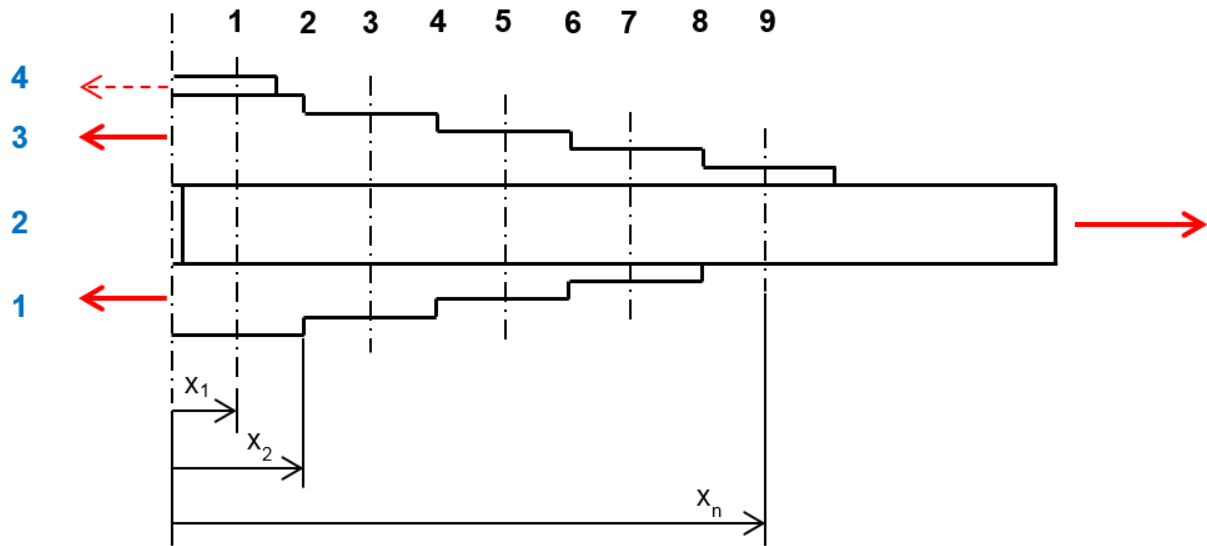
Figure 11.3 Geometry of the cross-section, right half;
blue numbers – part ID, black numbers – row ID

11.2 Applied loads

For derivation of the loading sequence the stresses during all the flight phases with considering gusts and manoeuvres need to be recorded. These loads are obtained by employing finite element method (FEM). Forces acting on the fasteners, which serve as inputs for fatigue analysis and derivation of SMF for given sequence, are taken from the results of load case 111, i.e. cruise with load factor 1 g. Because conditions represented by this load case cover majority of the structure's fatigue life, its application to all the load cases does not produce significant error.

The randomised sequence [45] utilised in the analysis is derived from the stresses in the panel in area of the front spar in section 0. The sequence generator Eris is used to create a sequence with application of range pair counting method.

SQ_0093_AfgrowInput_RangePairFilterApplied

A passage of the sequence is displayed in Figure 11.4. The sequence contains in average 737.295 cycles per flight hour and assumes 1-g-cruise stress σ_{1g} = 28.6 MPa. The residual strength limit load is assumed as a uniform tensile stress 120 MPa.
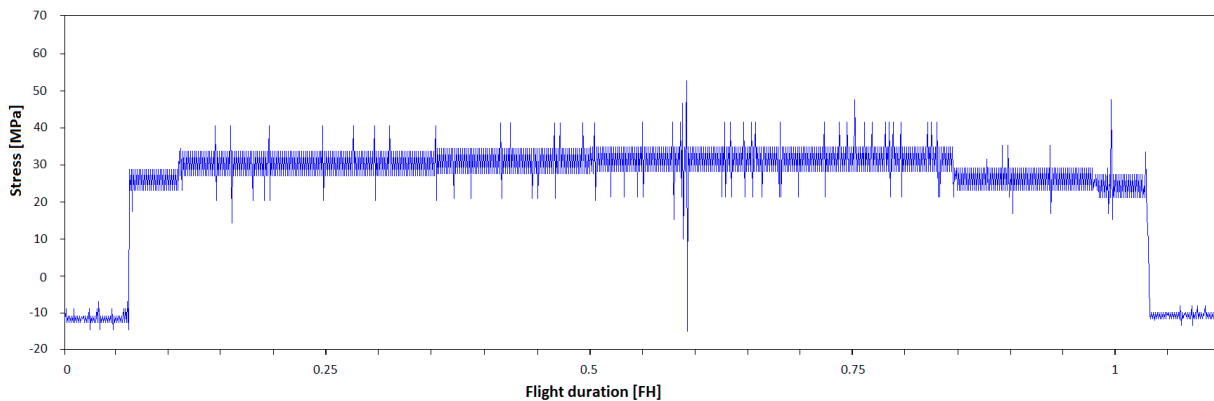
Figure 11.4 Passage of sequence SQ_0093_AfgrowInput_RangePairFilterApplied

The FEM model for stress and forces evaluation is derived from the global model [41] by local mesh refinement. It is built for MSC NASTRAN with use of ANSA pre-processor. The linear solver 101 is employed. Following elements are the building units of the model:

- shell elements CTRIA3 and CQUAD4
- string elements CBUSH (used for modelling the rivets in the analysed area)
- rigid body elements RBE2 and RBE3 (modelling the rivets in the rest of model)

Other elements such as CBEAM, CBAR etc. are used within the model; however they are not of big importance in the analysed area. The stiffness of CBUSH elements representing rivets is modelled by Huth's method [40].

While magnitude of the forces in all direction was obtained from the NASTRAN output text file *.f06*, stresses were obtained with use of μETA post-processor. For the calculation of by-pass stress which is an input to equation (5.1) the membrane stress was taken from the elements. When inputting the calculated forces into AIMA, it is important to preserve correct mutual orientation of the forces in the CBUSH elements, as depicted in Figure 11.5. The best approach to avoid problems with incorrect force calculation is to set orientation of all CBUSH elements in the same direction when building the model.
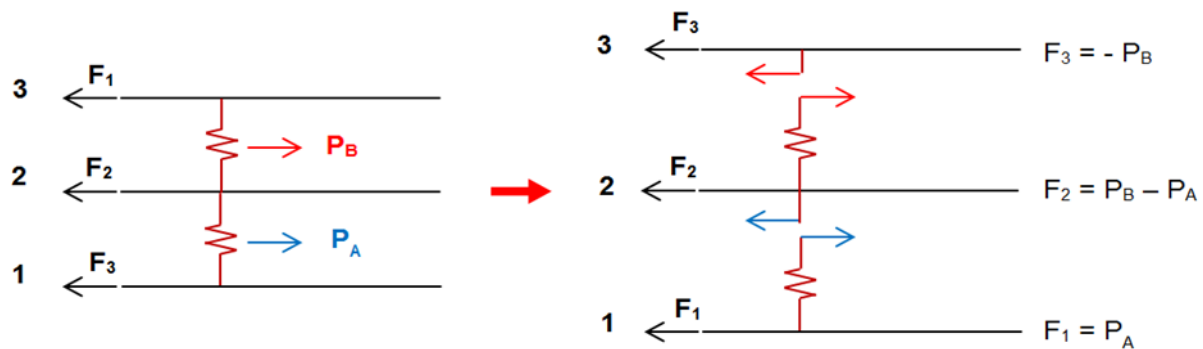
Figure 11.5 Orientation of CBUSH forces acting on constituent parts

11.3 Material properties

Aluminium alloy 7475-T7351 is used for manufacturing of all the three parts. Material properties based on the data in [37] and [38] are presented.

Table 11.3 Static properties of 7475-T7351 alloy, thickness 76 mm, L-T direction [38]

Yield strength	Mean value	$R_{p0.2}$	[MPa]	418.6
	Standard deviation	$s_{R_{p0.2}}$	[MPa]	8.66
Young's modulus	Mean value	E	[MPa]	69 260
	Standard deviation	s_E	[MPa]	1 440

Table 11.4 Crack growth parameters; 95 % confidence; 7475-T7351 alloy, thickness 76 mm, L-T direction [37]

Forman constant	C_f	$\left[\dfrac{m/cycle}{MPa\sqrt{m}^{1-n_f}}\right]$	1.07E-08
Forman exponent	n_f	[1]	2.83
Threshold SIF	K_{th}	[MPa√m]	0
Plane stress fracture toughness	K_c	[MPa√m]	85

Table 11.5 S-N curve parameters; 7475-T7351 alloy, thickness 76 mm, L-T direction [38]

S-N curve knee	Cycle count	N_{knee}	[cycles]	100 000
	Stress	σ_{knee}	[MPa]	142.6
A	Region $N \leq N_{knee}$	A_1	[cycle.MPa^{-m}]	5.7724E+11
	Region $N > N_{knee}$	A_2	[cycle.MPa^{-m}]	5.7724E+11
m	Region $N \leq N_{knee}$	m_1	[1]	3.1389
	Region $N > N_{knee}$	m_2	[1]	3.1389
Scatter	Standard deviation	s_{log}	log [cycle]	0.0684
S-N curve shift	Shifting factor	n_{det}	[1]	0.79

11.4 Analysis model

Based on the experiments performed on the test specimen described in Figure 10.6, it was concluded that the very last fastener row in the panel is critical; hence the analysis works with this assumption. Moreover, since the joint has symmetrical geometry and stresses differ only slightly between the left and right side of the wing, only right side (with higher maximum stress) is analysed. Index of the analysed part is then 2 and the row is 9.

Positions of the fasteners in the row are defined below in the vector *Y*, highlighted values represent edges of the material, i.e. does not contain holes. Curvature of the panel in chord-wise direction is neglected, since it does not directly influence the crack growth.

Y = [*0*, 13.5, 39 64.5, 89.5, 114.5, 140, 165.5, 193.5, 219,

244.5, 270, 295.5, 321, 346.5, 372, 397.5, 420, 445.5, 470.5,

497.5, 523.5, 549.5, 575.5, 601.5, 627.5, 652.5, 678, 703.5, 729,

754.5, 780, 805.5, 831, 856.5, 884.5, 909, 933, *945.5* **] [mm]**

Since the panel is a critical part, thickness along the whole row is equal to 9 mm. All holes have the same diameter defined by the Hi-lite fastener diameter, i.e. 4.7625 mm. By employing the methodology described in chapter 5 the vector of total stresses *S.max.val* along the row is obtained in the form:

S = [29.17, 29.00, 28.39, 27.70, 29.23, 28.75, 28.52, 27.79, 25.89, 25.89,

25.97, 26.84, 27.80, 26.13, 25.18, 24.17, 23.91, 24.02, 24.18, 23.32,

22.57, 21.08, 21.23, 20.24, 20.41, 20.25, 19.85, 18.95, 17.99, 16.84,

17.78, 17.85, 17.49, 16.95, 15.93, 15.65, 16.79 **] [MPa]**

Values of stresses and forces used for derivation of total stress σ_{tot} are displayed in Appendix F. The mean Young's modulus was assumed for secondary bending stress calculation for all parts. However, because it comprises at most 10 % of the total stress for any fastener, differences caused by varying Young's modulus are small.

The magnitude of the total stress along the row 9 in the panel (part ID = 2) is displayed in Figure 11.6. Apparently, it is higher in location of stringers run-outs. The stringers contribute to increase of the local stiffness of the panel, thus leading to transfer of higher load. As a result of various stress levels, probability of a crack initiation is different along the row. Mean expected time to crack initiation together with 95 % confidence band is displayed in Figure 11.7. Apparently, we can expect the first macroscopic crack to appear between the front spar and the second stringer.
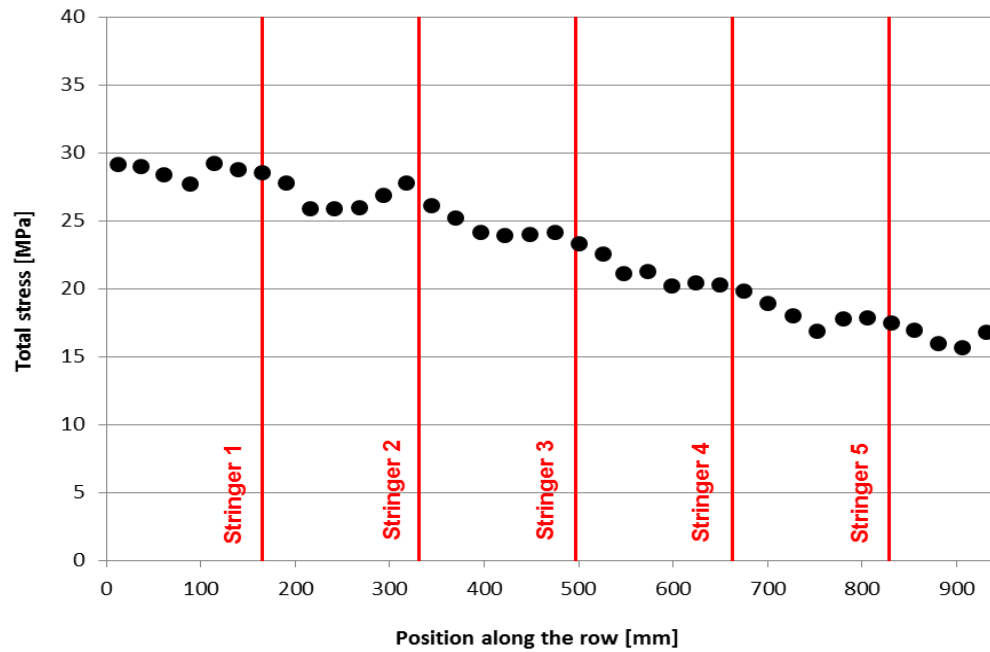
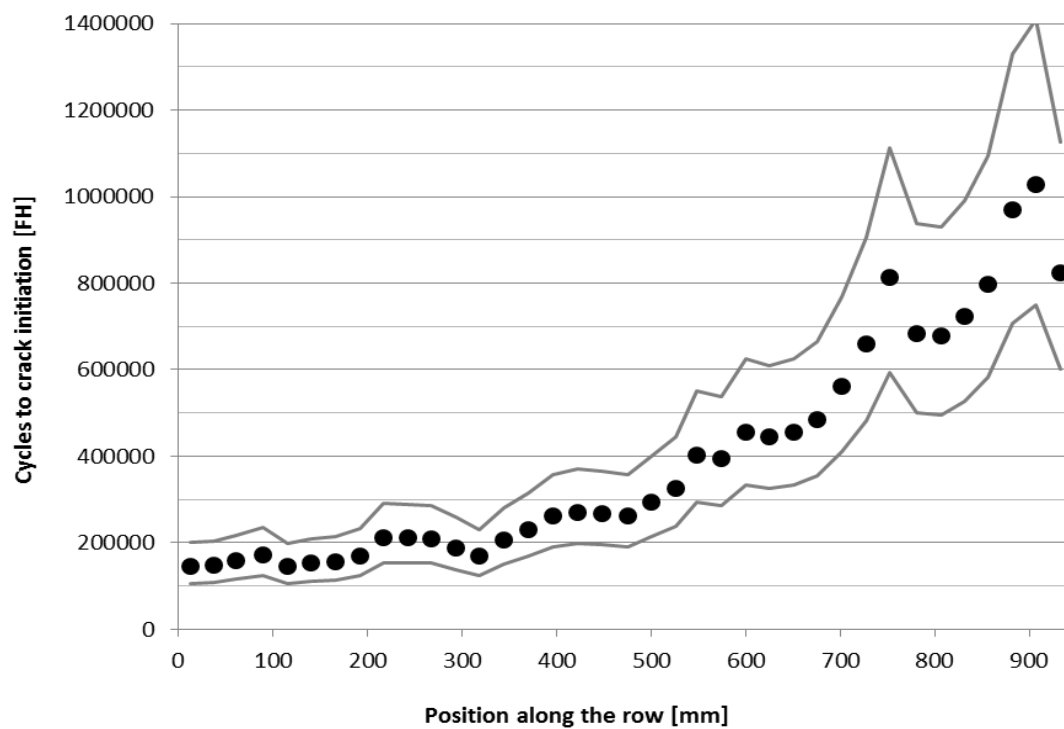**Figure 11.6 Total stress at fasteners along the row 9, part 2**

Figure 11.7 Expected time to crack initiation for fasteners along the row 9, part 2; Confidence band 95 %

11.5 Results

After 224 runs, the simulation satisfied the convergence criterion defined in chapter 4.3. The confidence band width defined by the first 50 runs was 298 flight hours. Mean of the time to WFD evaluated after each new simulation run is displayed in Figure 11.8. It is clear that all values are located within the confidence band.
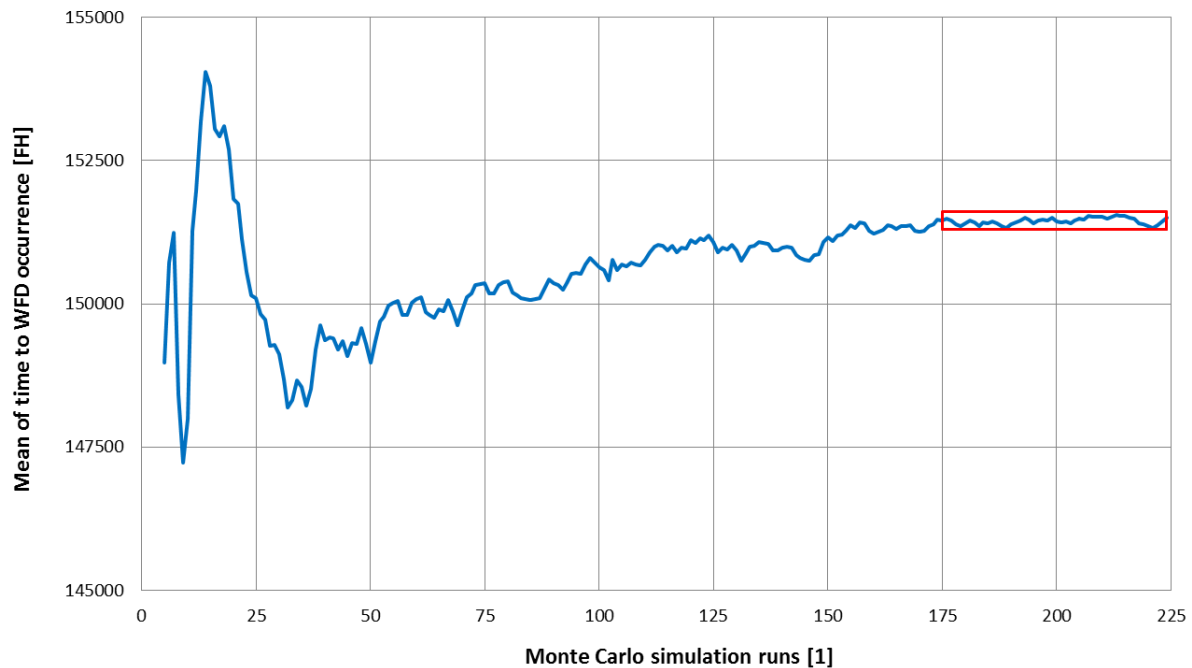
Figure 11.8 Mean of time to WFD occurrence after various number of runs of Monte Carlo simulation; Confidence band (red) as defined in chapter 4.3 displayed

The results of the calculation are presented in Table 11.6. The structural modification point depends on the statement of non-destructive testing department. However, because the inspection start point is far beyond the DSG, the assumption of ineffective inspections can be made, i.e. SMP is identical with ISP. In Figure 11.9 the cumulative probability distribution function of the time to the initiation of the first crack, to the failure of the first segment and to the WFD occurrence is displayed. Apparently, when comparing average values, the most of the fatigue life of the panel is spent in the phase of crack initiation (77.7 %). Until the first inter-hole segment fails, 95.6 % of the life is spent.

Table 11.6 Results of the MSD analysis

Time to 50 % fleet have a crack initiated	[FH]	117 751
Time to 50 % fleet have the 1st segment failed	[FH]	144 810
Time to 50 % fleet experience WFD	[FH]	151 510
Structural modification point	[FH]	50 500 or *75 750*
Inspection start point	[FH]	50 500
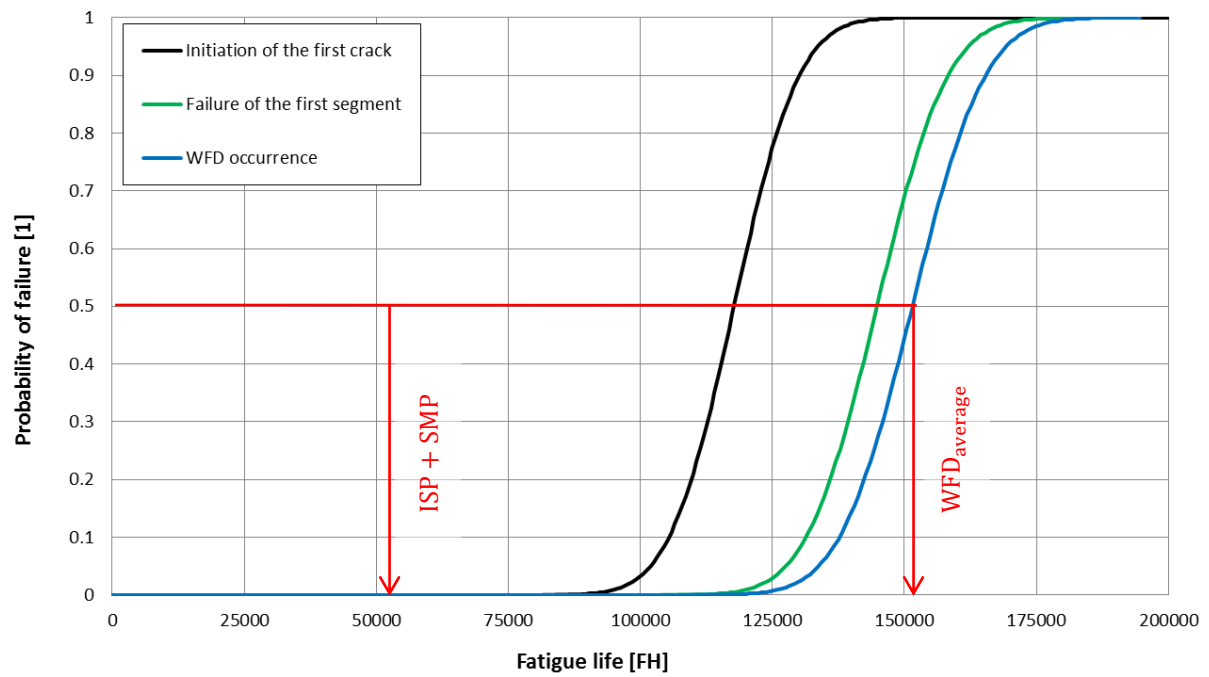
Figure 11.9 Cumulative probability distribution function of the time to WFD occurrence in the bottom panel splice joint

12 Conclusion

The thesis deals with the analysis of WFD susceptible wing structures. Regulations related to the WFD topic were identified and the methods of calculation recommended by AC 120-104 were considered. With application of methods for stress and fatigue calculations, and for crack growth predictions, an algorithm AIMA for multiple site damage analyses was developed. This software is capable of the complex MSD analysis of the structure, giving a user cumulative probability distribution of the first crack initiation and WFD occurrence as a result. Because of the stochastic nature of fatigue, Monte Carlo simulation method is employed for the MSD analysis. This approach requires significant number of runs to converge, consuming a large portion of time to provide the results. Because of this, AIMA works with many simplifications in order to save computational time.

To name the first one, an interaction between the cross sections is neglected when calculating the secondary bending stress. Including the interaction could lead to smoother stress distribution along the fastener rows. Another simplification is applied for the stress concentration factor (SCF) calculation for damage accumulation during the crack growth stage. Values of static SCF instead of generally lower fatigue ones are utilised. Moreover, if the stress near a hole or a notch exceeds the yield strength, no correction for plasticity is applied. All these simplifications lead to higher stress values and estimated shorter time to the crack initiation.

For the crack growth prediction, uniform axial loading is assumed. Stress intensity factor solutions to bending and bearing conditions are more complex, often only in tabular form for limited number of dimensions at disposal. To avoid necessity of including these solutions, axial, bearing and bending stresses are expressed as effective stress which represents the pure axial stress. Furthermore, no sequence interaction effects are included. Both these approaches result in higher effective stress intensity factor amplitude, leading to faster crack growth.

Only significant effect omitting which would lead to overestimating the fatigue life is a corrosion. It might be included by using an S-N curve developed from the fatigue test in corrosive conditions. Common approach is to minimize environmental effects during the operation, so the influence of corrosion could be ignored in the MSD analysis.

Validity of the algorithm used in AIMA was proved by the analysis of the L 410 NG bottom wing panel splice joint fatigue test specimen loaded by a constant amplitude. For all stress levels the 95% confidence interval of expected time to WFD occurrence lies between the mean S-N curve and the 95% confidence S-N curve. The agreement between the calculation and the experiment is apparent. Once the model validity was demonstrated, the analysis was performed on the entire splice joint with the operational loading sequence. It was shown that structural modification point lies far beyond the design service goal (DSG). This gives not only a sufficient margin for the MSD occurrence but also allows future consideration of extending the limit of validity beyond the actual DSG.

Despite the large capabilities of AIMA, it still has much to improve. Firstly a more user friendly interface could be implemented. Also the computational time is a challenge. The panel splice joint analysis ran around 220 hours, i.e. 9.3 days. This is a significant portion of time, which could be reduced by further improvement of the code, rewriting into a compiled language or simply using a computer with higher performance. After all, since a test evidence would take much more time and would be significantly more expensive, employing AIMA is still very effective way to assess the MSD behaviour of the structure.

13 References

[1]   HARTER, James A.: *AFGROW users guide and technical manual*. Centerville, Ohio: 2014.

[2]   NEWMAN, James C. Jr.: *An improved method of collocation for the stress analysis of cracked plates with various shaped boundaries*. Hampton, Virginia: NASA Langley Research Center: 1971.

[3]   ROOKE, David P. and CARTWIGHT, David J.: *Compendium of stress intensity factors*. London: Her Majesty's Stationary Office, 1976. ISBN 0117713368.

[4]   TADA, Hiroshi, PARIS, Paul C. and IRWIN, George R.: *The stress analysis of cracks handbook*. 2nd ed. St. Louis, Missouri: Paris Productions and Del Research Corp., 1985.

[5]   ROOKE, David P. and TWEED, J.: *Opening-mode stress intensity factors for two unequal cracks at hole*. Farnborough: 1979.

[6]   MIEDLAR, Peggy C., BERENS, Allan P., GUNDERSON Allan and GALLAGHER, J.P.: *USAF Damage Tolerant Design Handbook: Guidelines for the Analysis and Design of Damage Tolerant Aircraft Structures* [online]. Wright-Patterson AFB, Ohio: Air Force Wright Aeronautical Labs, 1984. [cit. 12.4.2016]. URL: http://www.afgrow.net/applications/DTDHandbook/default.aspx

[7]   VATANKHAH, Ali R.: Approximate Solutions to Complete Elliptic Integrals for Practical Use in Water Engineering. *Journal of Hydrologic Engineering*. 2011. November, p 942-945. ISSN 1084-0699.

[8]   ATA, Mustafa Y.: A convergence criterion for the Monte Carlo estimates. *Simulation Modelling Practice and Theory*. 2007, Vol.15, p 237–246. ISSN 1569-190X.

[9]   SWIFT, Thomas: Widespread fatigue damage monitoring – issues and concerns. In: *FAA/NASA International Symposium on Advanced Structural Integrity Methods for Airframe Durability and Damage Tolerance*. Hampton, Virginia: NASA Langley Research Center, 1994, Part 2, p 829-870.

[10]   SCHMIDT, Hans-Jürgen and SCHMIDT-BRANDECKER, Bianka: *Fatigue and damage tolerance course for metal structure*. 2014. Vol. 6.

[11]   HARTER James A.: *Internal Through Cracks in a Row of Fastener Holes* [online]. 2012. [cit. 12.4.2016]. URL: http://www.afgrow.net/DocumentHandler.ashx?name=Internal_Cracks_in_a_Row_of_Fastener_Holes.pdf

[12]   AC 120-104. *Establishing and implementing limit of validity to prevent widespread fatigue*. Federal Aviation Administration, 2011.

[13]   Federal Aviation Requirements, Part 23, Federal Aviation Administration.

[14]   PILKEY, Walter D.: *Peterson's stress concentration factors*. New York: John Wiley & Sons, 1997. ISBN 0-471-53849-3.

[15]   RŮŽEK, Roman and MLCH, Ivan: *Fatigue test results and evaluation of specimens representing splice joint in section 0 of L 410 NG aircraft.* Technical report SIGMA.4000.24.V.F.TR / R-6351. Praha: Výzkumný a zkušební letecký ústav, 2016.

[16]   SCHIJVE, Jaap: *Fatigue of Structures and Materials*. Dordrecht: Kluwer Academic Publishers, 2001. ISBN: 0-7923-7013-9.

[17]   LAGACE, Paul A.: *Unit M4.4: Simple Beam Theory* [online]. Massachusetts Institute of Technology, 2008. [cit. 12.4.2016].
URL: http://web.mit.edu/16.unified/www/SPRING/materials/Lectures/M4.4-Unified09.pdf

[18]   VLČEK, Dalibor and NÁGEĽ, Martin: *L410 UVP-E: Damage tolerance analysis of forward spar upper cap strap and leading edge splice in section 24*. Technical report ADATO.0474.A.U.TR. Kunovice: Aircraft Industries, 2016.

[19]   AUGUSTÍN, Petr: *Lectures to subject Fatigue of Aircraft Structures*. Brno: Brno University of Technology, 2015.

[20]   D'ERICCO, John: *inpaint_nans.m* [online]. Mathworks Files Exchange, 13.8.2012. [cit. 14.4.2016].
URL: http://www.mathworks.com/matlabcentral/fileexchange/4551-inpaint-nans

[21]   BOMBARDIER, Yan, LIAO, Min and RENAUD, Guillaume: *Fracture mechanics modelling of multiple site damage scenarios* [online]. Ottawa: National Research Council Canada, 2009. [cit. 15.3.2016].
URL: http://www.gruppofrattura.it/ocs/index.php/ICF/ICF12/paper/viewFile/1128/957

[22]   WU, Ling and SUN, Qin: A semi-analytical numerical method of determining stress intensity factors for multiple-site damage structure [online]. In: *23rd International Congress of Aeronautical Sciences*. Toronto, 2002, p 821.1-821.6. [cit. 15.4.2016]. URL:
http://www.icas.org/ICAS_ARCHIVE/ICAS2002/PAPERS/821.PDF

[23]   KATHIRESAN, K., HSU, T.M. and BRUSSAT, T.R.: *Advanced life analysis methods – Crack growth analysis methods for attachment lugs*. Technical report AFWAL-TR-84-3080, Vol. 2. Wright-Patterson AFB, Ohio: Air Force Flight Dynamics Labs, 1984.

[24]   TÝZNER, K.: *Hodnocení neregulárních zón křídla L 410 NG*. Kunovice: Aircraft Industries, 2011.

[25]   ASTM E399-90 (reapproved 1997). *Standard Test Method for Plane-Strain Fracture Toughness of Metallic Materials* [online]*. West Conshohocken, Pennsylvania: ASTM International: 2003. [cit. 22.4.2016]. URL:
http://web.mit.edu/3.35/www/Lecture_notes/plane_strain_fracture_toughness.pdf

[26]   TARPANI, José R. and SPINELLI, D.: Linear elastic vs elastic-plastic fracture mechanics methods. *Nuclear vessel integrity assessments in International Journal of Pressure Vessels and Piping.* 1997, Vol. 74(2), p. 97-103. ISSN 0308-0161.

[27]   *rng* [online]. Mathworks Documentation, 2016. [cit. 25.4.2016]. URL:
http://www.mathworks.com/help/matlab/ref/rng.html

[28]   KONG, JungSik, ZI, Goangseup, JEONG, MinChul, KIM, JungHoon, KIM, Minsung and VAN, Son-Nguyen: Fatigue life prediction of multiple site damage based on probabilistic equivalent initial flaw model. *Structural Engineering & Mechanics*. 2011, Vol. 38, No. 4, p 443-457. ISSN 1225-4568.

[29]   POOK, L.P.: *Linear fracture mechanics: What it is and what it does*. Report No 465. East Kilbride, Glasgow: National Engineering Laboratory, 1970.

[30]   MATSUMOTO, Makoto and NISHIMURA, Takuji: *Mersenne Twister: A 623-dimensionally equidistributed uniform pseudorandom number generator* [online]. Hiroshima: Hiroshima University,

1998. [cit. 3.5.2016]. URL: http://www.math.sci.hiroshima-u.ac.jp/~m-mat/MT/ARTICLES/mt.pdf

[31]   *Crack tip opening displacement (CTOD)* [online]. eFunda, 2016. [cit. 3.5.2016]. URL:
        http://www.efunda.com/formulae/solid_mechanics/fracture_mechanics/fm_epfm_CTOD.cfm

[32]   VLČEK, Dalibor: *Load spectra of the airplane L410-NG*. Technical report MOSTA.0420.A.U.PD,
        Revision D. Kunovice: Aircraft Industries, 2013.

[33]   YAHR, G.T.: *Fatigue design curves for 6061-T6 Aluminum*. Oak Ridge, Tennessee: Oak Ridge National
        Laboratory, 1993.

[34]   *Palmgren-Miner rule* [online]. Lectures to Intermediate Mechanics of Materials. Ames, Iowa: Iowa
        State University. [cit. 8.5.2016] URL: http://www.public.iastate.edu/~e_m.424/Palmgren-Miner.pdf

[35]   ASTM E647-15. *Standard test method for measurement of fatigue crack growth rates* [online]. West
        Conshohocken, Pennsylvania: ASTM International: 2015. [cit. 11.5.2016]. DOI: 10.1520/E0647-15.

[36]   PELIKÁN, František and JUREK, Peter: *Typical flight profile*. Technical report MOSTA.0103.A.A.PD,
        Revision G. Kunovice: Aircraft Industries, 2015.

[37]   BVOC, Maroš, MIČIC, Ján and VLČEK, Dalibor: *Metallic Materials Fatigue & Damage Tolerance Design
        Values. Appendix A103: 7475–T7351 aluminium alloy*. Technical report MOSTA. 0466.A.U.PD.
        Kunovice: Aircraft Industries, 2015.

[38]   HOMOLA, Petr, RŮŽEK, Roman, Nováková, Lucie, KAKOS, Martin and HRON, Robin: *Materiálové
        charakteristiky desky tl. 76 mm vyrobené ze slitiny 7475-T7351 ve směru L-T (Alcoa)*. Technical report
        R-5650. Praha: VZLÚ, 2013.

[39]   Hi-lite pin. *HST10* [online]. Torrance, California: Lisi Aerospace, 2015. [cit. 15.5.2016]. URL:
        http://www.lisi-aerospace.com/_layouts/CentralDocConnector/DCConnector.aspx?id=178&listId
        =Hi-LiteConfigurator&downloaded=HST10&type=nominal_size_shank

[40]   RAIANO, Michele: *Fastener modelling in NASTRAN* [online]. Aerospace Engineering, 2013. [cit.
        17.5.2016]. URL: http://aerospacengineering.net/?p=244

[41]   *Wing_PSE_MO3TP_AI05_Tec08*. FEM model. Kunovice: Aircraft Industries; Tecmos.

[42]   *SQ_0093_AfgrowInput_RangePairFilterApplied*. Randomised sequence. Kunovice: Aircraft Industries,
        2015.

[43]   *Aloha Airlines, Flight 243: Boeing 737-200, near Maui, Hawaii, April 28, 1988* [online]. Aircraft
        Accident Report NTSB/AAR-89/03. Washington, D.C.: National Transportation Safety Board, 1989.
        [cit. 17.5.2016]. URL: http://libraryonline.erau.edu/online-full-text/ntsb/aircraft-accident-
        reports/AAR89-03.pdf

[44]   VLČEK, Dalibor: *Aircraft L 410 NG* [online]. Let, 2016. [cit. 19.5.2016]. URL: http://www.let.cz/letadlo-
        l-410-ng.html

[45]   VLČEK, Dalibor: *Loading sequence for L 410 NG airplane*. Technical report MOSTA.0474.A.U.PD.
        Kunovice: Aircraft Industries, 2013.

14 Used software

Software name	Description	Version
Matlab	Computing environment, programming language	7.10.0
GNU Octave	Computing environment, programming language	4.0.0
ANSA (BETA CAE Systems)	FEM pre-processor	15.2.3
μETA (BETA CAE Systems)	FEM post-processor	15.2.3
MSC NASTRAN	FEM solver	2012.2.0
AFGROW	Damage tolerance analysis software	5.02.02.18
MS Excel (MS Office)	Tabular editor	2010; Office 365

15 Definitions and abbreviations

a	[mm]	Crack length
A	[cycle.MPa^{-m}]	Constant of an S-N curve
a_c	[mm]	Critical crack length
a_e	[mm]	Major ellipse semi-axis
B	[mm]	Spacing between fasteners in a row
b	[mm]	Distance of the centre of a hole from the edge
b_e	[mm]	Minor ellipse semi-axis
B_f	[mm]	Effective width of segment for given fastener
C	[%]	Confidence level
C_f	$\left[\dfrac{m/cycle}{MPa\sqrt{m}^{1-n_f}} \right]$	Forman equation constant
D	[FH^{-1} cycle^{-1}]	Damage
d	[mm]	Hole diameter
da/dN	[m/cycle]	Crack growth rate
D_{init}	[FH^{-1} cycle^{-1}]	Initial damage
DSG	[FH] or [FC]	Design service goal
E	[MPa]	Young's modulus
e	[mm]	Neutral line jump
E_{eff}	[MPa]	Effective Young's modulus for given section
EIFS	[mm]	Equivalent initial flaw size
F	[N]	Transferred force
f	[MPa / Nm]	Stress increment per bending moment in cruise
F_{off}	[1]	Offset correction of the shape function
F_w, F_{ww}	[1]	Finite width correction of the shape function
g	[1]	Load factor
ISP	[FH] or [FC]	Inspection start point
I_{WFD}	[FH] or [FC]	WFD inspection interval
J	[mm^4]	Area moment of inertia
j	[1]	Number of fastener
K	[MPa$\sqrt{m}$]	Stress intensity factor
K_C	[MPa$\sqrt{m}$]	Fracture toughness
$k_{cr,opp}$	[1]	Correction of damage increment at an uncracked side of a cracked hole
$k_{cr,vic}$	[1]	Correction of damage increment at a hole in vicinity of a crack

K_{IC}	$[MPa\sqrt{m}]$	Plane strain fracture toughness
k_{net}	[1]	Correction of damage increment due to net section loss
K_{NS}	[1]	Correction factor for the influence of net section loss due to crack presence
K_R	$[MPa\sqrt{m}]$	Crack growth resistance
K_t	[1]	Stress concentration factor
K_{t_g}	[1]	Stress concentration factor related to remote stress
K_{t_n}	[1]	Stress concentration factor related to nominal stress
K_{th}	$[MPa\sqrt{m}]$	Threshold stress intensity factor
L	[mm]	Length of segment between holes in direction of loading
ℓ	[mm]	Distance between a hole and a crack tip
LOV	[FH] or [FC]	Limit of validity
m	[1]	Exponent of S-N curve
M, M_b	[N mm]	Bending moment
N	[1]	Number of cycles
n	[1]	Number of some parameter (number of MC runs, number of boundary conditions etc.)
n	[1]	Cumulative frequency
$N_{a=1mm}$	[FH] or [FC]	Number of cycles until the macroscopic crack appears at given hole
n_{det}	[1]	S-N curve shifting coefficient
n_f	[1]	Exponent of Forman equation
n_f	[1]	Paris or Forman equation exponent
N_{init}	[FH] or [FC]	Number of cycles until the first macroscopic crack appears in whole structure
N_{knee}	[FH] or [FC]	Number of cycles at an S-N curve knee
P	[N]	Pin force
r	[mm]	Diameter of a hole, radius of an arc
R	[1]	Stress ratio
r_e	[mm]	Size of K-dominated zone
R_m	[MPa]	Ultimate strength
r_p	[mm]	Size of plastic zone
$R_{p0.2}$	[MPa]	Offset yield strength (2 % elongation)
s_{log}	[1]	Logarithmic standard deviation of S-N curve
SMF	[1]	Stress multiplication factor
SMP	[FH] or [FC]	Structural modification point
s_n^2	[1]	Sample variance of time to WFD

t	[mm]	Sheet thickness
TTCI	[FH]	Time to crack initiation
t_U	[mm]	Depth of U-shaped notch
W	[mm]	Plate width
w	[mm]	Displacement from neutral line
$WFD_{average}$	[FH] or [FC]	Period until 50 % of the fleet is WFD free
x	[mm]	Distance along x-axis
α	[1]	Confidence level
β	[1]	Shape function (for stress intensity factor)
β_{cor}	[1]	Correction factor for an influence of adjacent cracks on shape function
γ	[1]	Correction factor for offset of the centre crack
μ	[variable]	Mean value
ν	[1]	Poisson's ratio
ξ	[1]	Confidence band length
σ	[MPa]	Stress
σ_0	[MPa]	Flow stress
σ_{1g}	[MPa]	Stress level during the cruise with load factor equal to 1
σ_a	[MPa]	Stress amplitude
σ_b	[MPa]	Bending stress
$\sigma_{by-pass}$	[MPa]	Bending stress
σ_{knee}	[MPa]	Stress at an S-N curve knee
σ_m	[MPa]	Mean stress
$\sigma_{max}, \sigma_{min}$	[MPa]	Maximum or minimum stress
σ_p	[MPa]	Pin load stress
σ_{puls}	[MPa]	Maximum stress of pulsating cycle
σ_{RS}	[MPa]	Residual strength load case stress level
σ_y	[MPa]	Stress in direction of loading near the crack tip

AAWG	Airworthiness Assurance Working Group
AC	Advisory circular
ACI	Acceptable confidence interval
AI	Aircraft Industries, a.s.
AIMA	the algorithm name (derived from Aircraft Industries MSD Analysis)
ASCBR	Acceptable shifting confidence band rule
CB	Confidence band

CCT	Central crack tension (specimen)
CDF	Cumulative probability distribution function
CI	Confidence interval
CPU	Central processing unit
CS	Certification specification
CTOD	Crack tip opening displacement
DT	Damage tolerance
EASA	European Aviation Safety Agency
EPFM	Elastic-plastic fracture mechanics
FAA	Federal Aviation Agency
FAR	Federal Aviation Regulations
FC	Flight cycle
FEM	Finite element method
FH	Flight hour
FT	Fracture toughness
G-A-G	Ground-Air-Ground (cycle)
ID	Identification number
LEFM	Linear elastic fracture mechanics
MC	Monte Carlo
MED	Multiple element damage
MSD	Multiple site damage
NaN	Not-a-Number (used for missing values in the matrix)
R (curve)	Crack growth resistance
RNG	Random number generator
SCF	Stress concentration factor
S-N (curve)	Stress – Number of cycles to fatigue failure
TsAGI	Tsentralniy Aerogidrodinamicheskiy Institut
VZLÚ	Výzkumný a zkušební letecký ústav, a.s.
WFD	Widespread fatigue damage

16 List of appendices

A. Example input Excel spreadsheet

B. Example cumul_freq_gusts.txt file

C. Example cumul_freq_manoeuvres.txt file

D. Example cumul_freq_landing.txt file

E. Analysed area drawing

F. Loads applied to critical row in the panel splice joint analysis

Appendix A: **Example input Excel spreadsheet**

Geometry

THICKNESS t [mm]

BOTTOM	Area 1	Area 2	Area 3	Area 4	Area 5	Area 6	Area 7	Area 8	Area 9	Area 10
Line 1	0	0	0	2	3.25	3.25	4.5	4.5	5.5	5.5
Line 2	0	0	0	2	3.25	3.25	4.5	4.5	5.5	5.5
Line 3	0	0	0	2	3.25	3.25	4.5	4.5	5.5	5.5
Line 4	0	0	0	2	3.25	3.25	4.5	4.5	5.5	5.5

MIDDLE	Area 1	Area 2	Area 3	Area 4	Area 5	Area 6	Area 7	Area 8	Area 9	Area 10
Line 1	9	9	9	9	9	9	9	9	9	9
Line 2	9	9	9	9	9	9	9	9	9	0
Line 3	9	9	9	9	9	9	9	9	9	0
Line 4	9	9	9	9	9	9	9	9	9	0

TOP	Area 1	Area 2	Area 3	Area 4	Area 5	Area 6	Area 7	Area 8	Area 9	Area 10
Line 1	0	2	2.5	2.5	3.5	3.5	4.5	4.5	5.5	5.5
Line 2	0	2	2.5	2.5	3.5	3.5	4.5	4.5	5.5	5.5
Line 3	0	2	2.5	2.5	3.5	3.5	4.5	4.5	5.5	5.5
Line 4	0	2	2.5	2.5	3.5	3.5	4.5	4.5	5.5	5.5

MIDPLANE POSITION h [mm]

BOTTOM	Area 1	Area 2	Area 3	Area 4	Area 5	Area 6	Area 7	Area 8	Area 9	Area 10
Line 1	-4.5	-4.5	-4.5	-5.5	-6.125	-6.125	-6.75	-6.75	-7.25	-7.25
Line 2	-4.5	-4.5	-4.5	-5.5	-6.125	-6.125	-6.75	-6.75	-7.25	-7.25
Line 3	-4.5	-4.5	-4.5	-5.5	-6.125	-6.125	-6.75	-6.75	-7.25	-7.25
Line 4	-4.5	-4.5	-4.5	-5.5	-6.125	-6.125	-6.75	-6.75	-7.25	-7.25

MIDDLE	Area 1	Area 2	Area 3	Area 4	Area 5	Area 6	Area 7	Area 8	Area 9	Area 10
Line 1	0	0	0	0	0	0	0	0	0	0
Line 2	0	0	0	0	0	0	0	0	0	0
Line 3	0	0	0	0	0	0	0	0	0	0
Line 4	0	0	0	0	0	0	0	0	0	0

TOP	Area 1	Area 2	Area 3	Area 4	Area 5	Area 6	Area 7	Area 8	Area 9	Area 10
Line 1	4.5	5.5	5.75	5.75	6.25	6.25	6.75	6.75	7.25	7.25
Line 2	4.5	5.5	5.75	5.75	6.25	6.25	6.75	6.75	7.25	7.25
Line 3	4.5	5.5	5.75	5.75	6.25	6.25	6.75	6.75	7.25	7.25
Line 4	4.5	5.5	5.75	5.75	6.25	6.25	6.75	6.75	7.25	7.25

BOUNDARY CONDITIONS - displacement w_BC [mm]

SYMMETRICAL JOINT? (Y/N) Y

w_BC	Line 1	Line 2	Line 3	Line 4
	0.2	0.2	0.2	0.2

POSITION OF FASTENERS x,y [mm]

x	Origin	Row 1	Row 2	Row 3	Row 4	Row 5	Row 6	Row 7	Row 8	Row 9	End
	0	10	20	30	40	50	60	70	80	90	100

y	Origin	Line 1	Line 2	Line 3	Line 4	End
	0	25	50	75	100	125

FASTENERS DIAMETER d [mm]

	Row 1	Row 2	Row 3	Row 4	Row 5	Row 6	Row 7	Row 8	Row 9
Line 1	4.7625	0	4.7625	0	4.7625	0	4.7625	0	4.7625
Line 2	4.7625	0	4.7625	0	4.7625	0	4.7625	0	4.7625
Line 3	4.7625	0	4.7625	0	4.7625	0	4.7625	0	4.7625
Line 4	4.7625	0	4.7625	0	4.7625	0	4.7625	0	4.7625

Loads

INFORMATION ABOUT SEQUENCE

Stress level at cruise	σ_1g	[MPa]	28.6
Cycles per Flight Hour	CpFH	[1]	737.295
Residual strength load case stress	σ_RS	[MPa]	120

BY-PASS STRESS σ_By [MPa]

BOTTOM	Row 1	Row 2	Row 3	Row 4	Row 5	Row 6	Row 7	Row 8	Row 9
Line 1	-0.1	0.0	8.5	0.0	15.1	0.0	14.9	0.0	14.9
Line 2	-0.3	0.0	7.9	0.0	13.8	0.0	13.5	0.0	13.5
Line 3	-0.3	0.0	8.3	0.0	13.7	0.0	14.3	0.0	17.9
Line 4	-0.1	0.0	9.8	0.0	14.8	0.0	16.0	0.0	18.2

MIDDLE	Row 1	Row 2	Row 3	Row 4	Row 5	Row 6	Row 7	Row 8	Row 9
Line 1	22.6	0.0	18.8	0.0	14.9	0.0	7.1	0.0	0.8
Line 2	22.2	0.0	18.5	0.0	14.2	0.0	7.0	0.0	0.2
Line 3	21.9	0.0	18.4	0.0	14.2	0.0	7.2	0.0	0.0
Line 4	22.5	0.0	18.8	0.0	14.0	0.0	7.5	0.0	-0.1

TOP	Row 1	Row 2	Row 3	Row 4	Row 5	Row 6	Row 7	Row 8	Row 9
Line 1	0.0	0.0	2.3	0.0	10.7	0.0	15.4	0.0	18.4
Line 2	0.0	0.0	0.9	0.0	11.5	0.0	15.5	0.0	18.3
Line 3	0.0	0.0	0.7	0.0	9.2	0.0	9.2	0.0	12.9
Line 4	0.0	0.0	0.5	0.0	8.6	0.0	8.6	0.0	12.4

LONGITUDINAL PIN FORCE F_L [N]

BOTTOM	Row 1	Row 2	Row 3	Row 4	Row 5	Row 6	Row 7	Row 8	Row 9
Line 1	-313.1	0.0	-488.2	0.0	-456.8	0.0	-781.0	0.0	-853.8
Line 2	-306.9	0.0	-440.4	0.0	-428.8	0.0	-709.8	0.0	-796.0
Line 3	-307.4	0.0	-436.7	0.0	-412.6	0.0	-675.4	0.0	-758.8
Line 4	-287.3	0.0	-372.6	0.0	-385.6	0.0	-625.4	0.0	-728.8

TOP	Row 1	Row 2	Row 3	Row 4	Row 5	Row 6	Row 7	Row 8	Row 9
Line 1	0.0	0.0	508.6	0.0	735.2	0.0	879.0	0.0	1017.3
Line 2	0.0	0.0	500.0	0.0	694.7	0.0	828.7	0.0	970.0
Line 3	0.0	0.0	470.1	0.0	697.7	0.0	817.6	0.0	944.7
Line 4	0.0	0.0	440.0	0.0	688.4	0.0	830.4	0.0	948.3

TRANSVERSAL PIN FORCE F_T [N]

BOTTOM	Row 1	Row 2	Row 3	Row 4	Row 5	Row 6	Row 7	Row 8	Row 9
Line 1	-10.0	0.0	-15.0	0.0	-8.0	0.0	-20.0	0.0	-15.0
Line 2	-10.0	0.0	-15.0	0.0	-8.0	0.0	-20.0	0.0	-15.0
Line 3	-10.0	0.0	-15.0	0.0	-8.0	0.0	-20.0	0.0	-15.0
Line 4	-10.0	0.0	-15.0	0.0	-8.0	0.0	-20.0	0.0	-15.0

TOP	Row 1	Row 2	Row 3	Row 4	Row 5	Row 6	Row 7	Row 8	Row 9
Line 1	0.0	0.0	15.0	0.0	8.0	0.0	20.0	0.0	15.0
Line 2	0.0	0.0	15.0	0.0	8.0	0.0	20.0	0.0	15.0
Line 3	0.0	0.0	15.0	0.0	8.0	0.0	20.0	0.0	15.0
Line 4	0.0	0.0	15.0	0.0	8.0	0.0	20.0	0.0	15.0

Material properties

Identification of semiproduct series (identical number means that parts are made of the same series of semiproduct)				PART		
				BOTTOM	MIDDLE	TOP
				0	1	2
Young's modulus	Mean value	E	[MPa]	69260	69260	69260
	Standard deviation	s_E	[MPa]	1440	1440	1440
Yield strength	Mean value	Rp0,2	[MPa]	418.6	418.6	418.6
	Standard deviation	s_Rp0,2	[MPa]	8.66	8.66	8.66
SN curve	Coefficient	A_1	[cycle.MPa^-m]	5.77E+11	5.77E+11	5.77E+11
		A_2		5.77E+11	5.77E+11	5.77E+11
	Exponent	m_1	[log(cycle)/log(MPa)]	3.1389	3.1389	3.1389
		m_2		3.1389	3.1389	3.1389
	Behaviour knee	N_knee	[cycles]	100000	100000	100000
	Logarithmic standard deviation	s_log	[log(N)]	0.0684	0.0684	0.0684
Crack growth curve (da/dN)	Coefficient	C	[...]	1.07E-08	1.07E-08	1.07E-08
	Exponent	n_f	[1]	2.83	2.83	2.83
	Threshold SIF	K_0	[MPa.m^0.5]	0	0	0
	Fracture SIF	K_f	[MPa.m^0.5]	85	85	85
	Fracture toughness	K_C	[MPa.m^0.5]	53.36	53.36	53.36
Ratio between cycles to crack lenght 1 mm and cycles used for SN curve definition		n_det	[1]	0.79	0.79	0.79

Fatigue data

Section			0 (taken from 3)	
Dynamic coefficient	K_dyn	[1]		1
Upper value of cycle GAG	Δn_max	-		1.76
Flight duration		[FH]		1
Bending moment (Ue = 0,00 m/s, load factor n = 1)	Mn	[Nm]	Take-off	81 338
			Climb	90 874
			Cruise	92 083
			Descent	92 918
			Approach	78 516
			Landing	72 902
			Standing before T/O	-25 331
			Standing after LDG	-22 660
Bending moment (Ue = 3,05 m/s)	Mn	[Nm]	Take-off	99 408
			Climb	119 021
			Cruise	124 801
			Descent	128 523
			Approach	100 832
			Landing	93 336
Load factor (Ue = 3,05 m/s)	n	[1]	Take-off	0.2456
			Climb	0.3635
			Cruise	0.4261
			Descent	0.4748
			Approach	0.3086
			Landing	0.2762

Appendix B: Example *cumul_freq_gusts.txt* file

```
FLIGHT PHASES: CUMULATIVE FREQUENCIES FOR
GUSTS
-------
Cumul.freq.    Gust speed [m/s]
%
% Take-off
%
14.68523947    0.00
7.938542326    0.50
4.403224204    1.00
2.466462371    1.50
1.40193015     2.00
0.814250294    2.50
0.483470368    3.00
0.280572613    3.50
0.162411447    4.00
0.095228792    4.50
0.056677266    5.00
0.034255837    5.50
0.020965839    6.00
0.00801203     7.00
0.003162137    8.00
0.001327892    9.00
0.000593571    10.00
0.000123907    12.00
3.1665E-05     14.00
1.65209E-05    15.00
%
% Climb
%
  101.9938182  0
  55.13578752  0.5
  30.58184036  1
  17.13039241  1.5
  9.736866     2
  5.655236109  2.5
  3.357860721  3
  1.948669083  3.5
  1.128000919  4
  0.66139528   4.5
  0.393642251  5
  0.237918053  5.5
  0.145614649  6
  0.055646183  7
  0.02196208   8
  0.009222645  9
  0.004122549  10
  0.000860573  12
  0.000219924  14
  0.000114743  15
%
% Cruise
%
39.09333333    0
21.13306236    0.5
11.7217504     1
6.565928723    1.5
3.732055087    2
2.167602254    2.5
1.287038477    3
0.746907718    3.5
0.43235283     4
0.253506993    4.5
0.150879612    5
0.091191897    5.5
0.055812814    6
0.021328692    7
0.008417872    8
0.003534959    9
0.001580137    10
0.00032985     12
0.000084295    14
0.00004398     15
       ...
```

```
%
% Descent
%
  164.2446803  0
  88.78733981  0.5
  49.24714735  1
  27.58574857  1.5
  15.67966051  2
  9.106850427  2.5
  5.407295955  3
  3.138018913  3.5
  1.816464504  4
  1.065070984  4.5
  0.63389769   5
  0.383128853  5.5
  0.23448903   6
  0.089609249  7
  0.035366406  8
  0.01485159   9
  0.006638703  10
  0.001385814  12
  0.000354153  14
  0.000184775  15
%
% Approach
%
47.33984523    0
25.59095927    0.5
14.19438565    1
7.950973299    1.5
4.519310459    2
2.624845376    2.5
1.558531778    3
0.904463568    3.5
0.523555151    4
0.306982822    4.5
0.182706791    5
0.110428299    5.5
0.067586204    6
0.025827856    7
0.010193573    8
0.004280638    9
0.001913457    10
0.00039943     12
0.000102077    14
5.32573E-05    15
%
% Landing
%
  1.14E+01     0.00
  6.16E+00     0.50
  3.42E+00     1.00
  1.91E+00     1.50
  1.09E+00     2.00
  6.32E-01     2.50
  3.75E-01     3.00
  2.18E-01     3.50
  1.26E-01     4.00
  7.39E-02     4.50
  4.40E-02     5.00
  2.66E-02     5.50
  1.63E-02     6.00
  6.22E-03     7.00
  2.45E-03     8.00
  1.03E-03     9.00
  4.60E-04     10.00
  9.61E-05     12.00
  2.46E-05     14.00
  1.28E-05     15.00
```

Appendix C: Example *cumul_freq_manoeuvres.txt* file

```
FLIGHT  PHASES:  CUMULATIVE  FREQUENCIES  FOR
MANOEUVRES
-------
  Load factor n       Cum.freq.
positive negative
%
% Take-off
%
1       1             14.249
1.2044 0.798543002   1.548387693
1.3066 0.703240344   0.550454756
1.4088 0.617345831   0.216722401
1.511  0.535108107   0.088781055
1.6132 0.459376842   0.039030266
1.7154 0.387331033   0.017858795
1.8176 0.318105554   0.008425485
1.9198 0.251147204   0.004074014
2.022  0.186028407   0.002009648
2.1242 0.116657533   0.000946624
2.2264 0.046137389   0.000440371
2.3286 -0.018109747  0.000219293
2.4308 -0.080795488  0.000111068
2.533  -0.138544479  5.93498E-05
2.6352 -0.206161027  2.84934E-05
2.7374 -0.265755949  1.49237E-05
2.8396 -0.328488602  7.55474E-06
2.9418 -0.391597274  3.80882E-06
3.044  -0.455459912  1.90462E-06
%
% Climb
%
1       1             35.6225
1.2044 0.798543076   3.870969233
1.3066 0.703240418   1.376136889
1.4088 0.617345904   0.541806003
1.511  0.53510818    0.221952637
1.6132 0.459376916   0.097575665
1.7154 0.387331106   0.044646986
1.8176 0.318105628   0.021063712
1.9198 0.251147278   0.010185035
2.022  0.186028481   0.005024119
2.1242 0.116657607   0.00236656
2.2264 0.046137463   0.001100927
2.3286 -0.018109673  0.000548232
2.4308 -0.080795415  0.00027767
2.533  -0.138544405  0.000148375
2.6352 -0.206160953  7.12336E-05
2.7374 -0.265755875  3.73092E-05
2.8396 -0.328488528  1.88868E-05
2.9418 -0.3915972    9.52205E-06
3.044  -0.455459838  4.76155E-06
%
% Cruise
%
1       1             42.747
1.2044 0.798543005   4.645163079
1.3066 0.703240347   1.651364267
1.4088 0.617345834   0.650167204
1.511  0.53510811    0.266343164
1.6132 0.459376845   0.117090798
1.7154 0.387331035   0.053576384
1.8176 0.318105557   0.025276454
1.9198 0.251147207   0.012222043
2.022  0.18602841    0.006028943
2.1242 0.116657536   0.002839872
2.2264 0.046137392   0.001321112
2.3286 -0.018109744  0.000657878
2.4308 -0.080795486  0.000333203
2.533  -0.138544476  0.000178049
2.6352 -0.206161024  8.54803E-05
2.7374 -0.265755946  4.47711E-05
2.8396 -0.328488599  2.26642E-05
              ...
```

```
2.9418 -0.391597271  1.14265E-05
3.044  -0.455459909  5.71386E-06
%
% Descent
%
1       1             14.249
1.2044 0.798543002   1.548387693
1.3066 0.703240344   0.550454756
1.4088 0.617345831   0.216722401
1.511  0.535108107   0.088781055
1.6132 0.459376842   0.039030266
1.7154 0.387331033   0.017858795
1.8176 0.318105554   0.008425485
1.9198 0.251147204   0.004074014
2.022  0.186028407   0.002009648
2.1242 0.116657533   0.000946624
2.2264 0.046137389   0.000440371
2.3286 -0.018109747  0.000219293
2.4308 -0.080795488  0.000111068
2.533  -0.138544479  5.93498E-05
2.6352 -0.206161027  2.84934E-05
2.7374 -0.265755949  1.49237E-05
2.8396 -0.328488602  7.55474E-06
2.9418 -0.391597274  3.80882E-06
3.044  -0.455459912  1.90462E-06
%
% Approach
%
1       1             21.3735
1.2044 0.798543062   2.32258154
1.3066 0.703240403   0.825682133
1.4088 0.61734589    0.325083602
1.511  0.535108166   0.133171582
1.6132 0.459376902   0.058545399
1.7154 0.387331092   0.026788192
1.8176 0.318105614   0.012638227
1.9198 0.251147263   0.006111021
2.022  0.186028467   0.003014472
2.1242 0.116657593   0.001419936
2.2264 0.046137448   0.000660556
2.3286 -0.018109687  0.000328939
2.4308 -0.080795429  0.000166602
2.533  -0.13854442   8.90247E-05
2.6352 -0.206160967  4.27402E-05
2.7374 -0.26575589   2.23855E-05
2.8396 -0.328488542  1.13321E-05
2.9418 -0.391597214  5.71323E-06
3.044  -0.455459853  2.85693E-06
%
% Landing
%
1       1             14.249
1.2044 0.798543002   1.548387693
1.3066 0.703240344   0.550454756
1.4088 0.617345831   0.216722401
1.511  0.535108107   0.088781055
1.6132 0.459376842   0.039030266
1.7154 0.387331033   0.017858795
1.8176 0.318105554   0.008425485
1.9198 0.251147204   0.004074014
2.022  0.186028407   0.002009648
2.1242 0.116657533   0.000946624
2.2264 0.046137389   0.000440371
2.3286 -0.018109747  0.000219293
2.4308 -0.080795488  0.000111068
2.533  -0.138544479  5.93498E-05
2.6352 -0.206161027  2.84934E-05
2.7374 -0.265755949  1.49237E-05
2.8396 -0.328488602  7.55474E-06
2.9418 -0.391597274  3.80882E-06
3.044  -0.455459912  1.90462E-06
```

Appendix D: Example *cumul_freq_landing.txt* file

```
FLIGHT PHASES: CUMULATIVE FREQUENCIES FOR LANDING IMPACT
-------
Load factor | Cumul.freq.

1.00  1.00E+00
1.11  7.30E-01
1.22  4.30E-01
1.32  2.50E-01
1.43  1.20E-01
1.54  3.30E-02
1.65  1.15E-02
1.75  4.50E-03
1.86  2.00E-03
1.97  1.00E-03
2.08  5.00E-04
2.18  2.80E-04
2.29  1.60E-04
2.40  9.80E-05
```

Appendix E: **Analysed area drawing**

KRIDLO SKOREPINA

Y570008N

Appendix F: Loads applied to critical row in the panel splice joint analysis

Fastener ID	Position [mm]	P_L [N]	P_T [N]	σ_{by} [MPa]	σ_p [MPa]	σ_b [MPa]	σ_{tot} [MPa]
29000	13.5	-565.60	94.02	6.16	22.30	0.73	29.19
29001	39	-490.10	28.99	5.21	23.15	0.66	29.02
29002	64.5	-448.15	-16.26	4.74	22.85	0.82	28.42
29003	89.5	-449.81	33.33	4.80	22.15	0.77	27.72
29004	114.5	-451.45	26.16	4.80	23.90	0.54	29.24
29005	140	-459.70	11.36	4.85	23.65	0.26	28.76
29006	165.5	-184.26	29.33	2.00	24.20	2.39	28.59
29007	193.5	-398.42	16.54	4.22	22.05	1.57	27.84
29008	219	-386.31	41.79	4.15	20.35	1.43	25.93
29009	244.5	-382.10	4.33	4.02	19.95	1.98	25.95
29010	270	-377.50	10.60	3.99	20.20	1.84	26.02
29011	295.5	-377.77	9.42	3.99	21.20	1.71	26.90
29012	321	-376.15	7.88	3.97	21.20	2.72	27.89
29013	346.5	-367.78	6.24	3.88	20.25	2.07	26.20
29014	372	-355.16	4.00	3.74	19.45	2.06	25.24
29015	397.5	-343.95	4.10	3.62	18.60	2.01	24.23
29016	420	-338.84	6.44	3.57	18.40	2.00	23.97
29017	445.5	-338.87	7.55	3.58	18.55	1.95	24.08
29018	470.5	-337.93	6.90	3.56	18.70	1.97	24.24
29019	497.5	-330.81	-14.29	3.51	17.85	2.03	23.39
29020	523.5	-319.92	-11.16	3.38	17.05	2.20	22.63
29021	549.5	-304.30	-11.52	3.22	16.40	1.51	21.13
29022	575.5	-293.13	-11.16	3.10	16.40	1.78	21.28
29023	601.5	-286.99	-11.02	3.04	15.40	1.86	20.29
29024	627.5	-282.61	-12.30	3.00	15.60	1.87	20.46
29025	652.5	-275.74	-15.45	2.93	15.50	1.88	20.31
29026	678	-266.03	-18.88	2.84	15.25	1.82	19.91
29027	703.5	-252.09	-21.26	2.70	14.55	1.76	19.00
29028	729	-240.62	-20.25	2.57	13.80	1.67	18.04
29029	754.5	-233.19	-16.00	2.49	12.85	1.56	16.89
29030	780	-235.20	-18.14	2.51	13.15	2.18	17.85
29031	805.5	-239.36	-21.22	2.56	13.85	1.48	17.89
29032	831	-242.35	-26.60	2.61	13.60	1.33	17.54
29033	856.5	-243.61	-34.12	2.64	13.20	1.15	16.99
29034	884.5	-246.06	-43.52	2.68	12.35	0.93	15.96
29035	909	-264.12	-14.75	2.81	12.20	0.66	15.67
29036	933	-305.67	-71.31	3.38	12.25	1.20	16.82